



A critical review of powder-based additive manufacturing of ferrous alloys: Process parameters, microstructure and mechanical properties



Haniyeh Fayazfar ^a, Mehrnaz Salarian ^a, Allan Rogalsky ^a, Dyuti Sarker ^a, Paola Russo ^a, Vlad Paserin ^b, Ehsan Toyserkani ^{a,*}

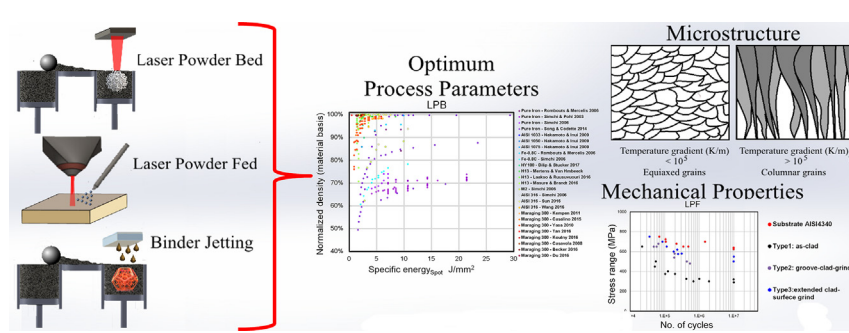
^a Multi-Scale Additive Manufacturing Lab, Department of Mechanical and Mechatronics Engineering, University of Waterloo, Waterloo, Ontario N2L 3G1, Canada

^b Rio Tinto Metal Powders, 1655 Route Marie-Victorin, Sorel-Tracy, Quebec J3R 4R4, Canada

HIGHLIGHTS

- Critical overview of different additive manufacturing (AM) process parameters on the quality of ferrous alloys.
- Introduction of new effective energy density numbers combined with the penetrated heat depth, hatch spacing and spot size.
- Critical overview of solidification and phase transformation of AM-processed ferrous alloys with mechanical properties.

GRAPHICAL ABSTRACT



ARTICLE INFO

Article history:

Received 28 October 2017

Received in revised form 2 February 2018

Accepted 6 February 2018

Available online 7 February 2018

Keywords:

Additive manufacturing

Laser powder-bed

Laser powder-fed

Binder jetting

Selective laser melting

Ferrous alloys

Steels

Process parameter

Microstructure

ABSTRACT

Additive manufacturing (AM) is an advanced manufacturing technology, enabling production of complex shapes by adding material layer-upon-layer, as distinct from conventional subtractive, forming and other manufacturing approaches. Thus far, several metallic materials including different types of ferrous alloys have been additively manufactured to full density with better or equivalent properties compared to counterparts made by conventional methods. In this perspective, this review article presents different powder-based additive manufacturing processes deployed to ferrous alloys, their key process parameters, phase transformation and microstructure development during solidification, all of which impact on mechanical behavior. The article enlightens the basics of Laser Powder-Bed (LPB), also known as selective laser melting), Laser Powder-Fed (LPF) and Binder Jetting (BJ) AM processes. These processes involve a sequence of complex/rapid thermal cycle and solidification behavior that influence the development of microstructure and eventually control the mechanical properties. A thorough discussion on mechanical behaviors, i.e., hardness, tensile, and cyclic/fatigue properties of AM manufactured steels is also presented based on several combined process parameters.

© 2018 Elsevier Ltd. All rights reserved.

1. Introduction

AM is a rapidly growing technique, where digital 3D design data is used to directly build up a product in a layer-by-layer process following

deposition, melting, fusion and binding of the successive material layers [1]. It is a direct manufacturing technology that enables to fabricate components composed of metal, polymer, ceramic, and composites with intricate features through external and internal layout, and reduce material consumption [2,3]. Metal AM technology has attracted industry/researchers where it offers unique applications in various industries for replacement or customization of parts with complex geometries,

* Corresponding author.

E-mail address: ehsan.toyserkani@uwaterloo.ca (E. Toyserkani).

Nomenclature

A	spot size area
c_p	specific heat capacity
d	laser spot diameter
g	acceleration of gravity
G	temperature gradient
H	capillary rise
k	thermal conductivity
l	layer thickness
\dot{m}	powder flow rate
P	laser power
q	laser energy flux
s	hatch spacing
t_d	drying time
T_m	melting temperature
T_0	room temperature
v	laser scan speed
V_s	solidification velocity
Z	normalized powder feed rate
α	thermal diffusivity
β	thermal absorptivity
ρ	Density
μ	dynamic viscosity of the melt pool
θ_s	melt pool transverse angle with respect to the substrate
γ	surface tension
ω	spacing between the walls
CE	carbon equivalent
$d\gamma/dT$	thermal surface tension gradient
HDR	heating depth ratio
VED	Volumetric Energy Density

internal structures and functionally graded properties [4–6]. Additional advantages of AM are: enabling consolidated parts for complex assembly, rapid production of prototypes and reduced design iterations, and faster market introduction of new products [7].

In contrast to the conventional cast and thermo-mechanical technique of material processing, in AM, there are limited options to modify the microstructures after manufacture, mostly because products are fabricated to near-net shape. Also, in the AM fabrication process, parts normally show significant anisotropy in properties along and perpendicular to the deposited layers. Samples deposited parallel (e.g. horizontal) or perpendicular (e.g. vertical) to the substrate undergo a different thermal history resulting in anisotropic mechanical properties [8,9]. The exact impact of process design parameters on physical and mechanical behaviors, and thus conformity of engineering parts fabricated via AM is still not well understood. Therefore, determination of the mechanical behaviors and also the influence of process design parameters for AM parts are of vital importance to predict their performance in service [10].

The goal of this paper is not to include all the existing studies related to AM of ferrous alloys but to provide an overview for researchers to understand significant and imminent research problems or opportunities as well as the R&D trend in this area. To this end, the most common mechanical properties reported in the literature for various ferrous alloys as well as process parameters control to achieve high density, near-net shape AM parts are investigated and reported for three AM techniques; Laser Powder-Bed (LPB), Laser Powder-Fed (LPF) and Binder Jetting (BJ) that are mainly used for the fabrication of parts composed of ferrous alloys. Electron-beam powder-bed fusion (EPBF) has also been used for the fabrication of parts composed of ferrous alloys; however, due to a very limited number of papers in the literature, the detail of this process is not included in the critical analysis. In addition, AM of

Metal Matrix Composites (MMCs) with ferrous alloys reinforcement elements, their process types and parameters, microstructural and mechanical properties are briefly summarized.

2. Additive manufacturing processes

2.1. Laser powder-bed (LPB)

LPB falls under powder-bed fusion AM according to ASTM committee F42 standard. LPB, also known as laser powder-bed fusion or selective laser melting (SLM), is a layer-upon-layer AM technique, where powder is spread in a layer and melted using a focused laser beam as shown in Fig. 1, to produce dense metallic parts. In this process, the obtainable geometric tolerance and minimum feature sizes are between 40 and 200 μm [11]. The overhanging geometry is supported by unmelted powder from previous layers. The main limitations for LPB are low build rate and the need to clear unmelted powder from internal geometry. A review with typical process applications can be found in [12]. LPB is widely used in multidisciplinary arenas such as, (1) in engineering to manufacture light weight machine parts, complex geometrical components, fuel cell, architectural design etc., (2) it also has demand in medical and dental applications because of some unique properties. The review identified two LPB topics generally applicable to any alloy, namely: (i) process optimization to maximize build rate at full density, (ii) microstructure control versus mechanical properties.

The operating design of LPB is schematically illustrated in Fig. 1a. In this technique, a numerically developed hatch stripe pattern is used over which the laser beam is scanned to melt the deposited powder layer as shown in Fig. 1b [13]. The main process parameters used in LPB are schematically shown in Fig. 1b, where the area is divided into stripes; comprising of several tracks detached by hatch spacing. The track is fabricated using laser beam with a fixed scan speed. During laser scanning process, an inert gas such as argon or nitrogen is introduced into the chamber to minimize oxidation. The platform is heated to about 80 °C before depositing and melting of the powder. After completing the process, the left-over powder is vacuumed and screened to be reused.

2.2. Laser powder-fed (LPF)

LPF falls under Directed Energy Deposition (DED) based on ASTM committee F42 standard. It is a class of laser-based additive manufacturing processes to synthesize full-density and high-performance complex metallic functional components. It is also known as laser consolidation, laser direct metal fabrication, laser cladding with blown powder, etc. This technique is based on a laser beam, focused on a specific area of a part where the powder is simultaneously supplied through a nozzle pointing to the same area, layer by layer. In contrast to the LPB process, which employs a bed of powder metal that is 'selectively' melted by a laser, LPF is accomplished by simultaneously delivering metallic powder and focused laser energy, as schematically shown in Fig. 2.

In LPF, a high power laser (e.g., Fiber, Disk, Nd:YAG or CO₂) is used to fabricate a melt zone on a substrate within an inert atmosphere; simultaneously, powder is injected to the melt through the laser beam. Subsequently, parts are made layer by layer using a 3D CAD file with each layer assembled track-upon-track via a controlled tool-path.

Advantages of the LPF process include the production of near-net-shape, full density parts with good mechanical properties and minimal imperfections (e.g. micro-cracking, distortion) [10,15]. A broad range of LPF applications was observed to various areas, including: 1) net shaped solid metallic parts, 2) functionally graded materials, 3) cellular solids, 4) in-situ alloyed parts, and 5) parts with conformal/internal features. However, predicting the properties of fabricated parts is very complicated due to the many process variables involved. Therefore, a better understanding regarding the microstructural evolution and

resulting materials properties is needed to achieve more consistency in the properties of the deposited parts.

2.3. Binder jetting (BJ)

In the binder jetting AM process (one of the AM classes based on ASTM standard), complex metal parts are fabricated using different materials by selectively injecting liquid binder agent into a powder bed. The BJ process is schematically shown in Fig. 3. After one layer is printed, a counter-rotating roller or a wiping blade spreads a new layer of powder on the surface of the prior layer, which is subsequently printed and stitched with the earlier one through jettied binder. This procedure is repeated to finish the green part formation. The BJ printing process is completed by post-sintering of 3D printed green parts in a high-temperature furnace, where the polymeric binder is burned off and the powder particles are sintered together through atomic diffusion to achieve final density and strength [16,17].

The main advantages of the BJ technique are: (1) the prevention of residual stresses in the printed parts due to the absence of rapid heating and cooling of the melt pool, (2) no need to support structure and build substrate, (3) no need for environmentally controlled chamber during the green parts fabrication, (4) compatible with highly reflective materials in contrast to LPB [16]. However, one of the major drawbacks of the BJ process is the difficulty to reach full density parts after the post-sintering, leading to reduced mechanical performance of the BJ-made parts compared to conventional manufactured ones [18]. Moreover, BJ is usually unable to process ultra-fine and loosely packed powders. Ultra-fine powders are difficult to spread owing to low flowability and potential powder agglomeration due to humidity, creating defects in the green parts. The sintered products will experience a significant dimensional change and reduction in mechanical properties [19].

Within the steel family, the use of metal BJ process has been limited to the fabrication of end-use products from stainless steel (SS) powders. Binder jetted SS materials have shown applications in the area of aerospace, energy, automotive, prosthetics [21,22], microwave circuits and antennas [23], art, and design industry as rotors, stators, impellers, etc. offering a significant manufacturing time reduction and impactful weight and cost savings [24]. For example, meshed Ku band waveguides of 420 SS are fabricated using the BJ process, which reduces the material usage and weight by 22% while obtaining the low loss characteristic of metallic waveguides [23].

2.4. Electron-beam powder-bed fusion (EPBF)

EPBF falls under the class of powder-bed fusion AM as per the ASTM standard F3001-14 [25], which is a layer-by-layer process with similar

capabilities to LPB [26], as schematically shown in Fig. 4. Electrostatic charge is a consideration, leading to use of slightly larger powder (<40 µm fraction excluded [27]). The main process differences are the need for high vacuum and the use of the electron beam to pre-heat the powder bed. Use of vacuum is beneficial in eliminating impurities such as oxygen; however, it can also strip out low boiling point alloying agents such as Mn [28]. Electron beam heating provides interesting design capabilities for microstructure control [29], but its capabilities appear to be largely unstudied in ferrous alloys. Work with ferrous alloys is limited to two reports, which note that the cooling rate in the build chamber was insufficient to harden H13 tool steel [28]. This is disadvantageous for less hardenable low alloy materials but may lead to more consistent microstructure for higher alloy materials where post processing heat treatment is necessary. Arcam AB (A GE Additive company) is the only commercial equipment supplier for EPBF equipment and holds the process under patent until 2022 [25]. This causes limited new material development from this process [25,30]. However, it is reasonable to expect the field to open up as Arcam's patents expire.

3. Reflection on the number of relevant papers covering ferrous alloys

Fig. 5a, b illustrate the volume of papers associated with different kinds of steels processed by various AM processes. Among them, majority of the work is reported using the LPB process (155 papers) followed by the LPF process (54 papers), to the best knowledge of the authors and as of August 2017.

In the literature, the BJ process (15 papers) is limited to 420 SS and 316 SS. However, compared to others, the EPBF process (2 papers) is only available for limited work on H13 tool steel. Therefore, based on the literature, sufficient study is not available to do a critical review of the EPBF process.

For various AM processes of LPB, LPF and BJ, the pie charts in Fig. 6a–c represent the detail studies for each technique that have used steel powders of various compositions. In the LPB process, as shown in Fig. 6a, almost equal amount of work has been done on H13 tool steel, maraging steel and M2 HSS.

For other SS, i.e. 316 SS, 420 SS, 17-4 PH SS and low alloy steels, very limited work has been reported using LPB. From Fig. 6b, it was observed that in LPF, the most researched steel powders were 316 L SS and H13 tool steel followed by low alloy steels. However, only a limited amount of LPF studies have been reported on using 420 SS, 304 SS and maraging steel. In contrast to LPB, in BJ as shown in Fig. 6c, most of the work has been done with 316 SS and 420 SS. Also, the process covers a small quantity of work on pure iron, 430 SS and 410 SS.

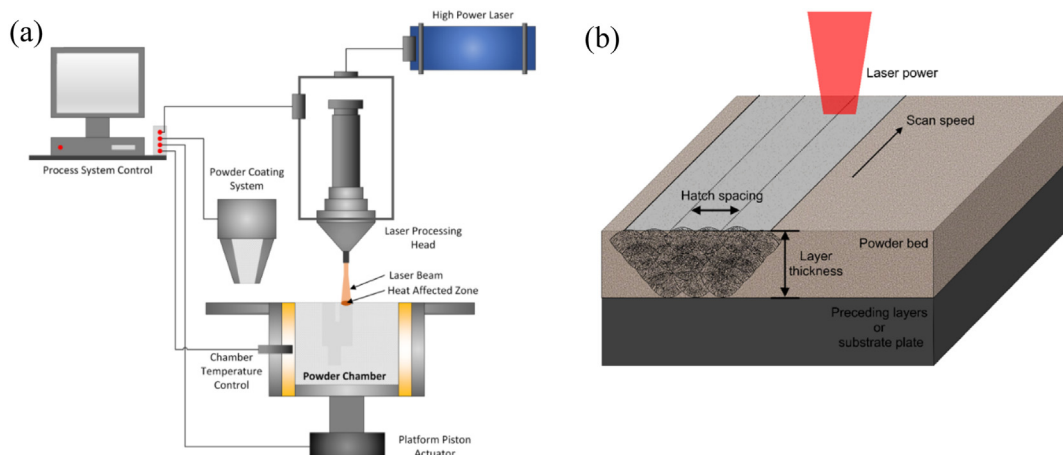


Fig. 1. (a) Schematic of operating process design in LPB, (b) close up of the LPB process zone [13].

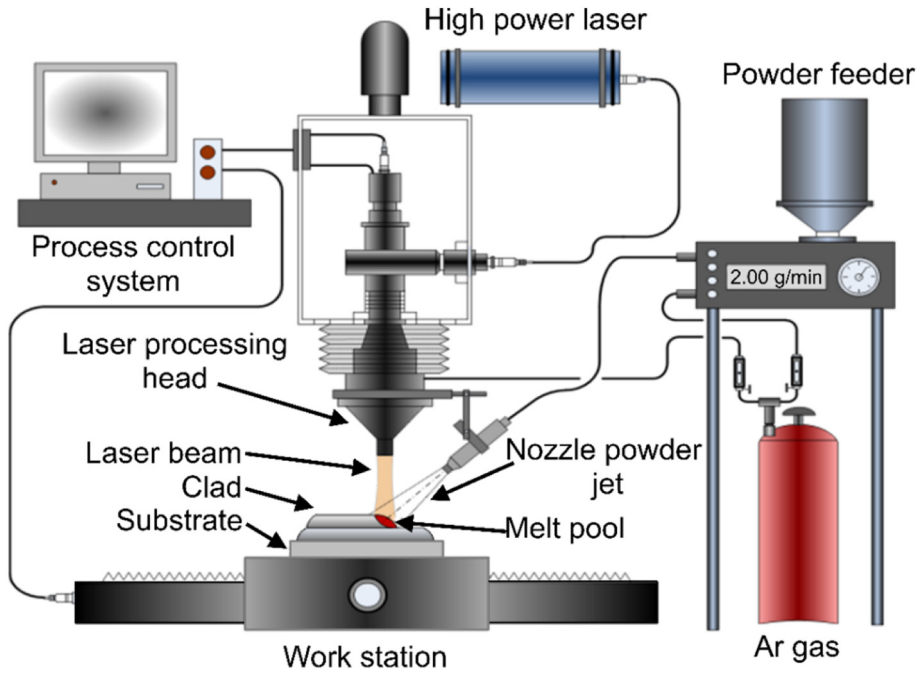


Fig. 2. Schematic presentation of the LPF technique (reproduced with permission from Elsevier) [14].

4. General process parameters

A wide range of process parameters as well as physical phenomena control the quality of AM products. Fig. 7 summarizes these parameters grouped as input parameters, process physics, and outputs. Commonly, the input parameters are as follows: laser energy, motion device, powder feeder set points, material, binder and ambient properties. In the design parameter chart, the output signifies the quality of the final product, listed as geometry, microstructure, hardness, cracks, porosity, residual stresses, surface roughness, and dilution [32]. Among the detail listed parameters in the chart (Fig. 7), some of the significant

parameters and their impact on physical and mechanical behaviors are discussed here.

As shown in Fig. 7, there are many common parameters for all three processes; however, each process has its own specific parameters too. With this point in mind, in the following, the role of common process parameters and process specific parameters are discussed. In addition, the authors intend to combine several parameters together to ease the critical review of results. To this extent a few new combined process parameters are proposed for the first time in this review paper. It has to be noted that some of the parameters are inherently important for a specific AM process and may not be relevant to other AM processes covered

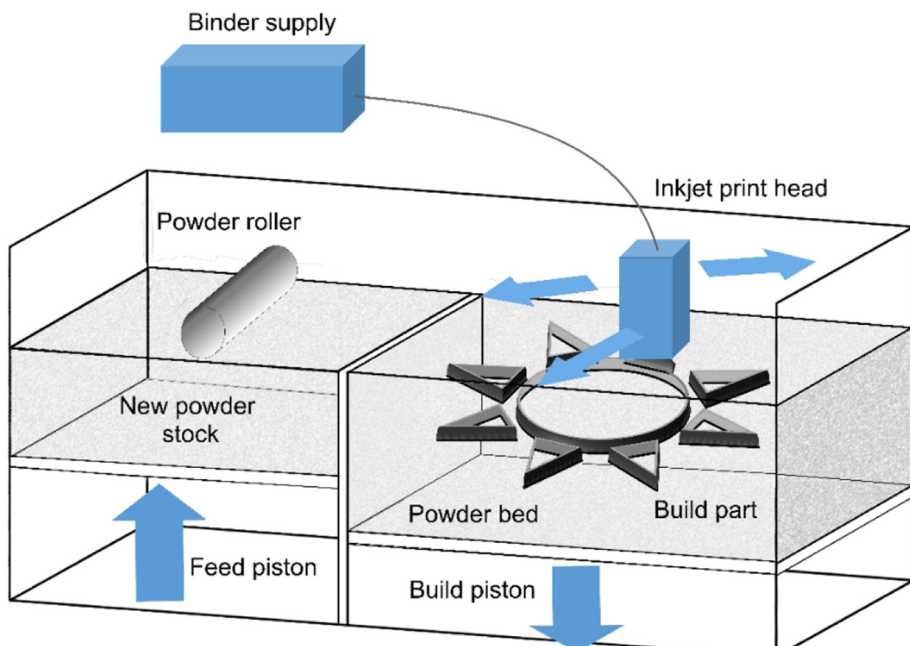


Fig. 3. Representation of binder jet 3D printing process [20].

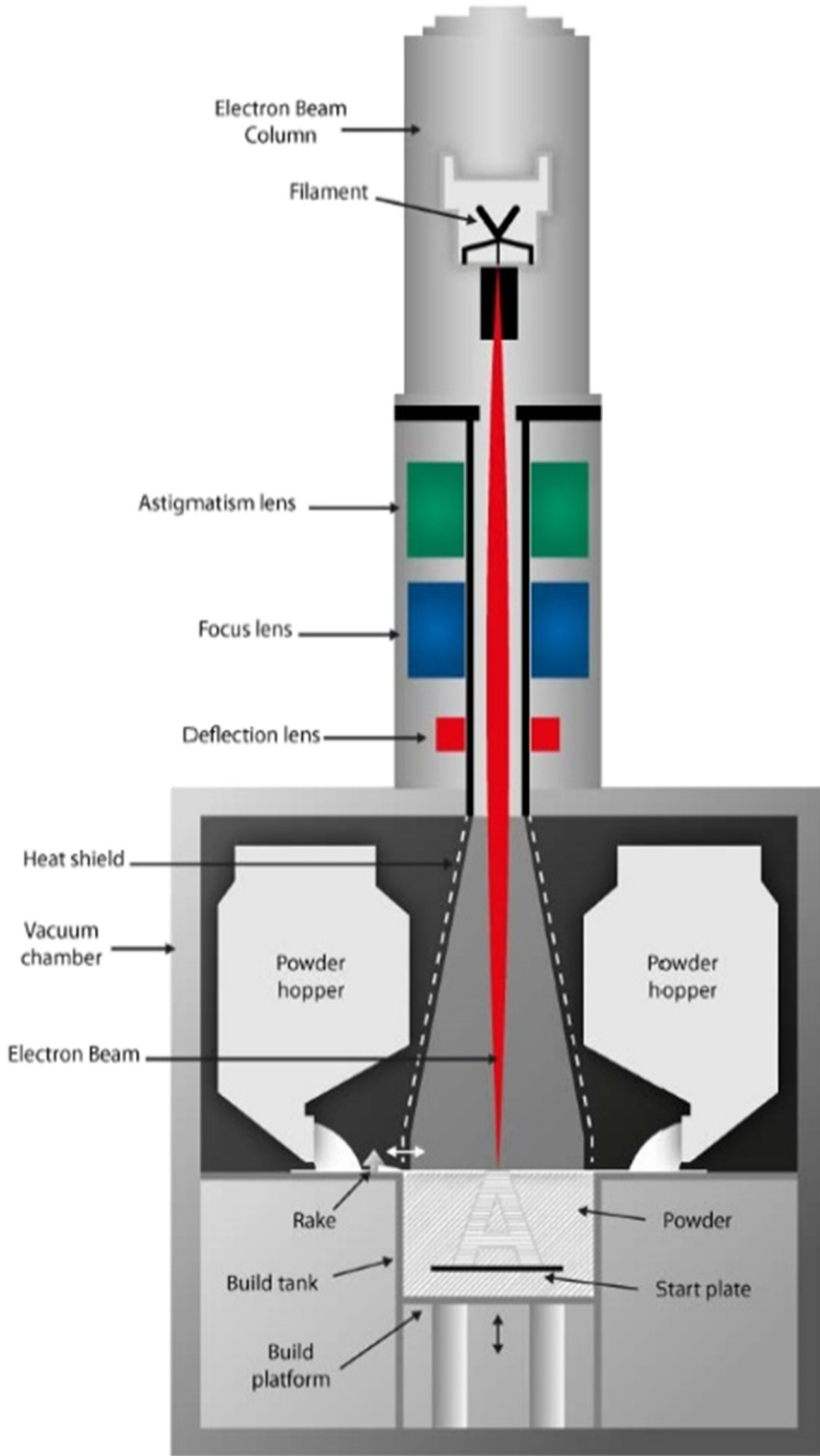


Fig. 4. Schematic of EPBF process; available on internet [25,31].

in this paper. For each process parameter set, therefore, the corresponding AM process is labelled accordingly.

4.1. Key process parameters and their effects on relative density

4.1.1. Hatch spacing to spot size ratio

The ratio between hatch spacing and spot size has major effects on process stability and the regular density when LPB is used [33]. As

seen in literature summary represented in Fig. 8, the majority of the work uses hatch spacing and spot size for analysis. According to Nakamoto et al. [34], highly dense part is obtained while hatch spacing is atypically low and heating depth is high at low energy density. Also, Mertens et al. [35] achieved good results with large hatch spacing and unusually high energy density, while increasing process speed with the available laser power. When hatch spacing is reduced, re-melting of solidified region is a strategy to maintain density despite high scan

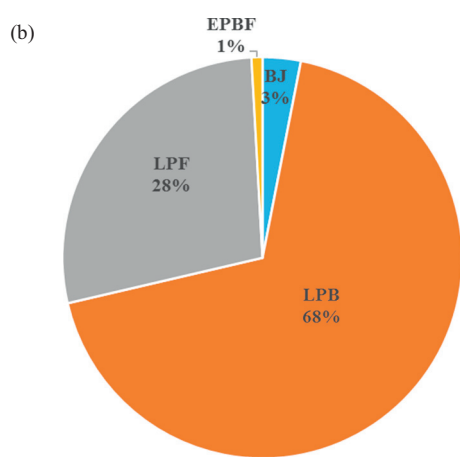
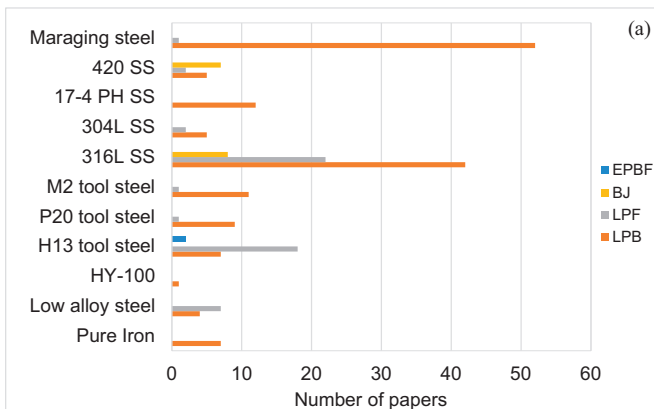


Fig. 5. (a,b) Relative emphasis of steels reported in the literature using various AM processes.

speed [36]. Fig. 8 indirectly explains the role of laser beam tracing overlap through the ratio between hatch space to spot size and its role on the relative density. Although the plot does not represent other main process parameters used for generating the densities, it implies that a wide range of densities is achievable while the average hatch spacing to spot size ratio is mainly set from 0.6 to 1.5.

4.1.2. Energy ratio

A consensus in the literature is that some measure of energy density is one of the best predictors for parts relative density for both LPB and LPF. A variety of energy density measures are used in the literature with a volumetric density approach. Volumetric density may have the advantages that it can be normalized against material enthalpy to be used for the comparison of multiple materials. However, some arguments have been made that the melting of multiple layers and also key-hole shape of the melt pool invalidates the use of layer thickness for the vertical length scale parameter [43]. This is backed by the observation in the next section that the layer thickness is highly correlated with optimum heat pulse depth. It is expected that the melted volume does not directly correspond to the cube defined by Volumetric Energy Density (VED), but that melted volume will scale fairly linearly with the volume of this cube for successful recipes [44,45]. However, the specific energy used mainly for LPF [32] and also used for LPB [43], [46–49] is more indicative of input energy from the surface irradiated by the laser beam [50].

$$E_{\text{specific}} = \frac{P}{v d} \quad (3.1)$$

where P is laser power, v is process speed and d is the spot size.

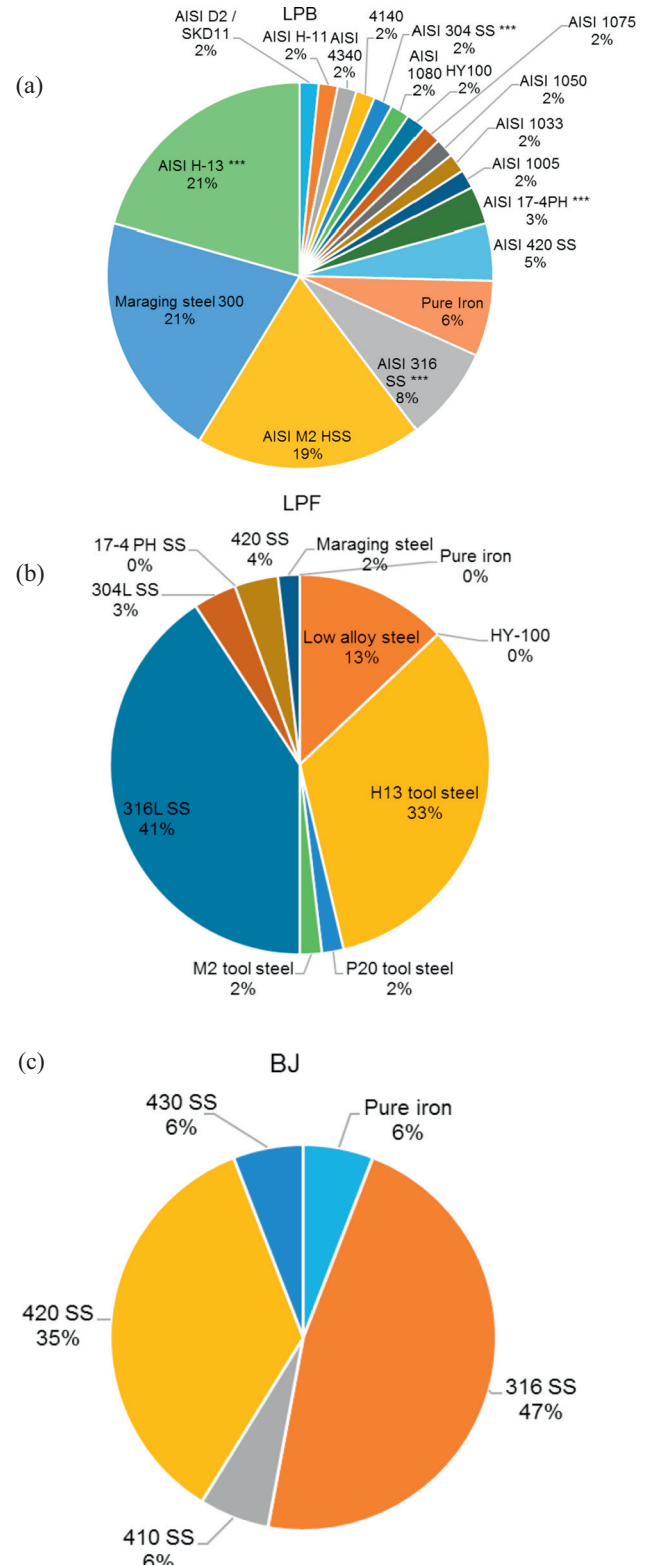


Fig. 6. Relative emphasis of steels reported in the literature using (a) LPB, (b) LPF and (c) BJ processes.

VED is more widely used for LPB techniques [27], [34], [39–42], [50–57], where three most important parameters are combined and justified based on the volumetric heat adsorption in powder bed; as defined below [58]:

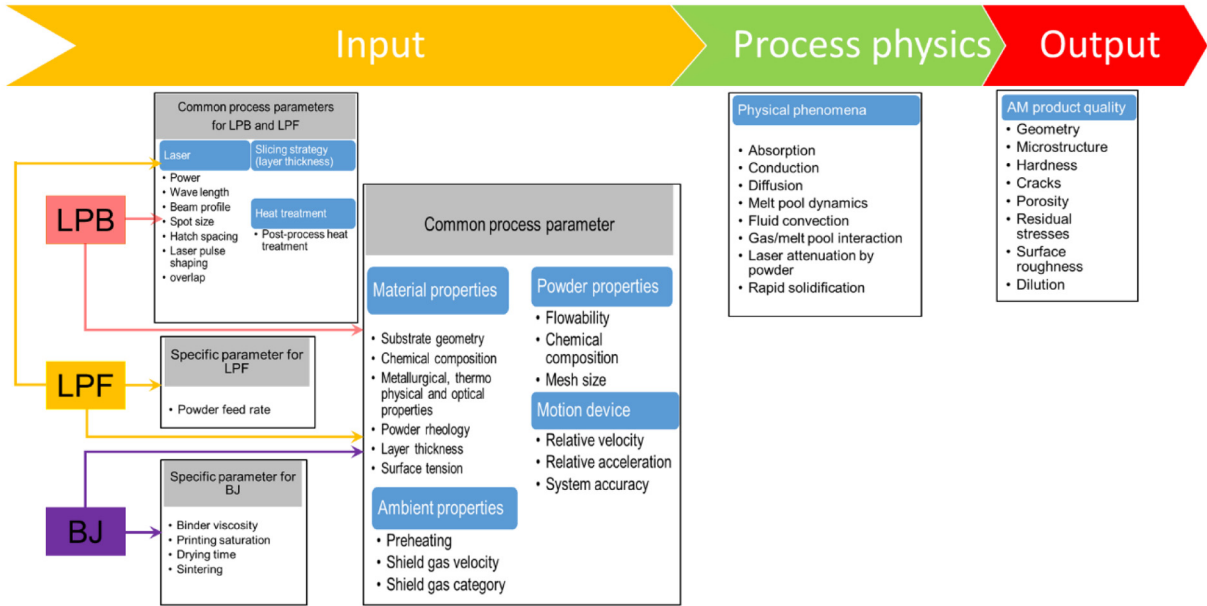


Fig. 7. A detail process design parameters for AM techniques.

$$VED_{Hatch} = \frac{P}{v s l} \quad (3.2)$$

where s is hatch spacing and l is layer thickness.

Spot size d provides an alternative definition more similar to specific energy,

$$VED_{Spot} = \frac{P}{v d l} \quad (3.3)$$

This is presumably related to energy requirements for fully melted materials within the proposed cube cells represented by hatch spacing, spot size and interaction length (i.e., speed/interaction time) [40,59]. Therefore, to compare across materials normalized VED, estimated enthalpy difference is used between room temperature (T_0) and the materials melting point (T_m).

$$\frac{VED_{Spot}}{\Delta H} = \frac{P}{v d l} \cdot \frac{\beta}{C_p,100^\circ C (T_m - T_0)} \quad (3.4)$$

where β is absorption factor, and C_p is heat capacity.

With the above four combined numbers, Fig. 9a–d are generated. This exercise has used C_p at 100 °C, which is readily available for all

materials and neglected the latent heat of fusion that normally covers small amount of total energy required for melting.

All plots, as shown in Fig. 9a–d, regarding density vs. energy, show similar trend; they reproduce well known result that energy input should be above the minimum threshold to achieve full density part. Normalized figure allows prediction that $VED_{Spot}/\Delta H$ should be >30 for full density part in steels. Based on the observed scatter, it is apparent that other factors are significant. Elevated value for enthalpy ratio suggests that heat transfer is very significant for the chosen process parameters. Also, precise value for required energy density is influenced by powder particle size distribution [51,52,60]. Moreover, from the literature, it is evident that high energy density reduces dimensional control making a hard process optimization procedure to compromise between specimen dimensionality and porosity [42].

4.1.3. Surface tension

In both LPB and LPF, surface tension plays an important role as it dictates capillary and wetting forces and also represent if the AM process is a diffusion based process or convention based. From [32], surface tension number is defined as,

$$S = \frac{(d\gamma/dT)qd}{\mu v k} \quad (3.5)$$

where $(d\gamma/dT)$ is the thermal surface tension gradient, q is the laser flux, d is the spot size, μ is the dynamic viscosity of the melt, v is the scan speed and k is the material thermal conductivity near its melting point.

For $S \leq 45,000$, surface tension is negligible. This is one of the recommended non-directional parameters which is closely related to Marangoni number [38,61]. In the literature, surface tension gradient and melt viscosity data is only readily available for pure iron, whereas viscosity estimates may be available for alloys via a generalization of the Andrade equation [62–64]. A tenuous approximation of surface tension is possible via thermodynamic approaches [65], however as atmospheric interaction is expected to be very significant (for both O₂ & N₂) [38,61,65,66], accurate estimations should include atmosphere data which is not readily available. Unfortunately, significance of surface tension cannot be adequately/comprehensively evaluated from the literature due to the factors mentioned above.

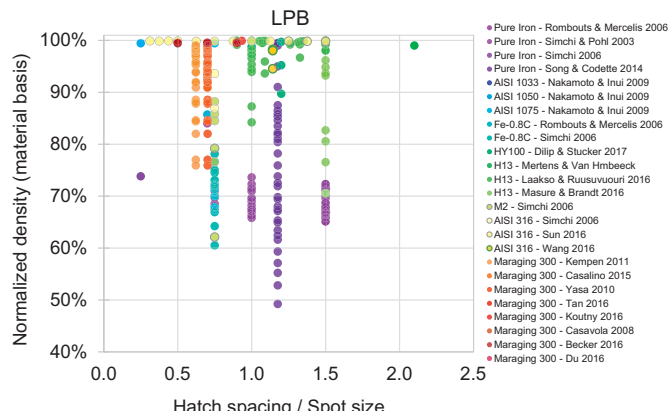


Fig. 8. Effect of hatch spacing/spot size on the density of ferrous alloys in LPB process [33–35], [37–42].

4.1.4. Dimensionless heating depth ratio (HDR)

To incorporate material properties and the heat penetration depth that would represent the keyhole depth into the analysis, the authors propose a new combined number called “dimensionless depth”. The one dimensional transient model is formulated as: [67,68],

$$T(z, t) = \frac{P \beta}{A k} \sqrt{4\alpha t} iefc \left[\frac{z}{\sqrt{4\alpha t}} \right] \quad (3.6)$$

where A is spot area, z is distance from surface, t is laser interaction time, α is thermal diffusivity, z is vertical axis, P is laser power, k is thermal conductivity and β is absorption factor. While, 90% of temperature change occurs within 1 scaling parameter of surface [67], the interaction time can be expressed by d/v where d is the spot size diameter [61]. The heating depth can be obtained when the limit of Eq. (3.6) approaches zero. This results in the following equation representing the heat penetration depth:

$$\text{HeatedDepth} = \sqrt{4\alpha \frac{d}{v}} \quad (3.7)$$

A logical dimensionless combined process parameter may be proposed through a ratio of the above equation and layer thickness, leading to a parameter so-called heating depth ratio (HDR).

$$HDR = \frac{\sqrt{4\alpha \frac{d}{v}}}{l} \quad (3.8)$$

The relative density versus HDR data from the literature is plotted in Fig. 10a. From the data available in the literature, it is apparent that, all successful authors are operating with heating depth greater than layer

thickness. Therefore, an HDR of 1.5 appears to be a good guideline for full density parts, as shown in Fig. 10a. Also the low part density at high VED generally correlates with large HDR (long interaction times) as seen in Fig. 10b and c. Fig. 10c zooms into a narrower range of HDR. From the Fig. 10b and c, it is seen that the central trend VED requirement appears to increase with increasing HDR [37]. There are however, a few outliers (reported density approximately above 99%) that may be attributed to the fact that the operating in a significantly different mode with respect to hatch spacing [26].

4.1.5. Drying time (BJ process)

In the BJ process, after printing of each powder layer, the print bed needs some time to be dried using resistive heater, known as ‘drying time’. To prevent blocking at the print head, it simultaneously shifts to a clean tank to remove extra binder materials. If the drying time is not adequate, print head may be blocked, which significantly reduces the surface quality of the final part [24]. Moreover, as demonstrated in Fig. 11, at short drying time, binder infiltrates only into the top thin layer leaving more pores in the green part, which leads to a higher porosity and a higher shrinkage in the sintering process [24]. Drying time should be long enough to achieve satisfactory green strength [69].

As depicted in Fig. 12, a drying time ranging from 10 to 20 s is adequate to promote sufficient green strength and higher relative densities compared to the 60 s drying time. Moreover, excessive drying time causes higher solidification and shrinkage rate, which eventually increases the production time and electric power consumption [24].

However, drying time is also determined by the choice of binder. For example, diethylene glycol (DEG) binders have a longer drying time of about 30 s/layer, while phenolic binders do not require drying. Therefore, drying time (t_d) is defined as a function of powder thermal conductivity (k), binder saturation (S), and surface area (A), as expressed in

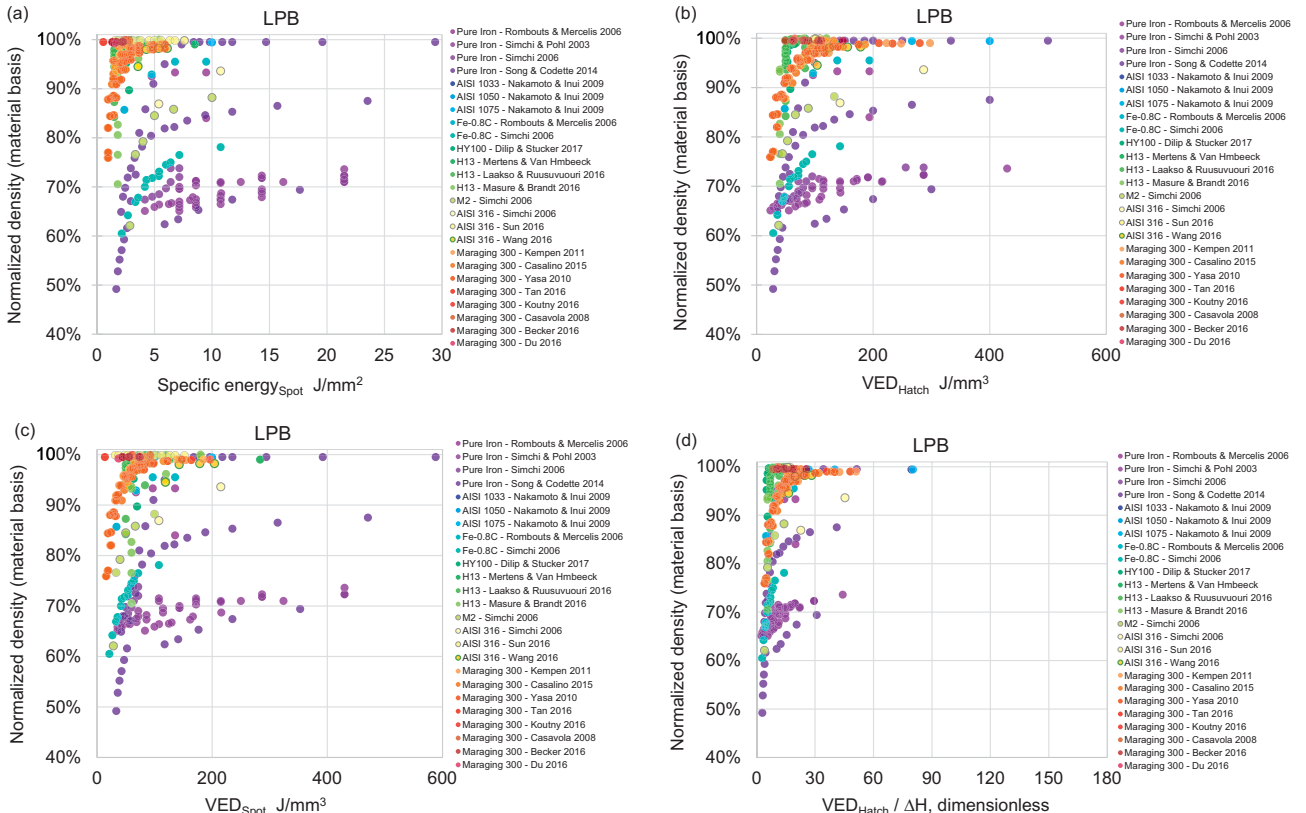


Fig. 9. Relative density vs. energy for various ferrous alloys, (a) relative density vs. specific energy, (b) relative density vs. hatch based VED, (c) relative density vs. spot based VED, (d) VED/ΔH [33–35], [37–42].

Eq. (3.9). Thus, powders with poor thermal conductivity, higher binder saturation, and larger surface area need longer drying time (t_d) [70].

$$t_d \propto \frac{SA}{k} \quad (3.9)$$

4.1.6. Printing saturation (BJ process)

Printing saturation or binder saturation in BJ is the ratio of air space between powder particles (V_{air}) and binder volume (V_{binder}) [24,72]. In simple words, saturation explains the amount of binder to be deposited in the period of printing, and it determines the printing quality and final

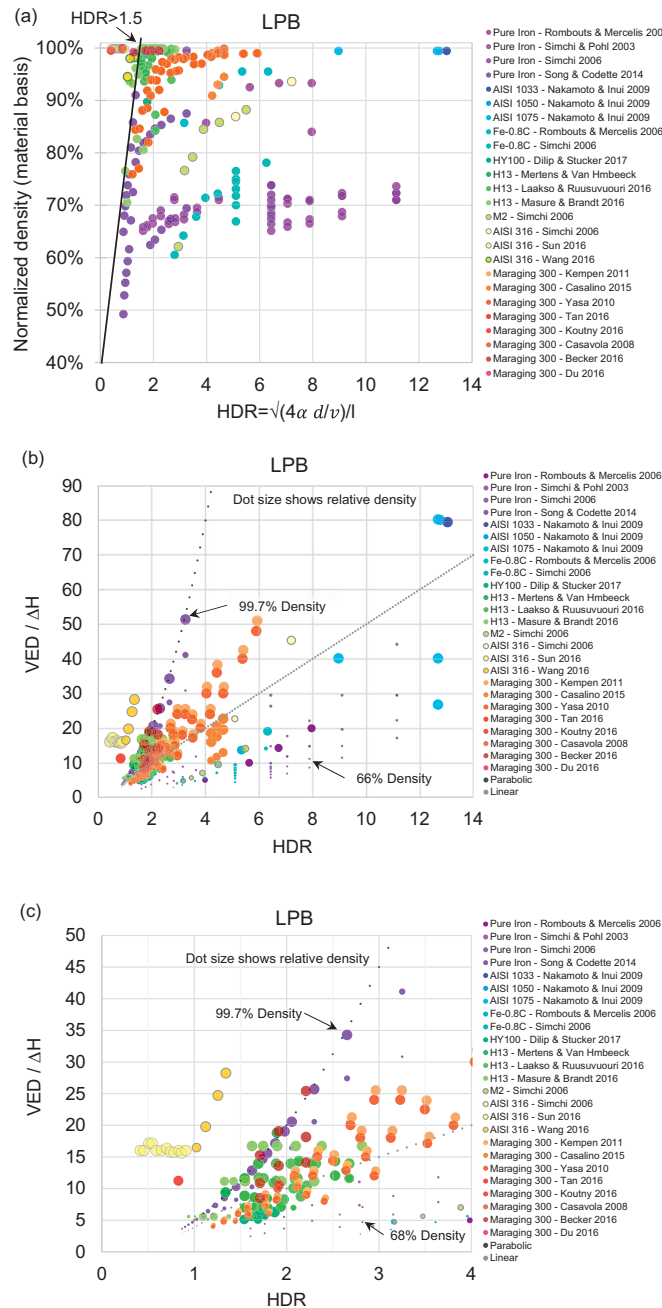


Fig. 10. Relative density vs. heating depth ratio for various ferrous alloys, (a) normalized density vs. dimensionless depth, (b) VED/ΔH vs. heating depth ratio, (c) zoom in the plot of (b) [33–35], [37–42].

sintered density, which is defined by the following equations [24,72].

$$S = V_{binder}/V_{air} \quad (3.10)$$

$$V_{air} = \left(1 - \frac{PR}{100}\right) \times V_{solid} \quad (3.11)$$

where V_{solid} is the volume of solid particles in a defined envelope. Here, PR is the packing density of the powder bed, as defined below, [24].

$$PR = \frac{V_{powder}}{V_{powder} + V_{air}} \quad (3.12)$$

Therefore, optimal binder saturation is selected based on powder packing factor and wettability [70]. In order to yield sufficient green part strength and quality, satisfactory binder saturation is needed [72]. If not satisfactory, some powders fall off from the part, leading to a bad surface quality (zigzag surface), as shown in Fig. 13a [24]. On the other hand, low level saturation can result in inaccurate geometry and low sintered density leaving porosity after binder burn-out. The excessive powder bonded to the surface makes some swells on the surface leading to bad surface roughness as depicted in Fig. 13b.

Oversaturation also leads to unwanted wetting of the bed, thus sticking powders to the roller and subsequent inhomogeneous powder bed [70,72]. It has been shown that spherical particles use binders more efficiently by having small necking area between particles leading to comparatively low binder saturation levels [72]. Our review shows that compared to the 3D printed bio-implants, which are designed to possess higher porosity, lower binder saturation level gives rise to higher relative density for ferrous alloys. The effect of printing saturation on relative density for the 3D printed parts is shown in Fig. 14; however, we do not have enough data points to be able to draw a concrete conclusion for ferrous alloys.

4.2. Common key process parameters for all three AM processes

4.2.1. Powder characteristics

Powder properties such as flowability, compressibility, tap density, size, shape, distribution, etc. have significant effects on the final AM made parts [73,74]. Most research studies on the LPB processing of maraging steels have been focused on the use of gas atomized powders that are usually expensive. Hoeges et al. [75] investigated the impact of different atomization methods on the quality of LPB processed parts. They employed high-pressure water atomization to produce maraging steel (Ni 17–19, Co 8.5–9.5, Mo 4.5–5.2, Ti 0.6–0.8, Al 0.05–0.15, C ≤ 0.03, Cr, Cu ≤ 0.5, Si, Mn ≤ 0.1, S,P ≤ 0.01 wt%) with niobium instead of titanium. It is beneficial to replace titanium with niobium, because of its lower affinity to oxygen preventing the formation of stable solid oxides which tend to adhere to the pouring nozzle. Moreover, it optimizes the flowability of maraging steel, and minimizes oxide inclusions during the LPB process. The detail of the formation of oxide inclusions due to the oxide contamination of the powder is focused in LPB processed 17-4

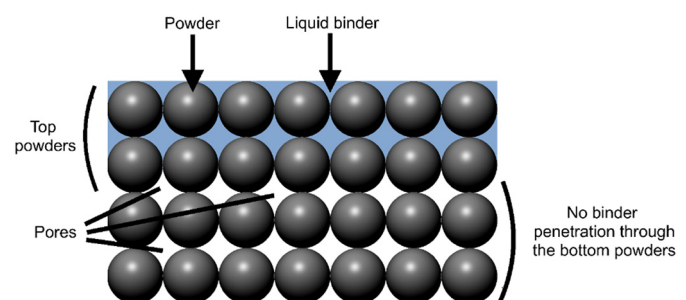


Fig. 11. Short drying time leads to thin binder penetration [24].

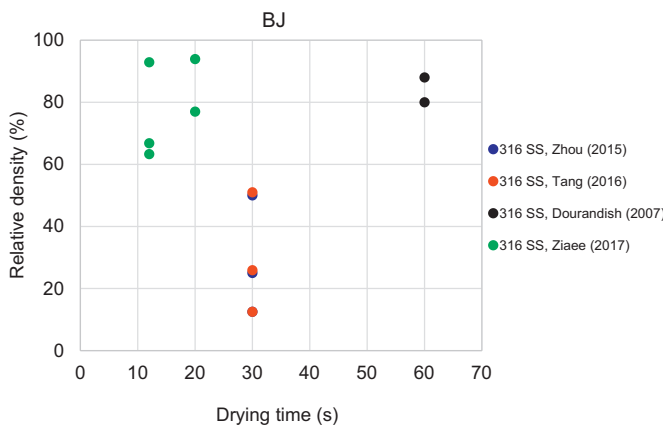


Fig. 12. Effect of drying time on relative density of 3D printed parts [21,22,69,71].

PH steel [76]. The researchers addressed the major drawbacks associated with water atomized powder characteristics including irregular particle shape, lower tap densities, and oxidized surfaces. More importantly, there is a slight difference in the avalanche angle between water atomized and gas atomized maraging steel powder (1°). The smaller the avalanche angle, the better the processability of the powder; therefore, the powder will spread more smoothly during the deposition of a thin powder layer [75]. It should be noted that water atomized pure iron powder (WA-Fe-Powder) with avalanche angle of $\sim 54^\circ$ has shown sufficient flowability to be processed with additive manufacturing machines, and is documented as a minimum requirement for the processability in LPB. In addition, Latenieur et al. [73], worked on WA-Fe based powder using the LPB process, where process parameters were optimized to improve density and mechanical properties of the 3D printed parts. While gas atomized maraging steel has been most widely used for additive manufacturing [75,77], there are not many papers associated with water atomized powders. Nevertheless, the mechanical properties of the water as well as gas-atomized powders for a few steel alloys are compared in Table 1 [75].

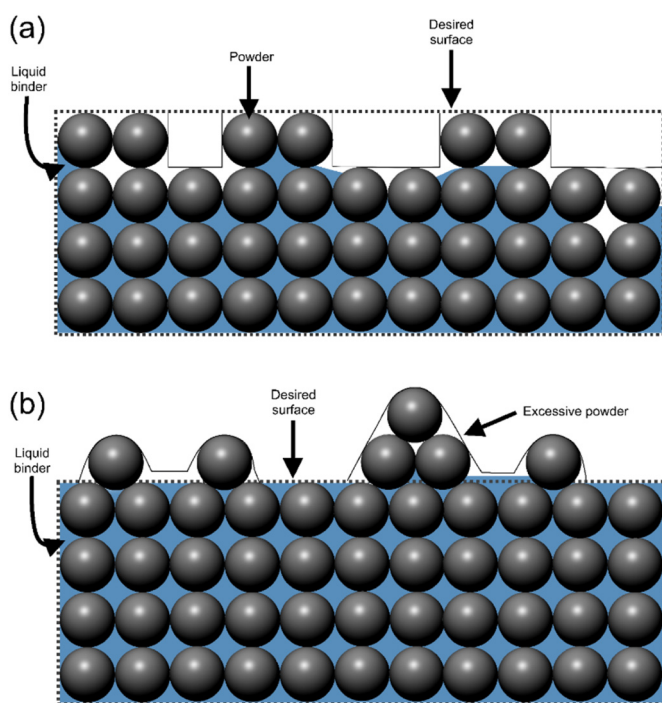


Fig. 13. (a) Low-level saturation leads to powder loss, and (b) over-saturation leads to excessive powder bond [24].

In the BJ process, powder characteristics such as particle size, morphology, density, tap density, and flowability affect the final properties of the AM components. For example, spherical particles are mostly preferred, although irregular particles are able to improve green strength without achieving uniform density. Furthermore, in order to reach good packing of powder layers and high green density, tap density of the powder should be satisfactory. Insufficient tap density leads to high porosity levels in the green components and subsequent high shrinkage during sintering, which makes it difficult to reach desired density and tolerances of the final component [78].

The powder particle size distribution (PSD) has a significant influence on the entire BJ process from making green parts to post processing. Dourandish et al. [69] showed that sintering behavior of complex-shaped biomedical parts of 316 L SS significantly depends on the PSD. Solid state sintering governs the densification of 316 L SS powders. However, using fine 316 L powder, after sintering the total amount of porosity is low (~12%) with relatively small pores. When coarse 316 L particles are used, a higher total porosity (~20%) with a significant amount of large (~100–300 μm) pores is observed. Moreover, the amount of carbon pick-up during de-bonding and sintering depends on the powder particle size. The amount of carbon pick-up for fine powder is 0.2 wt% compared to 0.07 wt% for coarse powders, which is attributed to the lower layer thickness and lower amount of binder used for 3D printing [69].

4.2.2. Layer thickness/layer slicing strategy

In steel alloys fabricated by LPB, higher layer thickness causes a decrease in relative density as extracted from published sources and shown in Fig. 15. Consequently, layer thickness influences the macro-hardness together with the scan speed [77,79,80]. To make the plot more representative, different color is used to focus different laser power, scanning speed, etc.; however, the plot is normalized around layer thickness.

Some studies have been carried out to control the three-dimensional deposition by the LPF technique [32,89–91]. It is known that if the process parameters are not completely optimized, the final layer thickness might be dissimilar to the original setting value, even with the use of height control device. To find out the impact of process design parameters on the layer thickness of H13 tool steel, actual layer thickness was measured. The dissimilarity in the final layer thickness from the setting values in terms of thickness error distribution is shown in Fig. 16a. It is seen that to achieve a good dimensional accuracy in H13 tool steel, layer thickness might be fixed as 0.254 or 0.381 mm. Also according to results shown in Fig. 16b, superior dimensional accuracy can be obtained by high powder mass feed rate. Therefore, in this process, both layer thickness and porosity greatly depend on powder mass feed rate and overlap percentages with a constant laser input power.

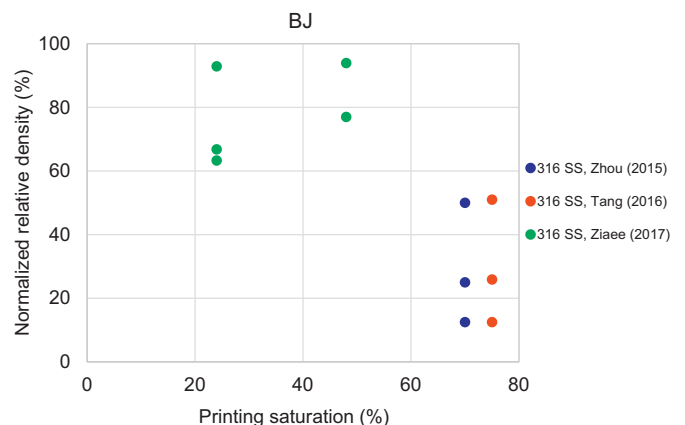


Fig. 14. Effect of printing saturation on relative density of 3D printed steel parts [21,22,71].

Table 1

Average avalanche angle of water and gas atomized powder and mechanical properties of LPB processed maraging steel after age hardening at 490 °C for 6 h [75].

Material	Avalanche angle (°)	Density (g/cm ³)	UTS (MPa)	Elongation at break (%)	Hardness (HRC)	Impact energy (J)
GA-maraging 300	47.5	8	2006	3.1	52	7
WA-maraging 300	48.5	8.04	1793	1.4	43	5

The larger powder mass feed rate causes greater porosity, but the possibility of actual layer thickness formation is enhanced [90]. However, in case of deficiency of energy input, the overlap of the melted track should be >50% [90]. By contrast, in another research, it is claimed that 40% overlap in H13 tool steel gives the best combination of layer thickness and maximum volume of deposition rate [91]. It has been reported that the layer thickness in LPF fabricated products shows a key role in the final parts microstructure. In particular, for H13, by increasing the layer thickness or specific energy, the primary dendrite widths are enhanced. In addition, the finer grain and the higher cooling rates can be obtained by a lower specific energy, lower layer thickness but by a higher speed [91]. For H13 tool steel, it is then shown a progressive relationship among the outputs of layer thickness and specific energy with powder mass feed rate [91].

An interesting strategy to achieve dimensional accuracy is by layer slicing. In the LPF process, the CAD design part is sliced into parallel layers and synthesized in a layer-wise method. This method is only applicable to surfaces where normal vectors are not aligned to 0° or 90° with the process direction. Therefore, in spite of a feasible solution of this method, the staircase effect (a surface with step-like features) still remains [92]. There are some studies reflecting on the slicing procedure to reduce staircase effects, such as the volumetric difference between layers [93] and controlling layer thickness [94]. However, these methods are considered for fixed direction deposition processes and do not entirely remove the staircase effect. There are other methodologies such as, multi-axis processing to minimize the staircase effect. In this method the slicing direction rotates to 90°, in case of an overhang structure instead of taking the classical parallel slicing procedure [95,96].

It has been reported that layer thickness in BJ is the most critical factor that affects the integrity of the part. It also determines the possibility to design of smallest feature size [24]. High layer thickness results in unbounded layers, while applying a thin layer leads to pushing away of the printed layers during spreading of the next powder layer [69]. Generally, it is believed that better end-product properties are achieved when applying a low layer thickness, while building time will considerably increase as a tradeoff [24]. It is also reported that layer thickness must be bigger than the diameter of the largest particle [70] or at least one diameter of the largest particle in the powder feedstock [15]. In this review, layer thickness/average particle size is defined as one of

the key parameters that need to be identified and controlled; however, the capability of the BJ machine constrains the choice of the layer thickness. Our review shows that higher relative densities are attained when the ratio of layer thickness to average particle size is in the range of 2.3 to 3.3, as shown in Fig. 17. It should be noted that to reach a firm conclusion more data points are necessary.

4.3. Specific process parameter for BJ

4.3.1. Binder burnout and sintering

The binder used in BJ AM technique is typically a glycerol based binder, which mainly occupies the interstitial spaces among the powder particles to hold the powder together in the desired shape. In the post-processing step, green part is subjected to binder burnout followed by sintering process, normally in a single step. Particle size distribution and alloy chemistry have a direct impact on sintering kinetics. In solid-state sintering, particle diameter is the main governing factor [70]. Conversely, in super solidus liquid-phase sintering regime, both particle diameter and liquid volume fraction control the sintering kinetics. Liquid volume fraction is the overriding factor. The alloy chemistry is a significant factor in selecting the optimized process temperature [70]. It is important to determine a correct sintering set temperature to obtain full density and sufficient mechanical properties. Frykholm et al. [78] suggest that 316 L SS green parts are required to be sintered at a temperature close to solidus temperature (1360–1380 °C) and in

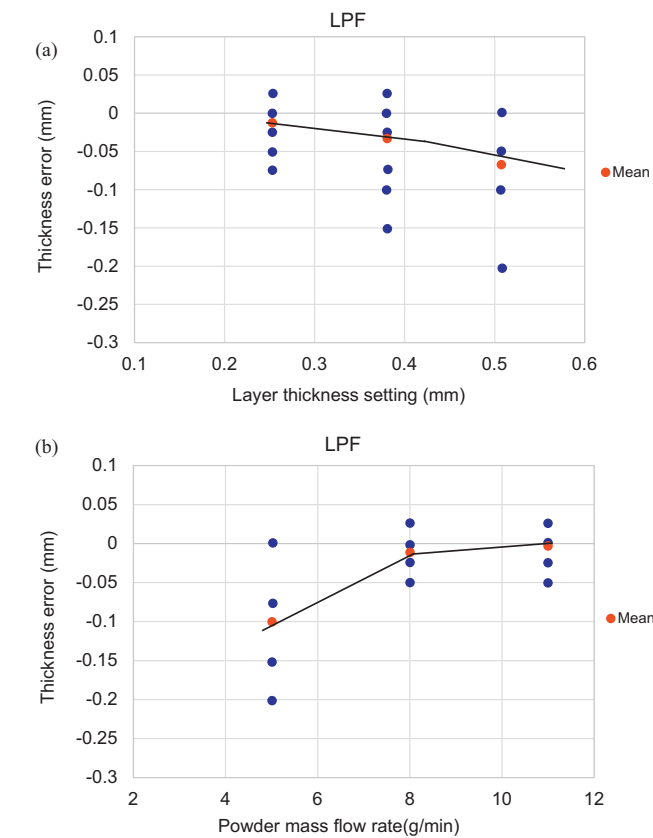
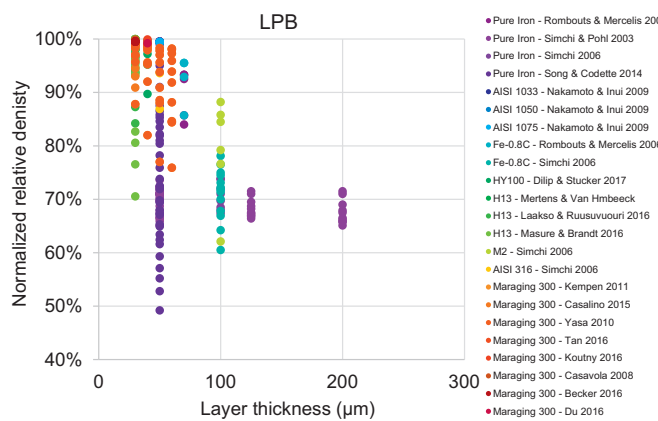


Fig. 15. Influence of layer thickness on relative density in LPB for different steel alloys [56,77,81–88].

Fig. 16. Impact on layer thickness error, in relation with, (a) layer thickness value, and (b) powder mass flow rate for H13 tool steel processed with LPF, adopted from [90].



vacuum with a partial pressure of Ar. This setting decreases the level of Cr loss from the surface, and preserves the corrosion resistance of the steel. In addition, sintering at high temperature leads to the formation of delta-ferrite, which is favorable for mechanical performance and corrosion resistance. After cooling, some residues of ferrite remain in the material; however, the impact of the low amount of delta-ferrite (up to 8%) is somewhat negligible. To yield higher densities, the sintering temperature could be increased, but this is not generally recommended as the higher temperature might affect tolerances. In this review, sintering temperature/melting temperature (T/T_m) is defined as a key parameter for post-processing of components processed through binder jetting 3D printing. From the review work as plotted in Fig. 18; it is stated that higher relative densities are achieved when the T/T_m is in the range of 0.8–1, with the highest relative density of 99.8 attained at $T/T_m = 0.89$. Vacuum sintering is another option to improve the final density by eliminating trapped air inside the samples [98].

4.3.2. Sintering additives

In BJ, it is known that incorporation of sintering additives into the base material enhances the densification and final structural integrity [97]. Sun et al. [99] demonstrated the effectiveness of adding silicon nitride (Si_3N_4) on density, dimensional accuracy, and mechanical properties for 3D printing processed 420 SS in a series of sintering conditions. From their work, it is evident that the 3D printed parts with additives can achieve a high relative density (~98%) and excellent mechanical properties (~200 GPa) with a slight distortion after sintering at 1300 °C. However, because of the large amount of silicon nitride (12.5 wt% ~28 vol%), the part is not considered to be a 420 SS anymore.

Among the various sintering additives, boron (B), carbon (C), and nitrogen (N) are the most effective elements to reduce the liquidus temperature, as shown in Fig. 19 [98]. For example, addition of 4 wt% B in iron (Fe) can reduce the eutectic point to 1174 °C in Fe-B phase diagram [98]. The sintering process is enhanced by the transformation of a solid to a liquid phase. With the adequate volume of liquid phase in the green part, sintering temperature is reduced and the sample density is improved whereas the excessive formation of liquid phase substantially destroys the sample shape. In powder mixture of SS and B, the liquid phase starts to occur from the location of high concentration of B and dissolves the neighboring SS powders as the liquidus temperature lowers the sintering temperature. However, the higher concentration of sintering additives causes the formation of extensive liquid phase to lose the intended sample shape and can lead to the formation of pores [97].

4.3.3. Infiltration of nanoparticles into porous BJ printed parts

Another strategy to improve the density of BJ parts involves the incorporation of nanoparticles into the inkjet fluid to fill the void spaces

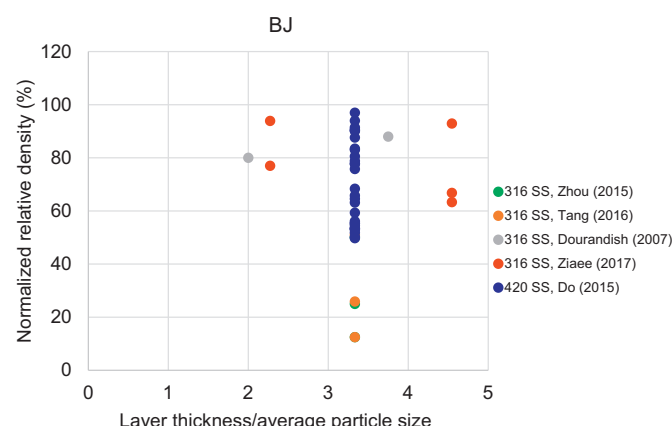


Fig. 17. Effect of layer thickness/average particle size on relative density of BJ 3D printed parts [21,22,69,71,97].

between the powder particles. However, nanoparticles may have impact on viscosity of the binder being jetted to make inkjet deposition challenging or impossible [18]. Following this approach where nanoparticles behave as a sintering additive, objects with densities up to 86.8% are achieved as void filled nanoparticles increases the packing factor of the powder bed [101]. Addition of metal nanoparticles will improve mechanical properties and dimensional accuracy, decrease the sintering temperatures, and offer multi-functional aspects to 3D printed parts; for example, thermal and electrical conductivity [101].

The chosen nanoparticles should be compatible with the composition of final parts, thus not negatively impacting the final material properties. Increasing the packing factor of the powder bed by incorporating nanoparticles was first adopted by Crane et al. [102], where iron nanoparticles dispersed in an organic solvent were employed to improve the quality of 3D printed 410 SS. Iron nanoparticles are excellent candidate for steel parts since addition of several percent more iron nanoparticles impacts slightly on the part composition.

During heating, the nanoparticle deposits, and sintering of nanoparticle toughens the bonds between particles, followed by shrinkage of deposits, which is schematically shown in Fig. 20. The differences in shrinkage kinetics between the associated powder and the products can cause cracks, which can be repaired by reapplying the nanoparticles, then the newly formed cracks are smaller than the previous ones.

In another attempt, Elliott et al. [101] infiltrated 316 L stainless steel 3D parts by 316 nanoparticles. The nanoparticles were suspended in water mixed with two liquid polymer carriers, diethylene glycol (DEG) or ethylene glycol (EG), and deposited drop-wise to a sintered 3D printed binder jetted part. This process depends on pH and molar ratio of water and polymers. The higher polarity of DEG compared to EG at a pH level of 11 and a DEG/H₂O molar ratio of 1:4 leads to the enhancement of dispersion and infiltration of nanoparticles in the 3D parts and subsequent increase in mass and density followed by sintering.

Bailey et al. [18] produced a nanoparticle, binder, and powder system that is more comparable to the BJ process by suspending copper nanoparticles in binder and adding the mixture to the 430 SS powder. Nano copper was selected only because it provides contrast with powder particles, which helps to distinguish the location of the nanoparticles inside the part. The quantity of nanoparticle parent solution is determined based on the parent solution's packing factor and targeted fraction of void space between skeleton particles [18].

However, incorporation of nanoparticles introduces dimensional instability, because of shrinkage and creep; especially at high infiltration temperature of steel [102]. To minimize creep deflections during infiltration, parts were packed with refractory powder; which is also challenging for complex shaped parts. Also, the shrinkage difference between the packing powder and parts may cause tearing during sintering. Moreover, at higher nanoparticle contents, a substantial foaming or void expansion occurs during curing. This is because the

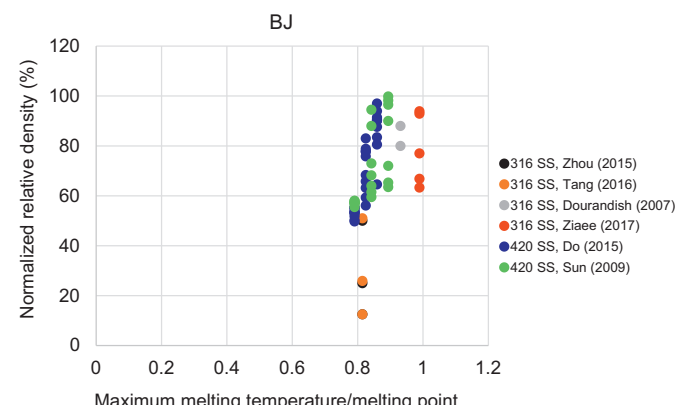


Fig. 18. Influence of maximum sintering temperature/melting point on relative density of 3D printed parts by BJ [21,22,69,71,97,99].

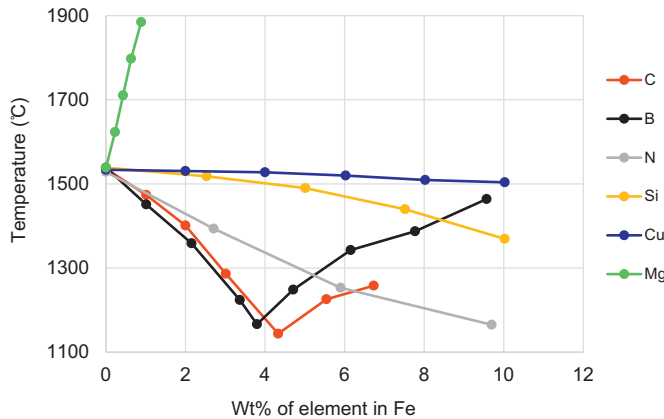


Fig. 19. The liquidus lines for various elements in Fe [100].

nano-particles occupy the voids in between the bigger particles and prevent the solvent in the binder from escaping, thus creating large cavities/visible porosities in the parts. On the other hand, the presence of nano-particles becomes more evident between the larger SS particles leading to an increase in the sintering of SS due to the nano-copper behaving as a sintering aid [18].

4.3.4. Liquid metal infiltration

Another route of densification is by the infiltration of liquid-metal, with negligible dimensional changes. Therefore, in BJ technique, metal parts are usually infiltrated with a low melting point material such as bronze in order to remove residual porosity and obtain full density [97,103]. This manufacturing process counts on capillarity of the infiltrant material to be absorbed by pores on the surface [103]. Infiltration changes the nature of the material while filling the pores of the printed material which slightly enhances the mechanical properties including hardness, elastic modulus, yield strength, etc. [17,97].

Sachs et al. [103] made an attempt to fabricate injection molding tooling of 316 SS, where cooling channels were conformal with the molding cavity. They introduced a new technique called “stilt infiltration” which assures that the channels would be free of infiltrant with almost no under-infiltration or over-infiltration of the part and clogged passages. Also in the process, the sample was raised on the top of the infiltrant surface, which created a negative pressure in the infiltrant causing the infiltrant to be kept out of the cooling channels. From this approach, it is assured that passages will not be filled above some

critical range. During infiltration, channels should be placed horizontally, in a way to maintain the capillary rise between parallel walls. If the infiltrant angle with respect to the walls is close to zero, then the capillary rise is given by the following [103],

$$h = \frac{2\gamma}{\rho g \omega} \quad (3.15)$$

where ω is the spacing between the walls, for the molten infiltrant, h is the capillary rise, γ is the surface tension, ρ is the density, and g is the acceleration of gravity.

Cordero et al. [104], also fabricated a dense ferrous alloy by infiltration of molten bronze, which showed higher rupture strength by eliminating stress concentration between the particle necks.

The optimum saturation of infiltrant liquid is significantly important to manufacture a standard green product. If the liquid infiltrant exceeds the saturation level, dimensional accuracy will be destroyed by the migration of excess infiltrant. On the other hand, lack of infiltrant can cause weak bonding between particles. Therefore, precise estimation of infiltrant saturation is vital for the design of BJ printed parts.

5. Potential defects

5.1. Cold and segregation cracking

Cold cracking susceptibility is proportional to hardenability, where carbon equivalent (CE) is defined as [105]:

$$CE = \%C + \left(\frac{\%Mn + \%Si}{6} \right) + \left(\frac{\%Cr + \%Mo + \%V}{5} \right) + \left(\frac{\%Cu + \%Ni}{15} \right) \quad (4.1)$$

The high carbon steel contains a continuous phase like martensite, whereas in SS, continuous phase is often retained austenite, which prevents cracking. Cracking is worst in M2 and H13 steel that can be blocked by preheating to partially or fully suppress martensite formation. In LPB, rapid solidification is insufficient to suppress segregation but generally results in fine microstructure. Also, low melting phase is sufficiently discontinuous to avoid segregation cracking. This type of phenomena is observed in high copper alloy 17-4 PH SS [106]. The crack formation is also reported in the LPB processed high silicon steel (6.9 wt%), which was influenced by higher laser energy input [45].

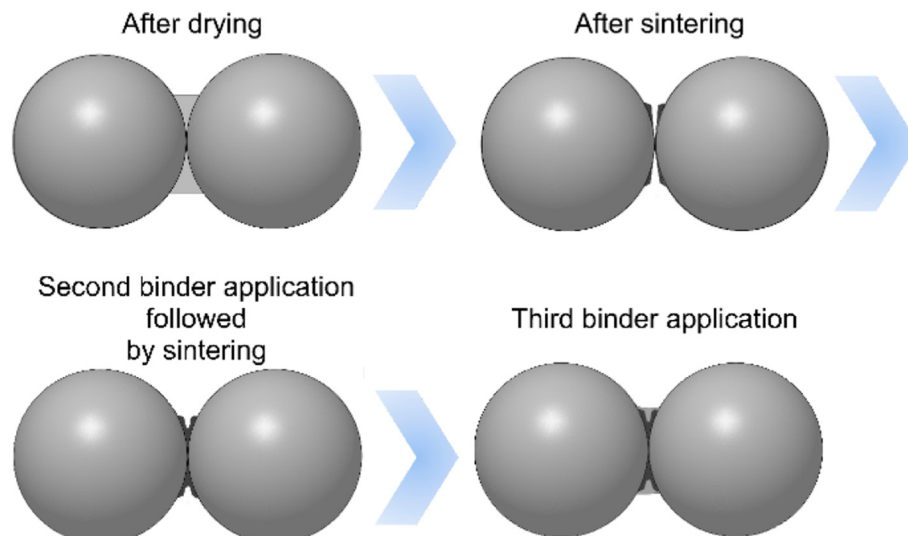


Fig. 20. Multiple application of nano-binder to enlarge the bonds and disappear the cracks generated during sintering [102].

The faster melting and solidifying rates in both LPB and LPF techniques result in a deposited layer with higher residual stresses and consequently cracking [107]. LPB introduces tensile residual stresses because of the localized input of high laser energy in a very short period of time, and together with the lower thermal conductivity of the powder, a higher temperature gradient is developed near the laser spot [45]. Consequently, the expansion of the heat affected zone is repressed by the neighboring material, which usually causes plastic compression. Again, during the cooling, the contraction affinity of the upper layers is neutralized by the subsequent layers, which cause tensile stresses that are major source of cracking.

In comparison between austenitic SS and low-carbon steels, the former is more sensitive to solidification cracking than the latter one because of their lower thermal conduction and higher thermal expansion coefficients. Moreover, some contaminants like sulfur and phosphorous have a profound impact on cracking in SS. Table 2 shows the cracking behavior of different water/gas atomized 316 SS powders linked with impurity amount. The cracking sensitivity becomes less by decreasing S + P + Si content. It is also claimed that, a considerable nitrogen value is harmful to solidification cracking [108].

5.2. Porosity

Generally, in AM, it is believed that the tendency of pore formation can be diminished (or controlled) by optimizing the process parameters, i.e. laser scan speed or laser power [109,110]. There are various reasons behind the formation of interlayer porosity including; (i) mismatch between mechanical properties of the underlying layer, (ii) mismatch between thermal elongation due to sharp temperature distribution in the deposited material, (iii) enclosed gas entrapped in the melt, (iv) chemical reaction between different feedstock etc. [111–113]. It was observed that low ductile materials show a greater tendency to interlayer porosity [112]. A recent study suggests that specified critical level of porosity and gas content in the starting powder has a profound impact on the interlayer porosity formation. Choi et al. [90] statistically investigated the pore formation in AISIH13 tool steel and concluded that the powder feed rate is a considerable factor, influencing porosity [114].

Primarily two types of porosity are considered: (1) gas porosity; resulted from encapsulated gas due to incomplete melting of particles with internal-porosity, and (2) lack of fusion (LOF) porosity due to voids that create among unmelted or incompletely melted powder particles. The former can be resolved by using powders free of gas porosity, while the later can be prevented by complete melting of the powder [115]. It is worth considering that LOF is the most detrimental flaw as it may act as a crack initiator as well as lead to a complete failure. Careful selection of process parameters should be considered in order to diminish crack formation and propagation [111,116].

Table 3 represents the impact of both laser power and powder feeding rate of H13 tool steel on pore formation in the LPF process. The results indicate that only powder feed rate is a crucial factor for the porosity formation in H13 tool steel. Also, as seen, in case of higher powder feed rate, porosity level can be reduced with increasing the laser power input. It should be noticed that achieving a desirable quality can be challenging. For example, obtaining actual layer thickness is more probable at a higher powder mass flow rate, but on the other hand, chance of pore formation is increased [90]. By optimizing the layer thickness of single clad tracks with adequate energy input, the porosity may be eliminated. In addition, choosing a suitable overlap between tracks can be another effective solution to reduce porosity.

A research work on H13 tool steel demonstrated that with a lower energy input, the overlap should be >50% [90]. In another work on H13, it is pointed out that acceptable layer thickness is <0.7 mm, and the ratio of energy/mass must be higher than 40 KJ/g to avoid pore formation [91]. In addition, the higher nominal specific energy can result in the lower pore/void formation. Also, Fig. 21 represents the specific

Table 2

In LPF, cracking behavior of various 316 SS powders related to impurity content, adopted from [108].

Different 316 SS powders	Fabrication method	S + P (Wt %)	S + P + Si (wt%)	N content	Cracking
316 SS-1	WA ^a	0.02	2.25	0.047	✓
316 SS-2	WA	0.125	1.445	–	✓
316 SS-3	GA ^b	0.023	0.553	0.062	✗
316 SS-4	GA	0.041	0.541	0.09	✓
316 SS-5	GA	0.035	0.475	–	✗
316 SS-6	GA	0.044	0.384	–	✗

^a Water atomized.

^b Gas atomized.

energy vs. porosity obtained from the literature on H13 tool steel with relevant normalized powder feed rate [117]. The normalized powder feed rate (ζ) is defined as:

$$\zeta = \frac{4m}{\pi d^2} \quad (7.1)$$

where, m is powder feed rate (g/s) and d is laser spot diameter on the substrate surface.

Table 4 shows the summary of the effect of various parameters on porosity level in different steels. The behavior of porosity in both 420 and 4140 low alloy steel has been investigated in several experiments.

For 420 SS, the linear mass density ($\frac{m}{d}$) which is the ratio of powder flow rate (m) divided by the laser traverse velocity ($v = \frac{d}{t}$) has been used to identify a proper combination of powder feed rate and laser traverse velocity to result in a fully dense part.

Fig. 22a shows that there is an optimal linear mass density, ($\frac{m}{d}$). At a lower value, no porosity is observed, and at a higher value, the porosity increases linearly with increasing linear mass density. For the 420 SS deposited on a 420 SS substrate, the critical linear mass density is 0.0115 g/mm to arrive at a full density part [115]. This optimal amount for 4140 SS on a 1045 steel substrate is approximately 0.018 g/mm, as shown in Fig. 22b. It can be seen that there are many combinations of powder flow rates and laser speeds to obtain a fully dense specimen. Values out of the optimal mass density range lead to lack of fusion porosity [115].

6. Microstructure development

6.1. General microstructural characteristics in AM ferrous alloys

In both LPB and LPF processes, the manufactured parts are usually pass through the complex thermal cycles; (i) rapid heating due to the absorption of laser energy, (ii) fast solidification of the melted region in the absence of heat source, (iii) substantial temperature gradients, (iv) accumulated heat and (v) reheating/recooling due to the laser energy in the adjacent layers/tracks. The frequent re-melting and re-solidifying progressions are continued when the subsequent layers are exposed to heat [10,120,121]. While non-equilibrium thermodynamics govern the physics of the microstructure formation in LPF and LPB, thermal cycle depends upon many process variables, hence predicting the microstructural characteristics of AM components, and the impact of process parameters on them, is still poorly understood.

Table 3

Influence of powder mass feed rate and laser power on porosity in H13 tool steel made by LPF [90].

Laser power (W)	1400			1200			1000		
Powder feed rate (g/min)	5	8	11	5	8	11	5	8	11
Porosity (%)	0.08	1	1.8	1.3	1.1	3	1	2.5	11

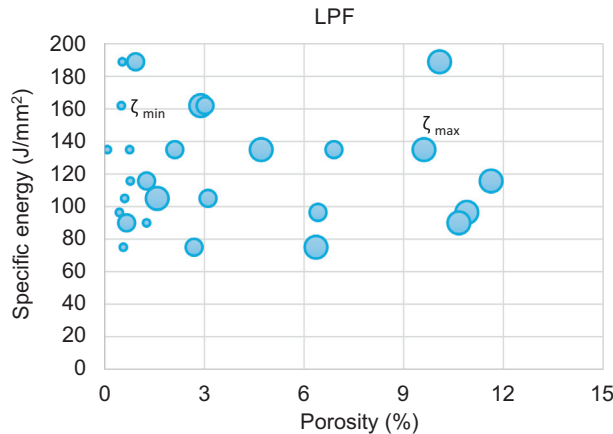


Fig. 21. Specific energy versus porosity in H13 tool steel with relevant normalized powder feed rate for LPF [117].

In general, the microstructure in AM is developed based on the above defined thermal history, where three main grain morphologies are observed in steel processed by AM: (i) columnar, (ii) mixture of columnar and equiaxed, and (iii) equiaxed. In other words, the AM processed steel typically show three different regions; (i) interface region, (ii) columnar grain region and (iii) equiaxed grain region. The predilection of microstructure is governed by a crucial control parameter proposed by Hunt [122], based on related solidification theory; the ratio of temperature gradient G and the solidification velocity V_s , i.e. G/V_s . In an extremely large G/V_s , when V_s tends to zero, the solidification microstructure contains planar grains. In a relatively high value, the predominant solidification microstructure would be columnar dendrites and smaller G/V_s value gives rise to equiaxed grains. In LPB, the heat is mostly transmitted through the formerly deposited layers, and develops the highest temperature gradient in that direction, which eventually influences the formation of directional columnar dendrites.

However, this may not be the case for LPF as the melt pool transverse angle with respect to the substrate (θ_s) can vary from 30 to 70° that can change the solidification rate by a factor of $\cos(\theta_s)$ [32]. If the temperature gradient becomes alike in some directions, grains tend to grow in that directions and become equiaxed. A schematic of solidified melt pool with different zones is shown in Fig. 23a. The melt pool consists of equiaxed grains in Zone I and columnar grains in Zone II, also shown in Fig. 23b. The shape and growth of dendrites are different at different layers based on the heat dissipation, as depicted in Fig. 23b.

During the LPF process, bottom layer is heated for a long time which may cause tempering effect and the accumulated heat can result in dendritic growth. On the other hand, at the top layer because of rapid cooling rate dendrites solidify very quickly and have no time to grow coarsely. Also in the LPB process, the microstructure developed is complex because of continuous re-melting process and the Marangoni effect that causes different heat flow directions in the same melt pool. This phenomenon eventually creates different grain growth orientations [123]. The higher thermal gradient, i.e. 10^6 K/m in the LPB process causes columnar microstructure in most of the materials [124]. Moreover, in LPB, the temperature gradients are interrupted by thermal

conductivity of powder as well as solidified zone [125]. As the heat dissipation through the build direction is higher compared to the other directions, solidification in that direction results in anisotropy in grain morphology and mechanical properties. Also in LPB and LPF, cooling rates tend to be high because the area that laser beam heats up is relatively small. Therefore, small heat affected zones and finer microstructures can be obtained in comparison with conventionally cast samples [122,126]. Yadroitsev et al. [127] explored that the 316 L SS processed with LPB presented higher yield strength compared to the forged materials. This statement is supported by Song et al. [37], where he stated that, the better mechanical property of LPB processed samples was due to the presence of smaller grains and higher dislocation density, associated with rapid solidification.

6.2. Solidification and phase transformation in AM steels

The phase transformation and microstructure development in AM processed steels are completely different compared to the conventional cast steels, which pass through slower cooling rates as well as gradual/equilibrium thermo-mechanical processes after casting to obtain more homogeneous material properties. Austenitic SS, (e.g. 316 L and 304) usually shows a completely austenitic microstructure in AM processed steel. Sun et al. [128] employed a detail microstructural characterization in LPB processed austenitic SS 316 L, where two main phases were identified as primary austenite (fcc γ) and small amount of retained ferrite (bcc δ) without any formation of martensite. However, Tucho et al. [129] identified traces of martensite and/or ferrite phases in austenite matrix in LPB processed 316 SS. Zhang [126] observed complete austenite phases in LPF of SS 316 L, but some ferrite phase was also observed by Yadollahi et al. [130]. Also, in LPB processed austenitic SS 304, similar elongated grains in building direction and complete austenite phase with no carbide precipitates were observed [131]. Similar austenitic phase with columnar structure is reported by Yu et al. [132], in LPB processed 304 SS. In this work, the mechanical anisotropy was compared between LPB processed 304 SS and Ti-6Al-4 V alloy, which is related to microstructure morphology governed by directional solidification. During the fast cooling stage involved in LPB processed SS 316 L, the high-temperature ferrite phase was not transformed to a low-temperature austenite phase. This retained ferrite phase eventually strengthens the austenitic matrix. For similar composition of Cr and Ni in SS up to Cr/Ni ratio of about 1.5, the solidification microstructure mainly contains austenite phases [133].

The microstructure of the conventional martensitic SS fabricated in the AM process is found to form some austenite phases together with martensite, which is stated for 17-4 PH SS, maraging steel (18Ni300), and also for the martensitic SS grade AISI420. 17-4 PH steel fabricated through the LPB process contains a significant amount of retained austenite with body centered cubic (bcc)/martensite and fine niobium carbides (NbC) favorably arranged through dendritic boundaries [106]. According to Cheruvathur et al. [106] during solidification of AM 17-4 steel, from the liquid the first phase is formed as: bcc/ferrite followed by bcc + fcc/austenite. Also, some MC phases enriched with Nb is formed. When solidification is roughly completed, the fcc turns as the major phases, and at the end of solidification, approximately equivalent amounts of bcc and fcc phases and small amount of NbC are detected.

Table 4

Influence of some process parameters on porosity of steels made by LPF.

Material	Resulting porosity	Mass flow rate	Laser power	Specific energy	Thickness	Stability of flow rate	Scan speed	Linear mass density
H13 tool steel [90]	↑							
H13 tool steel [90]	↓	↑						
H13 tool steel [117]	↓		↑					
316 SS [118]	↓				↑			
316 SS [114]	↓					↑		
316 SS [119]	↓						↑	
420 SS [116]	↑							↑

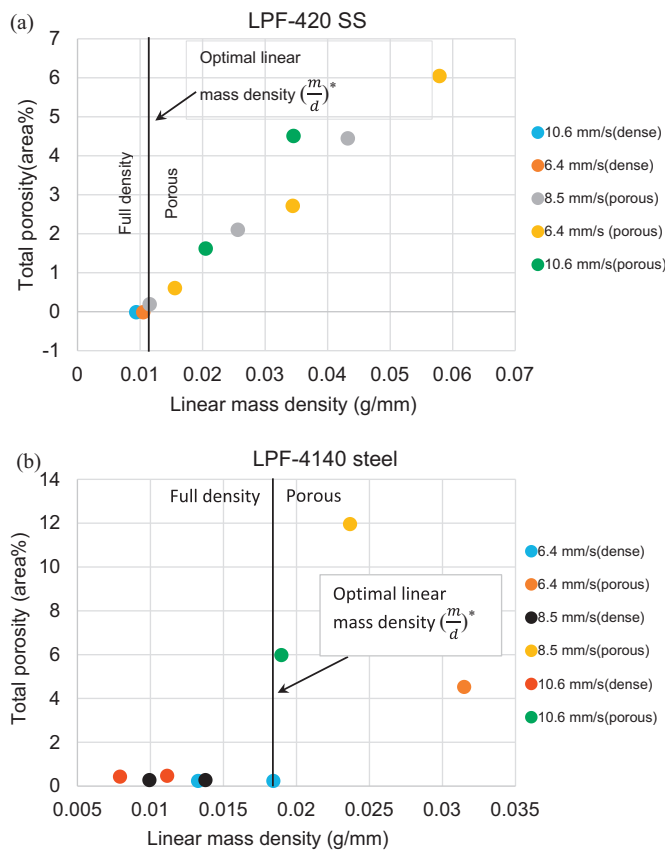


Fig. 22. Variation of total porosity with (a) linear mass density for various laser velocities in 420 SS, and (b) in 4140 steel made by LPF, adopted from [115].

Facchini et al. [134] worked on LPB of 17-4 PH steel and reported a microstructure consisting of austenite and martensite phases, with both twinned and un-twinned regions adjacent to the martensitic grains. The retained austenite is observed among the martensite plates. Kudzal et al. [135] and LeBrun et al. [136] examined the same phenomenological phase structure in 17-4 PH SS. During the cooling stages in LPB, the residual thermal stresses in the material cannot transfer all austenite to martensite, which result in retained austenite [136]. Mainly retained austenite forms at grain boundaries, because of the irregular atomic arrangement, which stops further growth of martensite [137]. Therefore, finer grain sizes enclosing more grain boundaries may influence the occurrence of more retained austenite in LPB of 17-4 PH SS. Al-Mangour et al. [138–140] worked on the LPF processed 17-4 SS, and reported on the microstructural phase transformation during shot-peening (SP) and heat-treatment. From their experiment, the retained austenite of

as-built sample passed through the SP process and possessed martensite phase transformation [139]. Their another study also explored microstructure development at different aging temperatures, where fractions of retained austenite was observed at 866 K but showed fully martensite at lower temperature of 755 K [138].

For both LPB and LPF processes, maraging steel grade 18Ni-300 shows similar tendency to form cellular/dendritic structure and epitaxial growth of the solidified grains [77,141]. This martensitic SS has a considerable amount of retained austenite and upon aging precipitation, together with austenite reversion is occurred [77,141,142]. The austenite reversion is expected during long period of aging, because the metastable martensite converts to stable austenite. During the aging process, Ni is released into the Fe matrix and convoys the conversion from Ni₃ (Mo, Ti) to further steady Fe₂Mo precipitates, which stimulates austenite reversion [143]. Campanelli et al. [144] investigated the microstructural morphology in 18Ni (300) maraging steel clad produced on AISI 304 substrate in the LPF process. The presence of equiaxed and elongated grains also with dendrite morphology were alike to that observed by Casalino et al. [88] in the LPB process of maraging steel. Their work revealed a microstructure with fine martensite phases and a transformation of austenite to Fe-Ni martensite. Austenite reversion is also explored by Krakhmalev et al. [145] in LPB processed AISI 420 martensitic SS. The top layer revealed martensite and retained austenite in contrast to inner layer where tempered martensite was present with higher volume of austenite. The LPB process is a multi-step technique containing repeated thermal cycles (melting-solidifying), which then believed to cause stabilization of austenite by rearrangement of carbon between martensite and austenite. Their selective diffusion result in the austenite reversion and consequent growth of retained austenite. In another investigation of martensitic SS SC420 processed in LPF [146], showed tempered martensite with fine carbides and ferrite along the grain boundary.

Mertens et al. [35] worked on LPB processed H13 tool steel, and reported a significant observation in microstructure development with different powder bed pre-heating temperatures. The microstructure after preheating at 200 °C, is comparable to the microstructure obtained without preheating which constitutes a martensitic phase as well as retained austenite. After preheating at 400 °C, which is above the martensite transformation temperature will produce bainite; an intermediate form between martensite and pearlite. Yan et al. [132] also reported martensitic phases decomposed into α-Fe and Fe₃C with retained austenite in the LPB processed H13 tool steel. During LPF of H13 tool steel, the microstructure morphology is columnar to equiaxed grains and most of the grains contain martensite phases [90,91].

During LPB of a high strength low alloy steel, e.g. HY100 [39], the microstructure in the molten region after solidification is fully austenitic; that completely converts to martensite (untempered) by rapid solidification. It is already reported in many work [147,148] that HY100 steel with lower carbon content and higher Ms. (406 °C) and Mf (221 °C)

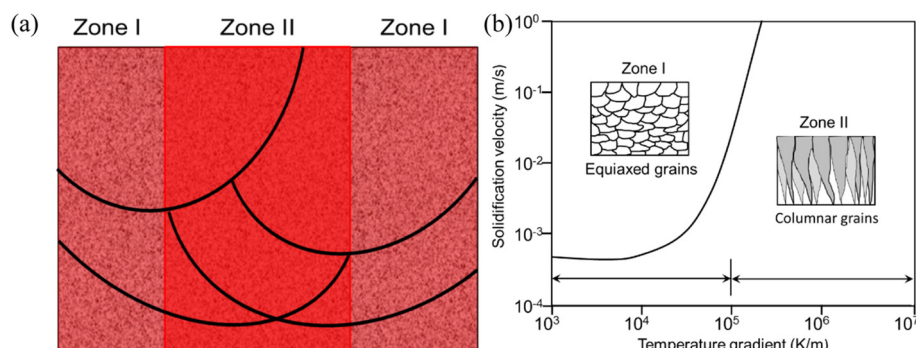


Fig. 23. (a) Schematic of the melting (Zone I) and re-melting zones (Zone II) in the melt pool, (b) the plot shows different temperature gradient regions to form columnar and equiaxed grains, with relation to solidification velocity for 316 SS [126].

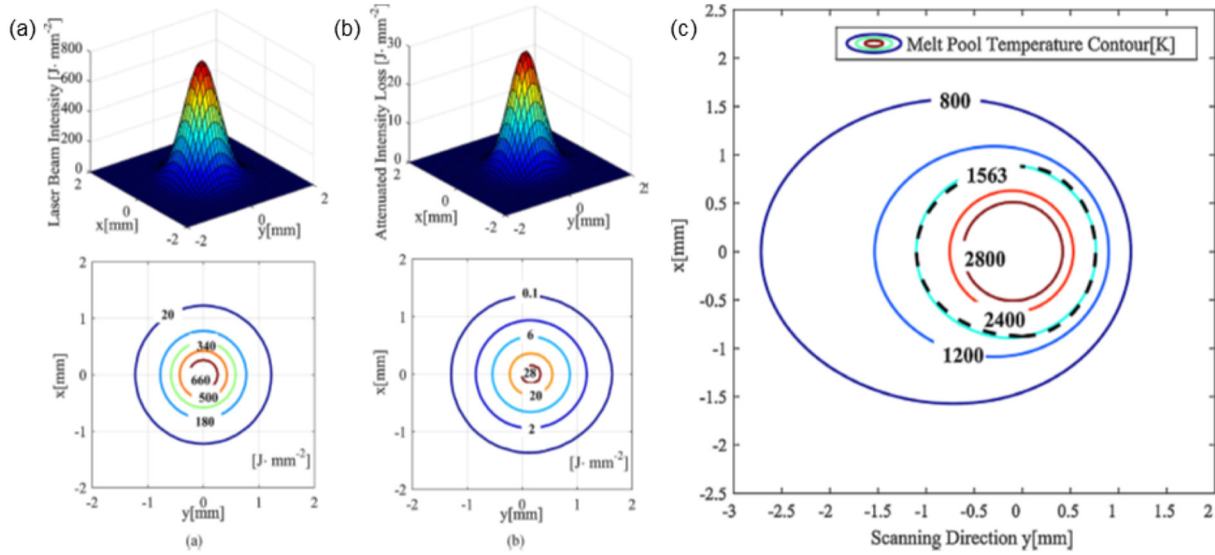


Fig. 24. Laser beam intensity distribution on the substrate surface (a) without attenuation (b) attenuated laser intensity loss by the powder and (c) temperature distribution in the melt pool on the Inconel 625 substrate surface [157] [reproduced with permission from Elsevier].

temperatures produces lath martensite and complete transformation of austenite to martensite. The standard heat treatment at austenizing temperature followed by quenching and tempering form tempered

martensite with variation in lath size. In steel, tempering causes carbon to diffuse out of supersaturated martensite, and reacts with Fe, Cr, and Mo to form carbides in the matrix of martensite.

Table 5

A summary of the input parameters and outputs employed for the modeling of different AM processes where ferrous alloys are used.

Materials/process	Input parameters	Output	Max. percentage difference
SS 303 L/LPF [155]	<ul style="list-style-type: none"> - Laser pulse energy - Laser pulse frequency - Laser pulse width - Laser beam diameter - Thermal conductivity - Specific heat capacity - Melting temperature - Density 	<ul style="list-style-type: none"> - Temperature field, - Melt pool depth and dilution 	In agreement with the experimental results
AISI 4340//LPF [165]	<ul style="list-style-type: none"> - Powder feed rate - Laser power on the substrate - Ambient temperature - Radius of the powder jet - Melting temperature - Radius of the laser beam - Process speed - Absorption factor 	<ul style="list-style-type: none"> - Shape of each deposited layer - Temperature distribution across the part 	In agreement with the experimental results (~23% between the third and fourth layers)
AISI-D2 AISI-316 L/LPF [166]	<ul style="list-style-type: none"> - Mass flow - Particle shape - Size distribution 	Particle flux	<15%
SS 304 L/LPB [167]	<ul style="list-style-type: none"> - Laser power - Hatch spacing - Point distance - Laser exposure time - Effective scan speed - Laser diameter - Optical penetration depth - Reflectance of SS304 L - Number of laser tracks 	<ul style="list-style-type: none"> - Temperature history - Melt pool size prediction - Microstructure formation 	Max error: 4% in width Max error: 30% in depth (Dependent on laser power)
316 SS/LPB [168]	<ul style="list-style-type: none"> - Laser power - Melting point - Latent heat of melting - Specific heat of the solid phase - Specific heat of the liquid phase - Thermal conductivity of dense material - Thermal conductivity of powder 	Local temperature distribution in the laser-powder interaction zone	
316 SS/LPB [169]	<ul style="list-style-type: none"> - Laser power - Scan speed - Energy density 	<ul style="list-style-type: none"> - Melt pool cross section and dimensions 	<ul style="list-style-type: none"> - 8.2% in width - 2.9% in depth

For high carbon steel 4140 in the LPB process [149], the microstructure constituents are obviously finer compared to the wrought 4140 steel and show martensite and bainite dominate phases. Because of the rapid solidification of the melt pools, similar martensitic phases with fine microstructure are observed in 4340 high-strength low alloy steel [53].

7. AM modeling for ferrous alloys

Modeling of AM processes is extremely important for the process parameters optimization and to provide prediction of residual stresses and microstructure evolution in 3D printed parts. Three categories of models can be found in literature: numerical, analytical and empirical. In LPB and LPF processes, melt pool formation [150], laser particle interaction process [151], temperature, velocity and thermal stress field distributions over the process, can be simulated by numerical models [152–154]. Analytical models take into consideration the physics of the processes and the process optimization. In the literature, analytical models have been employed to predict the melt pool depth, dilution and the temperature field with known values of clad height and width [155]. In their work Fathi et al., used a parabolic equation to build the melt pool's top surface and the temperature field was predicted solving the heat conduction in substrate based on an infinite moving point heat source [155]. Tan et al. [156], estimated the clad layer geometry based on a moving disc heat source model. An ellipse was used to fit the melt pool and the powder catchment efficiency was calculated as the ratio of melt pool and the powder stream area. Most of these models have different prediction accuracy, since they have either decoupled the heat and mass flow interactions in the LPF process or did not take into consideration the changes of the laser power absorptivity [157]. Huang et al. have developed an analytical model for LPF that combines the main physical changes of the whole process with the attenuated laser power, the heated powder stream and the semi-infinite substrate taking in consideration their intensity spatial distribution and concentration [157]. The original laser beam intensity distribution on substrate is shown in Fig. 24a, with maximum value of 660 J/mm^2 , while the attenuated laser intensity loss of around 28 J/mm^2 , by the powder is shown in Fig. 24b [157].

The temperature field on substrate surface, shown in Fig. 24c, was obtained coupling the attenuated laser beam and the heated powder stream that is considered the moving heat source. Two half ellipses were used to approximate the melt pool projection geometry on the substrate surface, and are displayed as dashed lines in Fig. 24c.

The modeling and simulation of LPB-AM are mostly based on numerical models, which incorporate multi-physics by means of Lattice Boltzmann method [158] or the Lagrangian-Eulerian method [159] and cover either the hydrodynamic or the thermodynamic aspects.

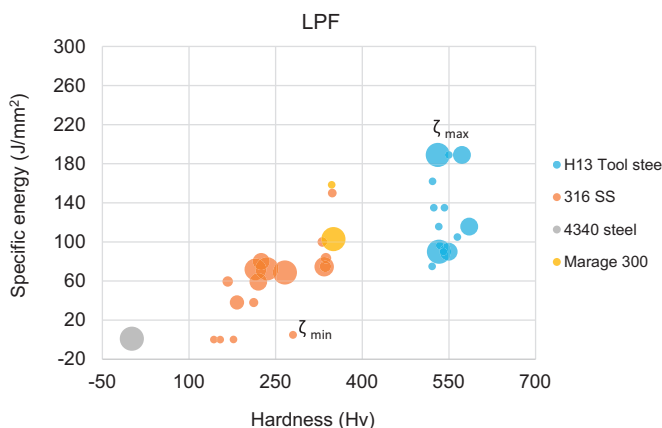


Fig. 25. Specific energy versus hardness of steels shown with equivalent normalized powder feed rate values with, $\xi_{\min} = 218,269.6$ and $\xi_{\max} = 478,114.4$. [176–179].

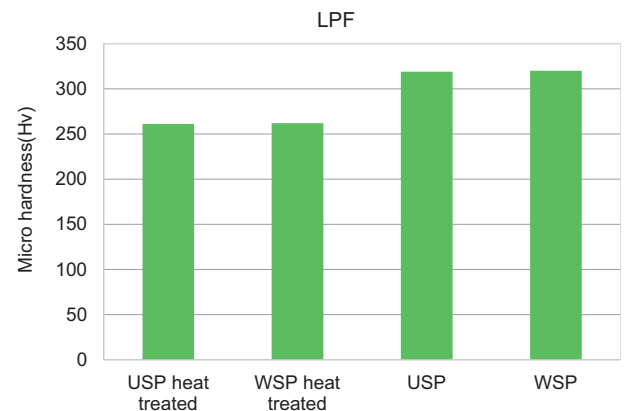


Fig. 26. Hardness distribution of 316 SS at different laser scanning strategies (unidirectional (USP) and weaving scanning path (WSP)) [184].

Empirical modeling are more time-efficient [160] compared to the numerical models, but are case sensitive, while numerical models requires high computation to capture the complex phenomena in the molten pool [157]. Numerical modeling of the LPB process consists of simulations at the micro level (melt-pool modeling) and at the macro level (part-level simulation). At the melt-pool modeling level, multiple physics phenomena should be considered: heat conduction, heat convection and radiation, capillary effects, Marangoni effect, photon absorption by particles [161]. Panwisawas and coworkers [161], taking into consideration most of the interfacial phenomena in their model, they derived the temperature distribution of single-track molten zones. It was demonstrated that the irregularity of the single tracks increased as the laser-scan speed increased. Regarding part level simulations, analytical and numerical modeling has been used to study the residual stresses in the LPB processes [162] and to investigate the temperature and stress distributions in one single layer in LPB [163]. Analytical models, do not incorporate the multi-physics, and are less common due to the more complex physics behind the LPB AM process. For instance, the model proposed by Knol [164] describes the process parameters effect on the residual stresses and the porosity through a semi-analytical thermal model. In their model, the authors build the powder bed temperature field adding the analytical temperature solution together with the numerical boundary correction solution.

Although there are many modeling papers for LPF and LPB, the number of modeling papers in which the target materials are ferrous alloys is limited. A summary of the input parameters and outputs employed for the modeling of different AM process, where ferrous alloys used for model verification and process parameters prediction, is presented in Table 5.

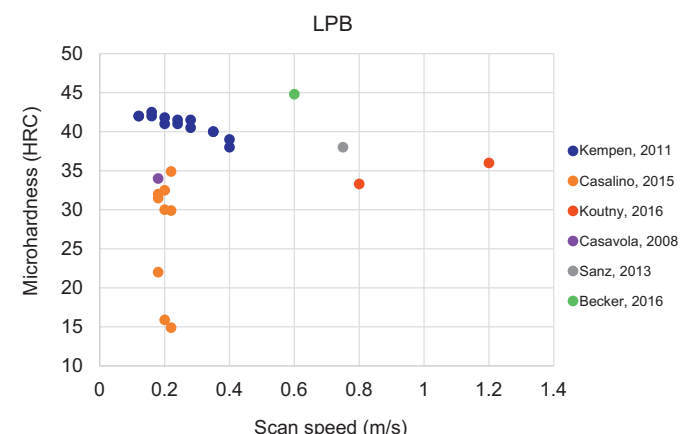


Fig. 27. Influence of scan speeds on microhardness [77,84,85,87,88,189].

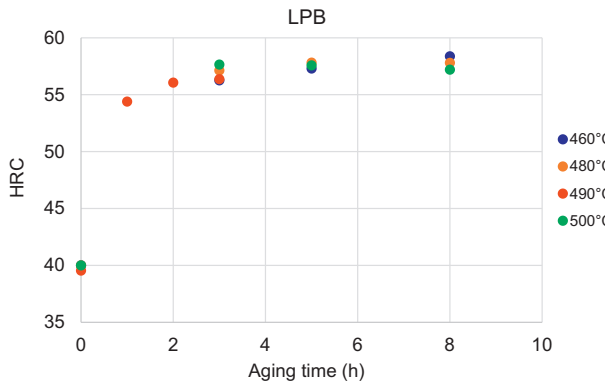


Fig. 28. Influence of different aging parameters on micro-hardness [77,80].

8. Mechanical characteristics

8.1. Hardness

8.1.1. Hardness for LPF processed parts

In the literature, clearly distinguished microstructure zones with micro-hardness have been reported for LPF processed AISI P20 tool steel [170], AISIH13 tool steel [91,171,172], AISI 420 tool steel [173], AISI 4140 steel [174], AISI 410 SS [109] and AISI 316 L SS [118]. It has been stated that for steels, the micro-hardness values of multilayers decreases from the first deposited layer and then increases towards the top layers [118,174,175] due to the heating up of the previous layers and giving them time to be slightly annealed [91]. Furthermore, this inhomogeneity can be ascribed to the time-changing solidification rate in the melt zone and a relatively slower rate in the central area. As a result, higher micro-hardness has generally been recognized at the top and bottom of LPF parts in comparison with the middle region [10].

In Fig. 25 for different kind of steels, the data for specific energy vs. the average micro-hardness is presented, as obtained from the literatures. From the Fig. 25, shown that, H13 tool steel has the highest hardness among the other steels included in these studies, as expected.

Between the low alloy steels; ASTM/SAE 4140, 4130, and 1045 are anticipated to be the hardest steel because of the higher content of alloying elements, as well as higher carbon content in 4140 and 4130 [180]. In another research work on 4140 steel, hardness was measured at different regions of the clad. The hardness value near the substrate surface was an average of 375 HK500, in the middle of the sample was

330 HK500 and the very last layer showed the hardness of 386 HK500. These hardness values were comparable to other works available in the literature, which associated with the formation of bainite and tempered martensitic [181,182]. In other publication, the hardness values of the deposited 18Ni (300) maraging steel was found between 347 and 350 HV [176–179]. These values are in agreement with the usual microhardness of 18Ni (300) steel after solution annealing heat treatment, as referred in the ASM Handbook [144,183].

In H13 tool steel, the internal part hardness somewhat diminished towards the center and bottom of the sample because of re-heating during the process [91]. Similar behavior was observed for 316 SS, where the Vickers microhardness values of clad surface intensified compared to the inside of the clad, as the clad surface experiences the cooling effect of shielding gas. In addition, for H13 tool steel, hardness values were similar to that of wrought material. However, for 316 SS clad, the hardness is much greater than that of conventional cold-rolled material because of the rapid solidification throughout the LPF process [126].

The impact of inter-layer time interval on microhardness values for 316 LSS was obtained according to the longitudinal axis of the samples, where the hardness amounts represent that the single-built set has lower hardness values (185 HV) even in heat treated condition (157 HV) compared to the nine-built specimens (215 HV). According to this research, the inter-layer time interval and post heat treatment can have an effect on the microhardness values of 316 SS [118]. It is worth mentioning that unidirectional and weaving laser scanning path (USP and WSP respectively) do not extremely influence the microhardness of 316 SS, as evident in Fig. 26. The Vickers hardness values of USP and WSP samples do not show any significant differences. However, as-deposited samples have higher hardness values compared to the heat-treated (1050 °C for 1 h) ones, which is in agreement with other researches [184].

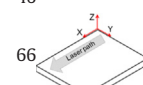
8.1.2. Hardness for LPB processed parts

A broad range of microhardness values for LPB processed 316 SS can be obtained by various scanning speeds and hatch spacing, as recently reported by Sun et al. [128]. The highest value of microhardness reported at an energy volume density of 101.33 J/mm³ was 220 HV [128], while, the annealed SS316 L samples showed a microhardness values between 150 and 160 HV. These microhardness values were lower than the ones reported by Saeidi [185] (320 HV). As reported by Sun [128], this difference might be attributed by the amount of amorphous nano-scale inclusions and the grain size. In particular, smaller

Table 6

Tensile properties of several 316 SS grades processed with LPF and conventional ones.

Ferrous alloys	Process	UTS (MPa)	YS (MPa)	EL (%)
316 SS [15]	Wrought or forged/and annealed bar	586	234	50
	LPF	758	434	46
	LPF-perpendicular building direction (Y)	793	448	
316 SS [193]	LPF-parallel building direction (X)	807	593	30
	Wrought or forged/and annealed bar	578	289	50
316 SS [194]	LPF	661	276	67
	LPF	579	296	41
316 L SS [191]	Wrought or forged/and annealed bar	480	170	40
	LPF	540–560	330–345	35–43
	LPF-parallel building direction (X)	586	241	50
316 SS [126]	Wrought or forged/and annealed bar	639	558	21
	LPF	352	536	46
	Perpendicular building direction (Y)	558	639	21
	Parallel building direction (X)	620–660	405–415	32–40
316SS,single-built(as-built) [130]	LPF	600–620	325–355	42–43
316SS,single-built(heat-treated) [130]	LPF	660–685	465–485	12–20
316SS,nine-built(as-built) [130]	LPF	540–625	330–395	35–85
316 SS [118,190]	LPF			



grain size and larger amount of inclusions lead to higher values of microhardness [128,185].

Another research conducted by Wang et al. [186], showed a correlation between the densification level, which depends on the volume energy density and the grain size. The researchers demonstrated higher hardness values (281.6 HV) at higher densification level, which resulted in more refined microstructures [186]. At increased energy density, a coarsening of the cellular dendrites occurs and leads to a decrease in the microhardness values (267.1 HV) [186]. Similar hardness value of 280 HV, is observed in LPB processed single tracks in 316 L austenitic SS [187].

Recently Rashid and coworkers reported the effect of scan strategy on microhardness of LPB processed 17-4 PH SS [188]. The highest hardness value (458 HV) was measured for the samples fabricated with a double scan strategy compared to the ones with a single scan strategy [193]. This phenomenon was due to the occurrence of lower percentage of retained austenite and a higher percentage of martensite [188]. However, for maraging steel, there is negligible effect of scan strategy on the hardness values, as plotted in Fig. 27, specifically at low scan speeds, and the same trend is reported for layer thickness [77,79,80]. However, at higher scan speeds, a small drop in micro-hardness values is observed.

Aging has a significant effect on the hardness values of LPB processed maraging steel, as shown in Fig. 28, where at 460 °C, the hardness and the aging time follow a linear relationship; micro-hardness continues to increase with time without showing over aging. However, the longer aging time has no significant effect to increase the micro-hardness values. On the other hand, at elevated temperatures and prolonged durations, micro-hardness starts to slightly decrease, which may be because of the austenite reversion and coarsening of the intermetallic precipitates. During laser melting, the surrounding material and the following layers are heated up leading to precipitation reactions, which may be promoted with micro-segregation accompanied with cellular growth. In LPB, the re-melting process is significantly pronounced to increase the micro-hardness of the parts, since a second round of aging takes place [77,80]. On the other hand, age hardening of LPB produced maraging steel causes an increase in the hardness up to 58 HRC, when optimal aging time and temperature (5 h and 480 °C) is selected.

8.2. Tensile properties

8.2.1. Tensile properties of LPF processed parts

Table 6 lists the ultimate tensile strength (UTS), yield strength (YS), and the elongation at failure (EL) for different grade steels processed by LPF along with reference properties of wrought steels, [15,118,190–192]. The UTS and YS of LPF parts are mostly greater than those synthesized from wrought counterparts, which can be ascribed to the higher cooling rate and grain refinements [15,190,192]. However, LPF processed steels show lower elongation-to-failure values, which is believed to be due to porosity and inclusions inside the products caused by the poor optimized process conditions.

Fig. 29a–c shows the specific energy vs. UTS, YS and EL values for various kinds of SS (316SS vs. 420SS) obtained from the literature. For comparison, different values of normalized powder feed rate (ζ) are also indicated.

Another interesting feature regarding the tensile properties of LPF steels is the building orientation of the parts, which affects the resultant tensile properties of the component. A summary of building orientation effects, e.g. parallel (X-direction) vs. perpendicular (Y-direction), on tensile properties of steels is listed in Table 6. It is believed that this anisotropic behavior is due to the occurrence of weak interfacial layers, both in Z- and Y-directions, which provides a simple path for shear bands [10,15]. Various cooling rates in these deposition directions might affect microstructure and mechanical properties.

The laser passing time between each subsequent layer is greater for X-direction compared to the materials built in the Y- or Z-directions.

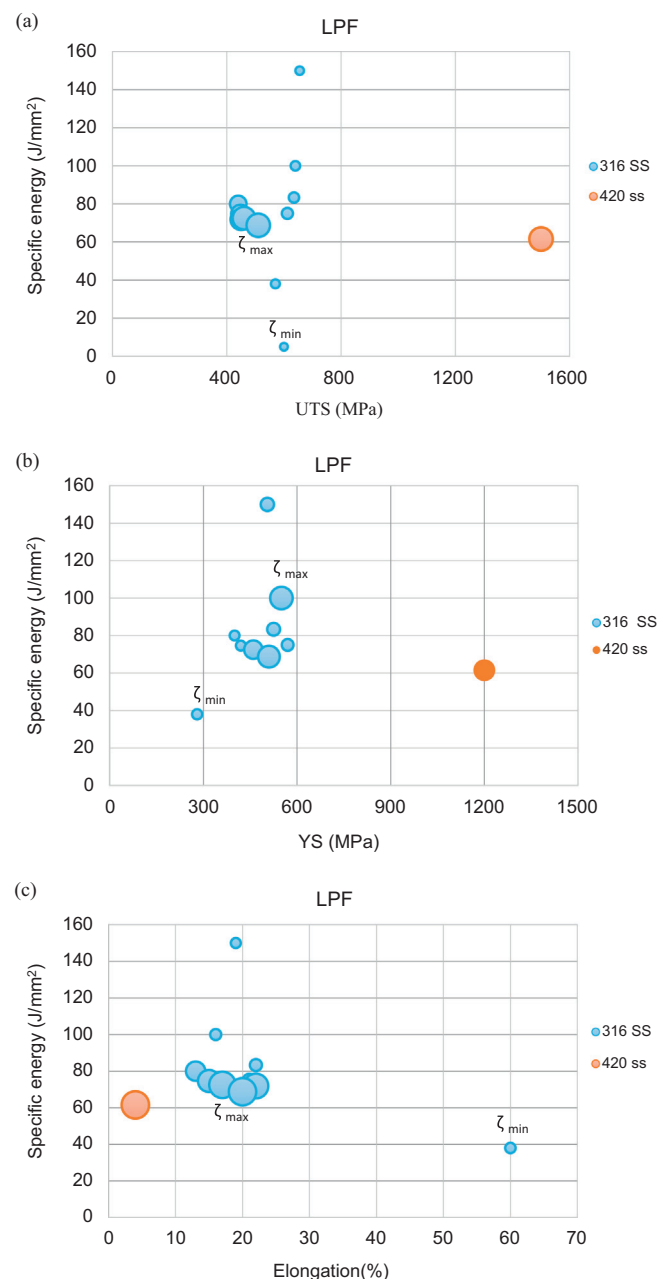


Fig. 29. Specific energy vs. (a) UTS, (b) YS and, (c) EL for different kinds of steels with relevant normalized powder feed rate (ζ) [89,108,118,126,146,195–198].

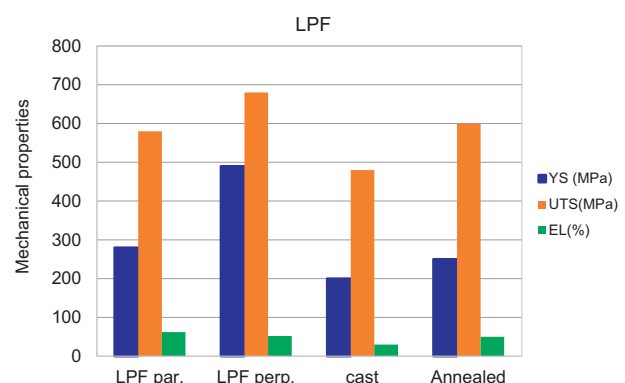


Fig. 30. Unusual behavior of YS, UTS and EL for LPF of 316 SS [110].

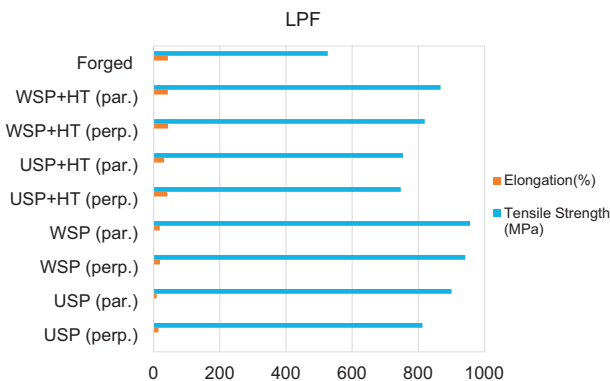


Fig. 31. Tensile properties of 316 SS, as-built, heat-treated and forged specimens with different scanning paths (unidirectional and weaving) in LPF [184].

Accordingly, higher cooling rates, and consequently, finer microstructures for specimens deposited in the X-direction can be obtained [199].

However, some authors describe different behavior for 316 SS in terms of anisotropy, as illustrated in Fig. 30, where the tensile properties for LPF steels in X and Y directions, as well as the results for cast and annealed steels are presented. The mechanical properties of LPF materials are superior to the cast and annealed wrought ones. Interestingly, specimens constructed perpendicular to build direction possess higher tensile strength and poorer elongation than the specimens build along the parallel direction. However, this is in contrast with other studies. According to the authors, this behavior was the result of the distinct positioning of grains along the tensile loading direction, together with the grain size and spacing between inclusions [108].

In addition to building orientation, there are other two factors affecting the tensile properties of LPF parts; (i) inter-layer time interval and (ii) the scanning path. The measured tensile properties for single-built, nine built 316 SS and their corresponding cast and wrought materials are listed in Table 6. It is stated that the YS and UTS of 316 L SS by LPF is higher than their cast/wrought alloys, whether or not heat treatment or process time interval are taken into consideration. In addition, yield and tensile strengths of the specimens have been increased by higher layer-to-layer time interval. However, heat treatment can

decrease yield/tensile strength. Nine-built specimens show significantly poor elongation to failure in comparison with the cast and wrought materials probably due to the reasons such as: flaws within the parts, finer microstructures and unsteady metallurgical bond between the layers, when the elongation to failures of one-built specimens is similar to the heat treated ones [130].

The impact of scanning path on tensile properties of 316 SS is of interest. Fig. 31 represents the tensile data in both as prepared and heat-treated condition for 316 SS; built by following unidirectional (USP) and weaving scanning path (WSP). From the plot, it is evident that the USP and WSP as-built specimens have higher tensile strength than the forged parts. However, elongations are significantly lower in comparison with forged counterparts. The reasons for this behaviour could be the presence of finer grains resulted from the rapid solidification of the material in the LPF process. In addition, inevitable internal stress, oxidation and porosity might be other disadvantages for ductility. As displayed in Fig. 31, the tensile properties are anisotropic for the USP. The parallel loading direction to the scanning path shows greater tensile strength compared to the perpendicular one, whereas the elongation is the opposite. Therefore, it seems that the samples deposited by WSP have higher performance than the USP and the conventional forging ones [184].

8.2.2. Tensile properties of LPB processed parts

In Table 7, the tensile properties are listed for different steel grades fabricated by LPB techniques along with the properties of the wrought materials [125]. Ahmadi and coworkers reported about the variation of the mechanical properties with laser input power, scanning speed and scanning strategy in 316 SS fabricated by LPB [200]. In particular the authors demonstrated that strain and toughness of the samples are remarkably affected by the laser power. The reason is that as the laser power increases, greater energy density and complete melting are reached due to the greater particle fusion. Moreover, the high energy density reduces the porosity and leads to bigger melt pools, and eventually the manufactured products density will be increased. The tensile strength, as well as other mechanical properties are influenced by porosity [200]. The authors also studied the variation of the mechanical properties with the scanning direction.

Table 7
Tensile properties of various steels, fabricated by LPB

Ferrous alloy	Process	UTS (MPa)	YS (MPa)	EL (%)
Iron (electrolytic, annealed) [201]	Wrought	240–280	70–140	40–60
Iron (0.004%) [202]	LPB	450	380	20
Iron (0.02%) [37]	LPB	350–410	240–300	10
AISI 1005 [203]	LPB	305	164	–
AISI 1033 [34]	LPB	–	650 ^a	–
AISI 1050 [34]	LPB	–	800 ^a	–
AISI 1075 [34]	LPB	–	1150 ^a	–
4130 – as built [149]	LPB	1503 ± 69	1344 ± 67	12 ± 2
17-4 PH SS ASTM A564 [125]	Wrought (ST + PA)	1310	1170	10
17-4 PH SS [136]	LPB	1255 ± 3	661 ± 24	16.2 ± 2.5
304 SS [204]	LPB (orthogonal to building direction)	715.5 ± 1.5	568 ± 2	41.7 ± 1.1
304 [205]	LPF longitudinal	710	448	59
	LPF transverse	324	655	70
18Ni-300 M [77]	Wrought	1000–1170	760–895	6–15
18Ni-300 M [77]	LPB	1290 ± 114	1214 ± 99	13.3 ± 1.9
18Ni-300 M [142]	LPB	1165 ± 7	915 ± 7	12.44 ± 0.14
4340 [53] 593 °C stress-relieved	LPB	1289–1310	1365	16–17
HY100 [39] as per MIL-S-16216	Wrought	Not specified	690–827	>18%
HY100 – as built (xy) [39]	LPB	1200 ± 15	1160 ± 15	6 ± 2
HY100 [39] direct temper 650 °C-2 h-AC (xy)	LPB	880 ± 10	710 ± 30	8 ± 3
HY100 [39] 900 °C-1 h-WQ + 650 °C-2 h-AC	LPB	780 ± 10	690 ± 10	18 ± 2
H13 [206]	LPB	1000–1200	–	0.9–1.9
H13 [207]	LPB	1370 ± 175.1	1003.0 ± 8.5	1.7 ± 0.6
M2 – heat treated [36]	Wrought	1611	–	1.3
M2 [36]	LPB	1286	–	0.6

^a Compressive, ST: solution treated, PA: peak aged.

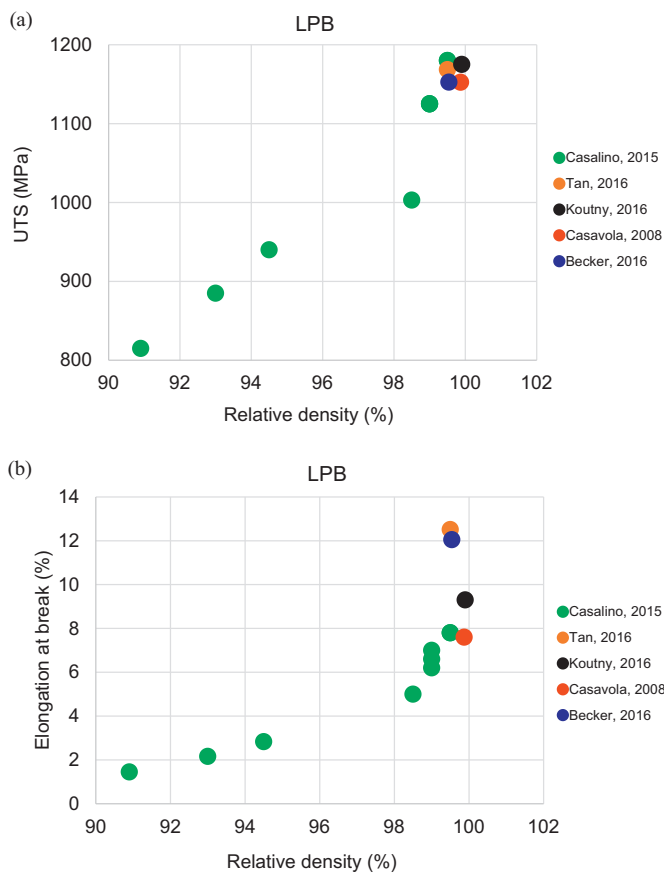


Fig. 32. Correlation between ultimate tensile strength (a) and elongation at break (b) and relative density [83–85,87,88].

In particular, it was demonstrated that the parts fabricated by cross-hatching with zig-zag scanning showed improved mechanical properties compared to the parts obtained by the unidirectional scanning [200]. The enhancement of the tensile strength and toughness is due to the reduction of porosity induced by the cross-hatching method.

Wang et al. [186] also showed that the tensile strength and elongation values of LPB manufactured 316 SS are influenced by the laser energy density ($\frac{P}{v s l}$, where P is laser power, v is process speed, s is hatching space and l is layer thickness). From their work, higher tensile strength is found in LPB processed 316 SS, compared to the wrought one. The strength properties vary with the processing method, processing parameters and the post-process heating, which affect the microstructure [125]. Nakamoto and coworkers [34], showed that steels with higher carbon content showed increased values of yield stress. Moreover, for fully dense SLS samples at a given carbon content, the yield stress is higher for those ones fabricated at a lower energy input.

The tensile property of maraging steels fabricated by the LPB process, correlates positively with relative density, as displayed in Fig. 32 (a,b). LPB processed parts show higher strength and hardness values compared to conventionally aged products, because of the melting and re-melting process. In addition, aging heat treatment leads to an

increase in ultimate tensile strength and Young's modulus through the precipitation of intermetallics. However, the elongation is significantly reduced by age hardening [77,79,83]. As relative density of the LPB processed parts increases, fracture behavior shifts from brittle to ductile. Ductile fracture results from the growth and joining of micro-cavities, while brittle fracture behavior is the result of macro-cavities, which generated throughout the sintering process without sufficient energy density.

8.2.3. Tensile properties of BJ printed parts

Binder jetted cellular lattice structures are less stiff with a smaller elastic modulus compared to the LPB/LPF processed lattice structures, which is due to the formation of a weak neck connection among the powder particles in BJ manufacturing process and partially sintered metal powders [21,22]. Consequently, these lattice structures are only suitable for tissue engineering scaffolds that necessitate micropores for nutrient diffusion [21]. Zhou et al. [22] introduced Instrumented Indentation Testing (IIT) to measure the Young's modulus of lattice structural parts made by BJ, and depicted a value of 1.50 and 0.446 GPa for grid lattice sizes of 1.5 and 1 mm, respectively, which are far from 200 GPa for a conventionally processed SS.

8.3. Fatigue property

8.3.1. Background

Fatigue is one of the critical failure modes for the effective design of many engineering materials. Cyclic loading normally initiates cracks by accumulating the plastic damage and subsequent propagation of the cracks [208]. Generally, cracks tend to initiate near the surface, where nominal stresses are often higher (e.g., in bending), and where geometric variations at surfaces (such as machining marks, surface flaws, notches, etc.) cause stress concentration. Also, material defects (such as inclusions, second-phase particles, voids, micro-cracks etc.) can produce stress concentrations to promote crack formation and failure. Thus, fatigue plays a significant role in the engineering design.

8.3.2. Fatigue strength in LPB processed steel

From the literature, it is already known that high cycle fatigue (HCF) properties of LPB steels are very sensitive to process-induced porosities which influence premature failure through the crack initiation mechanisms. Fatigue test parameters for some LPB processed steels are summarized in Table 8.

Zhang et al. [209] studied the fatigue properties of LPB processed 316 L SS and explored that within a $\pm 30\%$ tolerance limit, porosity does not invade the HCF properties. Within the optimum processing level, porosity driven cracking may be influenced by solidification defects caused by over-melting and under-melting and degrade fatigue resistance. In their experiment, laser powers were varied from 50%, 70%, 100%, 130% and 150%, samples were denoted as 0.5P, 0.7P, P, 1.3P and 1.5P respectively, as shown in Fig. 33.

A longer fatigue life is observed in 0.7P sample because of the internal grain growth morphology. Usually grains with less favorable orientation relative to the temperature gradient stop growing at melt pool boundary. The finer grain sizes with increased grain boundaries act as obstacles to dislocation motion and promote intergranular crack

Table 8
Heat treatment (HT) detail of LPB processed steels and their fatigue test parameters.

Substrate	Fabrication method	Clad-microstructure	Post-HT	Microstructure after post-HT	Fatigue test parameter
316 SS [209]	LPB	Austenite	–	–	R = 0.1, F = 5 Hz
17-4 PH SS [137]	LPB	Martensite + retained austenite	Solution annealing 1040 °C/30 m + AC + precipitation hardening 482 °C/1 h + AC	Precipitation of chromium nickel copper	R = -1, strain controlled
AISI18Ni300 [210]	LPB	Martensite	–	–	R = 0, F = 15–50 Hz

initiation and crack branching, which could result in higher ductility and longer fatigue life.

Yadollahi et al. [137] studied the strain-controlled fatigue behavior of LPB processed 17-4 PH SS, where four types of samples were considered; (i) as built horizontal, (ii) as built vertical, (iii) horizontal + heat treatment, and (iv) vertical + heat treatment. The strain amplitudes vs. fatigue lives of different LPB 17-4 PH SS is shown in Fig. 34. For LPB processed 17-4 PH SS, solution annealing and peak-aging heat treatment is favorable for low cycle fatigue (LCF), and unfavorable for HCF. This is because the associated impurities from the LPB process make 17-4 PH SS more sensitive and after heat treatment it became harder. However, as the defect sensitivity in LCF process was less obvious, after heat treatment specimens showed better fatigue property. Also the building direction showed significant impact on fatigue properties in LPB processed parts. In horizontally built sample, higher fatigue strength was mainly ascribed by their orientation along the loading axis. In case of vertical specimen, defects were more harmful as they generated stress concentration during loading.

The effect of scan speed, porosity and microstructure on fatigue properties of LPB processed maraging steel AISI 18Ni300 was investigated by Santos et al. [210]. The result shown in Fig. 35 indicated that for short lives, fatigue strength in both load control and displacement control is similar. However, for longer life, load control tests show higher fatigue strength.

8.3.3. Fatigue strength in LPF processed steel

Very few research works have been done on the fatigue properties of LPF processed steel, among them 300 M steel [211], AISI4340 steel [212,213] AerMet100 [214] steel are reported. The experimental detail of pre and post heat treatment of various laser cladded steels and their fatigue test parameters are listed in Table 9. The fatigue behaviour of the laser cladded material is not simple because of the formation of complex microstructures with different zones (cladding zone, interfacial zone, and heat affected zone) compared to the conventional microstructure in steel after heat treatment.

Chew et al. [212] characterized the axial fatigue failure of AISI4340 steel where three types of specimens were designed in: Type1: as-clad, Type2: groove-clad-grind, Type3: extended clad-surface grind. The fatigue behavior of the substrate together with the above mentioned cladded samples, is shown in Fig. 36. In general, laser cladding reduced the fatigue life, e.g. Type1 specimen has poor fatigue strength compared to Type2 and Type3. In Type1 specimen, the as-clad region acts as localized stress raiser to initiate crack propagation and failure. The surface grounded clad toe region in Type2 specimen also enables to initiate surface cracks with lower propagation rate because of lesser stress concentration, which results in longer fatigue life. Design of Type3 specimen reduced the cross-sectional area which improved fatigue behavior though it pass through the surface grinding of the extended clad.

AISI4340 steel was used as a substrate, where AISI4340 and AerMet100 clads were produced using laser cladding, and a poor fatigue life was reported in AISI4340 as-clad compared to AerMet100 clad [213]. Fig. 37 shows a comparison of fatigue life between AISI4340 as-clad and AerMet100 clad. The reasons for this degradation are summarized as: (1) the clad and HAZ region show high hardness and brittle properties, (2) generation of tensile residual stresses and (3) microstructural inhomogeneity, i.e. columnar grains in the clad area and grain growth in HAZ stimulating inter-granular fracture.

During laser cladding process, the conversion of ferrite from austenite is inhibited because of rapid solidification. As a result, a brittle phase martensite is formed from austenite. Bhattacharya et al. [215] stated a detailed microstructure development during DMD of AISI4340 steel powder. In their work, tempered lath martensite was formed in AISI4340 steel clad.

During laser processing of steel, heating produced by the successive overlapping tracks will not allow austenite in the earlier track to cool

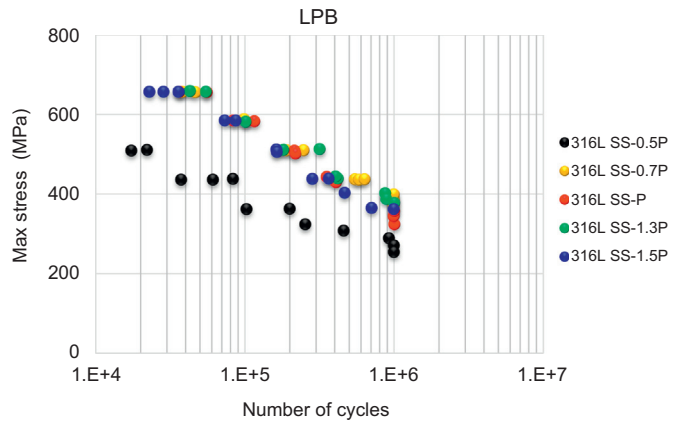


Fig. 33. S-N curves of LPB processed 316 L steel made with different laser powers in LPB, adopted from [209].

below Ms. temperature to form martensite. At the end of the cladding process, the substrate will solidify which results in the conversion of austenite to martensite. This brittle and untempered martensite degraded fatigue life and showed brittle failure mode in AISI4340 as clad steel [212,213].

On the other hand, AerMet100 showed increased fatigue life compared to AISI4340. This is because of the following reasons; (1) lower carbon content of the AerMet100 (0.25 wt%), compared to AISI4340 (0.4 wt%), resulting lower hardness in the clad region, and (2) high nickel content produced Fe-Ni lath-martensite which stimulate ductility. After post clad heat treatment (PCHT), the fatigue life is improved for both clad materials, which is because of the recovery of ductility and toughness in that region.

9. Metal matrix composites (MMC) in AM

Metal matrix composites (MMCs) are manufactured with metals or alloys, reinforced with particulates or fibers of other materials with the objective of high specific strength and stiffness, higher operating temperature/thermal stability, better wear resistance, improved fatigue strength and the capability to possess these properties for a particular applications [216–219]. The reinforcement of metal matrix using AM technology, opens up the possibility of their application in areas where light weight material and cost reduction has the priority, like in automotive, aerospace, and biomedical industries [216–218].

Generally, MMCs are manufactured using conventional techniques, i.e., casting and powder metallurgy, where some major problems are associated as follows: (1) In casting method, the required molds and the

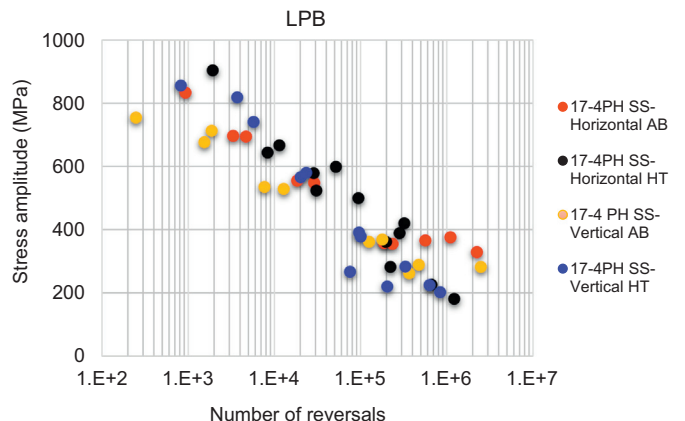


Fig. 34. S-N curves of LPB processed 17-4 PH SS at different sample orientation and heat treatment, adopted from [137].

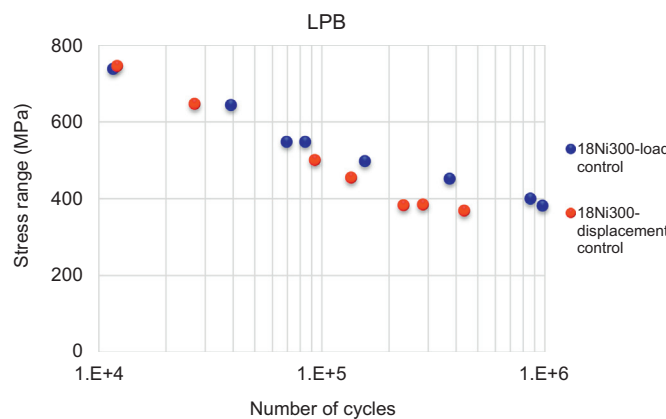


Fig. 35. S-N curves of LPB processed 18Ni300 steel in both load control and displacement control condition, adopted from [210].

post process machining make the technique expensive [216], (2) The low working temperature results weak interfacial bonding between reinforced particle and the matrix which may deteriorate the mechanical property of the composite [220], (3) Microstructural inhomogeneity is another problem due to the non-uniform distribution of reinforcing element throughout the matrix because of Van der Waals attraction forces between surrounding particles [221]. Compared to the conventional casting, in LPB and LPF AM, melt pool pass through a non-equilibrium solidification due to fast heating and cooling over a small melt pool area, which lead to finer microstructure and homogeneous distribution of reinforcing element [5,222]. Moreover, AM can reduce processing times and cost by fabricating near net shape with minimum machining and allow to manufacture products with complex geometry.

In MMC of ferrous alloys, the common reinforcing element includes phases of carbides (SiC, TiC, WC), nitrides (TaN, TiN), borides (TiB, TiB₂, WB), metal oxides (Al₂O₃), and carbon fibers [139], [217,223,224]. Addition of second-phase carbides into steel matrix can improve mechanical properties because of their slow growth rate and thermal stability compared to the cementite [217,225]. For example, reinforcement of thermodynamically stable TiC in martensitic steel matrix, has proven improved stiffness, hardness and wear property [217]. In laser based AM, the strong Marangoni convection brought by high thermal capillary forces caused instability in the melt pool. The liquid flow is generally obsessed by gravity force, buoyancy force and surface tension in the molten area. Consequently, the redisposition of reinforcing elements and their subsequent distributions are significantly influenced by the fluid flow.

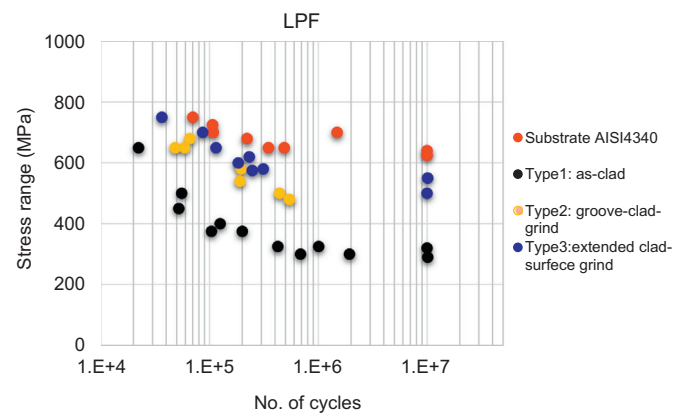


Fig. 36. A comparison between the fatigue behaviors of AISI4340 steel and the clad produced as Type1 (as-clad), Type2 (groove-clad-grind) and Type3 (extended clad-surface grind), adopted from [212].

9.1. LPB processed MMC

In literature, MMC manufactured using LPB process is limited to two steel matrix materials (316 L SS, H13 tool steel) and three reinforced materials or fillers: (titanium carbide (TiC), titanium diboride (TiB₂) and hydroxyapatite (HA)), as summarized in Table 10. The as printed relative density > 95% is achieved with TiC and TiB₂ but is not reported for HA [216,222,223,225–228]. Hot Isostatic Pressing (HIP) treatments allowed a relative density in the range of 99% + for TiB₂, however this decreased the wear resistance and hardness when compared to the as printed condition [225,226].

While filler is seen throughout the matrix, it is typically more concentrated at solidification cell boundaries forming a continuous network of high filler content regions with a honeycomb like appearance [216–218,221,223,225–230]. The presence of well dispersed high melting particulate fillers serves as a nucleating agent resulting in grain refinement. As expected from composites theory, well dispersed nanofillers produce the strongest effects (e.g. 316 L-15TiC [216,221,227]). Due to the increased nucleation, MMC matrix grains are also more equiaxed and exhibit weaker crystallographic texture when compared to unfilled material [217,222,227]. Unlike typical LPB builds, columnar grains in MMC do not extend though the layer due to increased nucleation [222,223].

In LPB produced MMC, the hardness and wear resistance follow the expected trends for particulate reinforced composites, namely they are proportional to filler volume fraction and inversely proportional to filler size. Despite the lower relative densities of MMC, their properties were consistently better than unfilled controls. The most successful filler

Table 9
Heat treatment detail of LPF processed steels and their fatigue test parameters.

Substrate	Pre-HT	Microstructure after Pre-HT	Fabrication method	Clad-microstructure	Post-HT	Microstructure after post-HT	Fatigue test parameter
AISI4340steel [212]	OQ 860 °C + TP 610 °C/160 m	Tempered martensite, coarse carbides	Laser cladding-6 kWIPG fiber laser	Martensite	–	–	R = 0, F = 15 Hz
Alloy steel 300 M [211]			LSF-IIIB laser solid forming	Martensite, bainite	925 °C/1 h + AC + 870 °C/1 h + OQ + 300 °C/2 h + AC	Martensite, bainite, retained austenite	R = 0.1,0.3,0.5
AerMet100 [214]	885 °C/1 h + cold treatment-73 °C/1 h + TP482°C/5 h	Ferrite and martensite	Laser cladding-TRUMPF TruLaser Cell 7020	Austenite and lath martensite	TP 482 °C/5 h	Ni-Fe lath martensite, M2C carbides (M = Cr,Mo,Fe)	R = 0.1, 0.7, F = 5 Hz
AISI 4340, cladding with AerMet100 and AISI4340 [213]	850 °C/1 h + OQ + TP 220 °C/4 h	Tempered martensite	2.5 kW ND:YAG laser	4340 clad microstructure is austenite	Annealing 830 °C/1 h + slow cooling, hardening 850 °C/1 h + OQ + TP 220 °C/4 h.	4340-fine tempered lath martensite, AerMet100-coarse microstructure	R = 0.1, F = 10 Hz

Heat treatment-HT, OQ-Oil Quenching, AC-Air Cooling, TP-tempering, Frequency = F.

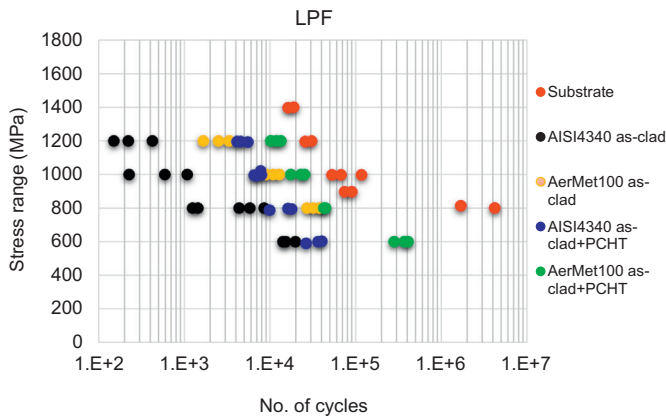


Fig. 37. Constant amplitude axial S-N fatigue curve using $R = 0.1$ and frequency of 10 Hz, adopted from [213].

appears to be TiB_2 , while the most successful preparation strategy appears to be in-situ filler formation during ball milling. The advantages of in-situ formation over the incorporation of an existing filler are the decreased filler size, clear and coherent filler/matrix interface [218] and the avoidance of an independent nano-particle production step. The primary disadvantage is the long-required reaction time (8–36 h) [218,228].

9.2. LPF processed MMC

In LPF, majority of researches have been considered TiC as the reinforcing material because of their high strength and better wear resistance properties, as summarized in Table 11. The amount of reinforced TiC has a significant effect on the size and morphology of the TiC in MMC. Also, various forms of TiC including, spherical, rod, flower-petal, cubic and dendrite shapes can be formed depending on the laser process parameters [231–234]. It is worth mentioning that TiC particles could be undissolved, partially dissolved and completely dissolved in the steel matrix relying on laser cladding parameters such as, laser power, powder feeding rate, and laser cladding speed. It is found that in most of the researches on Fe-TiC MMC, defects free coatings can be produced if TiC is completely dissolved in the steel matrix [234–236]. Also, in other

MMC, containing TiB_2 , SiC, VC, Cr_3C_2 , Al_2O_3 and ZrC as the reinforcing materials, defect free and favorable metallurgical bond between the clad and the substrate has been observed [237–240].

The microstructure of the composite coating is generally planar, cellular, dendritic or fine equiaxed grains [247,251]. So, laser process parameters show a critical role in the quality and microstructure of the composite clad and the interfacial strength between TiC reinforcing particle and the matrix [233,243]. Consequently, they can influence the wear resistance and hardness of the clad layer [232,242].

9.3. BJ printed MMC

The process detail of MMC manufactured in BJ technique and their properties are summarized in Table 12.

Kuldeep Agarwal's group at the Minnesota State University adopted BJ AM process to produce porous biocomposites based on SS and tricalcium phosphate (TCP) with tailored microstructure and mechanical properties to act as load bearing medical implants [254,255]. In their experiment, 316 SS and β -TCP were simply mixed in different volume fractions. After printing and sintering, β -TCP formed a coating on SS particles, with higher volume fraction of β -TCP covered more SS particles [254]. 316SS-20TCP and 316SS-40TCP composites represented an elastic modulus of 7–30 GPa, within the range of cortical and cancellous bones. Where, 316SS-40TCP was suited for scaffold applications and 316SS-20TCP composite found to be an excellent candidate for implant applications [254,255].

Scheithauer et al. [253] reported a thermoplastic 3D printing approach to produce metal-ceramic composites using high-filled iron chromium alloy/17-4 PH suspension and zirconia suspension in molten thermoplastic binder systems/dispersing agent with powder content of 50 vol% steel and 50 vol% zirconia. The process involved preparing suspensions in a heatable ball mill and printing of the suspensions in a layer-by-layer process, which then solidified and passed through the conventional de-binding and sintering [252,253]. Unwanted secondary phases such as oxides and carbides were formed and precipitated within the grain boundaries and the grown pore spaces, which could be avoided during heat treatment in inert atmosphere (Ar/H_2) [252]. This process can be adopted for any materials compositions, considering similar thermal expansion or shrinkage behavior of the materials, which leads to the formation of defectless parts with no delamination, structural changes, etc. [253].

Table 10
Properties of LPB processed MMCs.

Composite Matrix-Vol%	Mixing/heat treatment	Filler size	Hardness	Wear mm^3/Nm	YS (MPa)	Modulus (GPa)
316 L-15TiC	BM AP	45 μm [221]	–	–	710	–
		2–12 μm [227]	335–373 HV	–	987–1150	–
		1 μm [216]	385 HV	6.5×10^{-4}	–	–
		50 nm	406 HV [216]	6.1×10^{-4}	814 [221,222]	–
316 L-10TiC	IS AP	20 nm [218]	342–386 HV [228]	$1.4\text{--}2.3 \times 10^{-4}$ [218,228]	–	–
			318–415 HV [218]	–	–	–
316 L-10TiC [216]	BM AP	1 μm	339 HV	7.3×10^{-4}	–	–
		50 nm	364 HV	4.3×10^{-4}	–	–
316 L-2.5TiC [216]	BM AP	1 μm	293 HV	9.6×10^{-4}	–	–
		50 nm	295 HV	9.4×10^{-4}	–	–
316 L-15TiB ₂ [226]	PB AP	2–12 μm	568 HV	0.006×10^{-4}	–	–
		2–12 μm	617 HV	0.001×10^{-4}	–	–
		BM HIP	2–12 μm	1.0×10^{-4}	–	–
		BM 2xHIP	2–12 μm	1.6×10^{-4}	–	–
316 L-2.5TiB ₂ [226]	BM AP	2–12 μm	303 HV	–	–	–
316 L-15HA [229]	BM AP	<100 nm	2.52 NI	–	85	151
316 L-10HA [229]	BM AP	<100 nm	2.51 NI	–	162	167
316 L-5HA	BM AP	<100 nm [229]	2.36 NI	–	443	226
H13-15TiC	BM AP	5 μm [230]	241 HV	–	50–80	–
		50 nm	306–858 HV [225], 811 HV [9]	3.6×10^{-6} [9]	–	256 [9]
		BM HIP [225]	50 nm	345 HV	–	–
H13-15 TB ₂ [223]	BM AP	2–12 μm	759 HV	1.24	–	–
		2–12 μm	833 HV	1.95	–	–

BM-Ball-Mill, IN-in-situ, PB-powder blend; AP-As Printed, HIP- Hot Isostatic Press; HV-Vikers, NI-Nano Indentation (GPa).

Table 11

Properties of LPF processed MMCs.

Composite Matrix-Vol% filler/substrate	Filler (cemented) particle size (μm)	Hardness	Weight loss by wear (mg)
Tool steel 90MnCrV8-TiC [232]	3	950 HV2	8
Heat treated samples:	–	890 HV2	17
As-quenched			
TP 180 °C	–	790 HV2	38
TP 300 °C	–	1060 HV2	–
OQ1000 °C + twofold refrigerating –196 °C			
OQ 1000 °C + twofold refrigerating –196 °C	50–100	600–860 HV	–
16NCD13(14NiCrMo13-4); low-carbon low alloy	–80 + 40	550 HV0.1	–
Steel-TiC/cast iron [234,241,242]		At 2.5 vol% TiC	
Pure Fe-30 wt% TiC [243,244]	40	1000–1400 HVN	–
Fe-TiC/1045 steel [236]	–	840–500 HV0.2	0.1 mm ³
AISI 304 L SS-TiC [245]	82	220–500 HV0.1	
Steel-20 wt%TiB2/low carbon steel substrate [240]	–	900 HV0.2	0.24 mm ³
Fe-TiB2composite coating/1010 steel [246]	100	700–1000 HV0.2	5
AISI 316 L SS-SiC (5, 20 wt%)/mild steel [239,247]	25–40	340 VHN (for 5% SiC) 800 VHN (for 20% SiC)	–
Fe based alloy-VC/H13 steel [248]	–	900HV0.2	–
Fe-VC/1020 low carbon steel [237]	–	300–800 HV0.2	0.2 mm ³
AISI316–33,50 vol%Cr3C2/SS [249]	–45 /+5	45–57HRC0.2 (for 33 vol%) 52–58HRC0.2 (for 50 vol%)	25–35 times improvement (33 vol%) 42–88 times improvement (50 vol%)
Fe-based alloy-10,20%Cr3C2/35CrMo steel [250]	30–50	650–680HV0.2 (for 20%) (20% Cr3C2) 18 (10% Cr3C2)	5 – 1.2
304SS-10wt.%Al2O3/45steel [251]	45–100	600 HV	–
Fe based alloy-ZrC0.7/medium carbon steel [238]	74–100	1000–1200 HV0.2	–

10. Challenges, trends and opportunities

Metal AM processes have the potential to produce complex near-net-shape steel components. Various examples were found in the literature, where dense steel parts with acceptable properties were fabricated. However, there are significant challenges associated with LPB, LPF and BJ processes; some of the most significant ones are mentioned below:

- 1- There is a large number of process/design parameters such as, laser power, powder feed rate, laser traverse speed, layer thickness, scanning pattern, etc. involved in LPB and LPF manufacturing processes. As mechanical properties, thermal gradient and consequent microstructure of laser fabricated parts depend on the process parameters and interaction among them, it is vital to optimize these parameters to achieve near-net-shape components with minimal defects such as pores and inclusions. Therefore, novel and effective statistical approaches are required to consider all interdependencies of parameters while a minimum number of experiments is conducted. Within the context of new statistical approaches, much attention must be given to such higher-order interaction effects, which lead to systematic uncertainty in the resulting models and experimental achievements. In this regard, choosing the appropriate combined parameters is of vital importance for the statistical analysis as it is easier to consider their effect on porosity and mechanical properties of the AM parts instead of using individual parameters.
- 2- A vast majority of existing studies only investigate optimal process parameters for steels using simulation and/or experimental approach. A significant limitation is that, by changing the experimental conditions (e.g., material, process, system, or environmental conditions), the resulting optimal process parameters might no longer be applicable. Consequently, new experiments are needed to be

Table 12

Composite detail, process parameters, and properties of MMCs, manufactured in BJ process.

Composite Matrix-Vol% filler (method/substrate)	Filler (cemented) particle size (μm)	Heat treatment	YS (MPa)	Modulus (GPa)
17-4 PH SS-45 TZ-3Y-SE zirconia (suspensions based on heated binder mixture/dispersing agent) [252]	d50 = 0.3	Two-step de-binding: 270 °C (Air), 800 °C (Ar), Sintering-1350 °C (Ar)	–	–
Crofer22APU/17-4 PH SS-50 TZ-3Y-SE/TZ-3Y-E (suspensions based on heated binder mixture/dispersing agent) [253]	d50 (TZ-3Y-SE) = 0.180 d50 (TZ-3Y-E) = 0.105	Two-step de-binding: 270 °C (Air), 900 °C (Ar) Sintering-1400 °C (Ar/H ₂)	–	–
316 SS-20 TCP (mechanical mixing) [254,255] Layer thickness: 50 μm	–	Curing-150 °C, Sintering-1200 °C/8 h	798.713	–
316 SS-20 TCP (mechanical mixing) [254,255] Layer thickness: 200 μm	–	Curing-150 °C, Sintering-1200 °C/8 h	786.513	–
316 SS-20 TCP (mechanical mixing) [254] Layer thickness: 50 μm	5	Curing-175 °C, Sintering-1200 °C/4 h (Ar)	238.16	32.4
316 SS-20 TCP (mechanical mixing) [254] Layer thickness: 100 μm	5	Curing-175 °C, Sintering-1200 °C/4 h (Ar)	89.39	29.8
316 SS-40 TCP (mechanical mixing) [254] Layer thickness: 50 μm	5	Curing-175 °C, Sintering-1200 °C/4 h (Ar)	48.8	13.6
316SS-40 TCP (mechanical mixing) [254] Layer thickness: 100 μm	5	Curing-175 °C, Sintering-1200 °C/4 h (Ar)	31.7	15.7

- done from scratch. It is obvious from the data in the literature that it is extremely challenging to consolidate the data available due to the inconsistencies in the procedures and methodologies used for extracting data. As the AM community grows, the development of standard procedures is inevitable to help the community to interpret the data more effectively and prevent experimental duplication as much as possible.
- 3- Building orientation of steel parts fabricated via LPB and LPF may affect their thermal history. This is because of the anisotropic heat conduction along the built direction. As a result inhomogeneity in microstructure with elongated grains is formed that eventually leads to anisotropic mechanical properties. Post process heat treatment may eliminate the anisotropic property, but further investigation and validation of this approach is required. For example, Hot Isostatic Pressing (HIP) can significantly decrease the anisotropy in the building orientation by removing directional porosities; however, the HIP may cause a detrimental dimensional shrinkage. Another possible solution that to the best of our knowledge has not been considered yet in the literature is cooling of the substrate, for the sake of tempering, as soon as the AM process is completed. This would need to be carefully examined and effectively controlled.
- 4- Last but not least, the number of ferrous alloys deployed to AM processes is extremely limited. While there are >1000 steel alloys for conventional manufacturing (casting, forging, machining, etc.), there have not been many steel alloys deployed to AM by researchers and industry to-date. It becomes a more limiting factor when the number of qualified steel alloys offered by the AM Original Equipment Manufacturers (OEMs) is <10. Further efforts must be made to develop new steel alloys, which are better tailored to AM and also to deploy existing alloys to AM processes, for which imminent market opportunities are expected.

Acknowledgement

This study was carried out under the project, 'Additive manufacturing of ferrous alloys'. The authors gratefully acknowledge the financial support from the Federal Economic Development Agency for Southern Ontario (FedDev Ontario), Ontario Research Fund–Research Excellence, and Rio Tinto Metal Powders. The authors would also like to thank Zhidong Zhang, PhD student, for his contributions to the modeling section.

References

- [1] J.G.S.J. Laeng, F.W. Liou, Laser metal forming processes for rapid prototyping - a review, *Int. J. Prod. Res.* 38 (2000) 3973–3996, <https://doi.org/10.1080/00207540050176111>.
- [2] W.E. Frazier, Metal additive manufacturing: a review, *J. Mater. Eng. Perform.* 23 (2014) 1917–1928, <https://doi.org/10.1007/s11665-014-0958-z>.
- [3] L.E. Murr, E. Martinez, S.M. Gaytan, D.A. Ramirez, B.I. Machado, P.W. Shindo, J.L. Martinez, F. Medina, J. Wooten, D. Ciscl, U. Ackelid, R.B. Wicker, Microstructural architecture, microstructures, and mechanical properties for a nickel-base superalloy fabricated by electron beam melting, *Metall. Mater. Trans. A* 42 (2011) 3491–3508, <https://doi.org/10.1007/s11661-011-0748-z>.
- [4] L.E. Murr, S.M. Gaytan, D.A. Ramirez, E. Martinez, J. Hernandez, K.N. Amato, P.W. Shindo, F.R. Medina, R.B. Wicker, Metal fabrication by additive manufacturing using laser and electron beam melting technologies, *J. Mater. Sci. Technol.* 28 (2012) 1–14, [https://doi.org/10.1016/S1005-0302\(12\)60016-4](https://doi.org/10.1016/S1005-0302(12)60016-4).
- [5] D.D. Gu, W. Meiners, K. Wissenbach, R. Poprawe, Laser additive manufacturing of metallic components: materials, processes and mechanisms, *Int. Mater. Rev.* 57 (2012) 133–164, <https://doi.org/10.1179/1743280411Y.0000000014>.
- [6] I. Gibson, D. Rosen, B. Stucker, *Additive Manufacturing Technologies*, Springer New York, New York, NY, 2015, <https://doi.org/10.1007/978-1-4939-2113-3>.
- [7] L.E. Murr, E. Martinez, K.N. Amato, S.M. Gaytan, J. Hernandez, D.A. Ramirez, P.W. Shindo, F. Medina, R.B. Wicker, Fabrication of metal and alloy components by additive manufacturing: examples of 3D materials science, *J. Mater. Res. Technol.* 1 (2012) 42–54, [https://doi.org/10.1016/S2238-7854\(12\)70009-1](https://doi.org/10.1016/S2238-7854(12)70009-1).
- [8] P.A. Kobryn, S.L. Semiatin, Mechanical properties of laser-deposited Ti-6Al-4V, *Solid Free. Fabr. Proc.* Austin 2001, pp. 6–8.
- [9] A. Yadollahi, N. Shamsaei, S.M. Thompson, A. Elwany, L. Bian, Mechanical and microstructural properties of selective laser melted 17-4 PH stainless steel, *ASME 2015 Int. Mech. Eng. Congr. Expo*, American Society of Mechanical Engineers, 2015 (p. V02AT02A014-V02AT02A014).
- [10] N. Shamsaei, A. Yadollahi, L. Bian, S.M. Thompson, An overview of direct laser deposition for additive manufacturing; part II: mechanical behavior, process parameter optimization and control, *Addit. Manuf.* 8 (2015) 12–35, <https://doi.org/10.1016/j.addma.2015.07.002>.
- [11] V. Bhavar, P. Kattire, V. Patil, S. Khot, K. Gujar, R. Singh, A review on powder bed fusion technology of metal additive manufacturing, *4th Int. Conf. Exhib. Addit. Manuf. Technol Sept.*, 2014, pp. 1–2.
- [12] S.K. Tiwari, S. Pandey, S. Agrawal, S.M. Bobade, Selection of selective laser sintering materials for different applications, *Rapid Prototyp. J.* 21 (2015) 630–648, <https://doi.org/10.1108/rpj-03-2013-0027>.
- [13] H. Krauss, T. Zeugner, M.F. Zah, Layerwise monitoring of the selective laser melting process by thermography, *8th Int. Conf. Laser Assist. Net Shape Eng. LANE* 2014, 56, 2014, pp. 64–71, <https://doi.org/10.1016/j.phpro.2014.08.097>.
- [14] M. Alimardani, E. Toyserkani, J.P. Huissoon, C.P. Paul, On the delamination and crack formation in a thin wall fabricated using laser solid freeform fabrication process: an experimental-numerical investigation, *Opt. Lasers Eng.* 47 (2009) 1160–1168, <https://doi.org/10.1016/j.optlaseng.2009.06.010>.
- [15] C. Selcuk, Laser metal deposition for powder metallurgy parts, *Powder Metall.* 54 (2011) 94–99.
- [16] Y. Bai, G. Wagner, C.B. Williams, Effect of bimodal powder mixture on powder packing density and sintered density in binder jetting of metals, *2015 Annu. Int. Solid Free. Fabr. Symp.* 2015, p. 62.
- [17] K. Inaekyan, V. Paserin, I. Bailon-Poujol, V. Brailovski, V.P. Karine Inaekyan IanBailon-Poujol, Vladimir Brailovski, Binder-jetting additive manufacturing with water atomized iron powders, *AMP2016 Conf. Addit. Manuf.*, Boston, USA, 2016.
- [18] A. Bailey, A. Merriman, A. Elliott, M. Basti, Preliminary testing of nanoparticle effectiveness in binder jetting applications, *27th Annu. Int. Solid Free. Fabr. Symp.* 2016, pp. 1069–1077.
- [19] S.M. Allen, E.M. Sachs, Three-dimensional printing of metal parts for tooling and other applications, *Met. Mater.* 6 (2000) 589–594.
- [20] A. Basalah, Y. Shanjani, S. Esmaeli, E. Toyserkani, Characterizations of additive manufactured porous titanium implants, *J Biomed Mater Res B Appl Biomater* 100 (2012) 1970–1979.
- [21] Y. Tang, Y. Zhou, T. Hoff, M. Garon, Y.F. Zhao, Elastic modulus of 316 stainless steel lattice structure fabricated via binder jetting process, *Mater. Sci. Technol.* 32 (2016) 648–656.
- [22] Y. Zhou, Y. Tang, T. Hoff, M. Garon, F.Y. Zhao, The verification of the mechanical properties of binder jetting manufactured parts by instrumented indentation testing, *Procedia Manuf.* 1 (2015) 327–342, <https://doi.org/10.1016/j.promfg.2015.09.038>.
- [23] E.A. Rojas-Nastrucci, J. Nussbaum, T.M. Weller, N.B. Crane, Meshed rectangular waveguide for high power, low loss and reduced weight applications, *Microw. Symp. (IMS)*, 2016 IEEE MTT-S Int., IEEE 2016, pp. 1–4.
- [24] H. Chen, H. Chen, Y.F. Zhao, Process parameters optimization for improving surface quality and manufacturing accuracy of binder jetting additive manufacturing process, *Rapid Prototyp. J.* 22 (2016) 527–538.
- [25] W. Sames, *Additive Manufacturing of Inconel 718 Using Electron Beam Melting: Processing, Post-processing, & Mechanical Properties*, Texas A&M University, 2015.
- [26] L.E. Murr, S.M. Gaytan, A. Ceylan, E. Martinez, J.L. Martinez, D.H. Hernandez, B.I. Machado, D.A. Ramirez, F. Medina, S. Collins, R.B. Wicker, Characterization of titanium aluminide alloy components fabricated by additive manufacturing using electron beam melting, *Acta Mater.* 58 (2010) 1887–1894, <https://doi.org/10.1016/j.actamat.2009.11.032>.
- [27] H. Gong, K. Rafi, H. Gu, T. Starr, B. Stucker, Analysis of defect generation in Ti-6Al-4V parts made using powder bed fusion additive manufacturing processes, *Addit. Manuf.* 1 (2014) 87–98, <https://doi.org/10.1016/j.addma.2014.08.002>.
- [28] D. Cormier, O. Harrysson, H. West, Characterization of H13 steel produced via electron beam melting, *Rapid Prototyp. J.* 10 (2004) 35–41, <https://doi.org/10.1108/13552540410512516>.
- [29] R.R. Dehoff, M.M. Kirka, W.J. Sames, H. Bilheux, A.S. Tremsin, L.E. Lowe, S.S. Babu, Site specific control of crystallographic grain orientation through electron beam additive manufacturing, *Mater. Sci. Technol.* 31 (2015) 931–938, <https://doi.org/10.1179/1743284714Y.000000734>.
- [30] S.L. Sing, J. An, W.Y. Yeong, F.E. Wiria, Laser and electron-beam powder-bed additive manufacturing of metallic implants: a review on processes, materials and designs, *J. Orthop. Res.* 34 (2016) 369–385, <https://doi.org/10.1002/jor.23075>.
- [31] E.B.M. Arcam, Welcome to Manufaturing unbound, *Education* 40150 (2017) <https://doi.org/10.1080/03632415.2015.1027159>.
- [32] E. Toyserkani, A. Khajepour, S.F. Corbin, *Laser Cladding*, CRC Press, 2004.
- [33] P. Laakso, T. Riipinen, A. Laukkonen, T. Andersson, A. Jokinen, A. Revuelta, K. Ruusuvuori, Optimization and simulation of SLM process for high density H13 tool steel parts, *9th Int. Conf. Photonic Technol. LANE* 2016, 83, 2016, pp. 26–35, <https://doi.org/10.1016/j.phpro.2016.08.004>.
- [34] T. Nakamoto, N. Shirakawa, Y. Miyata, H. Inui, Selective laser sintering of high carbon steel powders studied as a function of carbon content, *J. Mater. Process. Technol.* 209 (2009) 5653–5660, <https://doi.org/10.1016/j.jmatprotex.2009.05.022>.
- [35] R. Mertens, B. Vrancken, N. Holmstock, Y. Kinds, J.-P. Kruth, J. Van Humbeeck, Influence of powder bed preheating on microstructure and mechanical properties of H13 tool steel SLM parts, *Phys. Procedia* 83 (2016) 882–890.
- [36] K. Kempen, B. Vrancken, S. Buls, L. Thijss, J. Van Humbeeck, J.-P. Kruth, Selective laser melting of crack-free high density M2 high speed steel parts by baseplate preheating, *J. Manuf. Sci. Eng.* 136 (2014), 61026, <https://doi.org/10.1115/1.4028513>.
- [37] B. Song, S. Dong, S. Deng, H. Liao, C. Coddet, Microstructure and tensile properties of iron parts fabricated by selective laser melting, *Opt. Laser Technol.* 56 (2014) 451–460, <https://doi.org/10.1016/j.optlastec.2013.09.017>.

- [38] M. Rombouts, J.P. Kruth, L. Froyen, P. Merce, Fundamentals of selective laser melting of alloyed steel powders fundamentals of selective laser melting of alloyed steel powders, *CIRP Ann. Manuf. Technol.* 55 (2006) 187–192, [https://doi.org/10.1016/S0007-8506\(07\)60395-3](https://doi.org/10.1016/S0007-8506(07)60395-3).
- [39] J.J.S. Dilip, G.D.J. Ram, T.L. Stair, B. Stucker, Selective laser melting of HY100 steel: process parameters, microstructure and mechanical properties, *Addit. Manuf.* 13 (2017) 49–60.
- [40] A. Simchi, Direct laser sintering of metal powders: mechanism, kinetics and microstructural features, *Mater. Sci. Eng. A* 428 (2006) 148–158, <https://doi.org/10.1016/j.msea.2006.04.117>.
- [41] A. Simchi, H. Pohl, Effects of laser sintering processing parameters on the microstructure and densification of iron powder, *Mater. Sci. Eng. A* 359 (2003) 119–128.
- [42] M. Mazur, M. Leary, M. McMillan, J. Elambasseril, M. Brandt, SLM additive manufacture of H13 tool steel with conformal cooling and structural lattices, *Rapid Prototyp. J.* 22 (2016) 504–518, <https://doi.org/10.1108/RPJ-06-2014-0075>.
- [43] L.N. Carter, X. Wang, N. Read, R. Khan, M. Aristizabal, K. Essa, M.M. Attallah, Process optimisation of selective laser melting using energy density model for nickel based superalloys, *Mater. Sci. Technol.* 32 (2016) 657–661.
- [44] I. Yadroitsev, M. Pavlov, P. Bertrand, I. Smurov, Mechanical Properties of Samples Fabricated by Selective Laser Melting, 14èmes Assises Eur. Du Prototypages Fabr. Rapide, Paris, 2009 24–25.
- [45] M. Garibaldi, I. Ashcroft, M. Simonelli, R. Hague, Metallurgy of high-silicon steel parts produced using selective laser melting, *Acta Mater.* 110 (2016) 207–216, <https://doi.org/10.1016/j.actamat.2016.03.037>.
- [46] Y.-A. Song, W. Koenig, Experimental study of the basic process mechanism for direct selective laser sintering of low-melting metallic powder, *CIRP Ann. Manuf. Technol.* 46 (1997) 127–130, [https://doi.org/10.1016/S0007-8506\(07\)60790-2](https://doi.org/10.1016/S0007-8506(07)60790-2).
- [47] H.J. Niu, I.T.H. Chang, Selective laser sintering of gas atomized M2 high speed steel powder, *J. Mater. Sci.* 35 (2000) 31–38.
- [48] M.M.A. Dewidar, Direct and Indirect Laser Sintering of Metals(PhD Thesis) <http://etheses.whiterose.ac.uk/id/eprint/3973> 2002.
- [49] R.B. Eane, *Metal Powder Effects on Selective Laser Sintering*, 2002.
- [50] D.E. Cooper, The High Deposition Rate Additive Manufacture of Nickel Superalloys and Metal Matrix Composites by, University of Warwick, 2016<http://webcat.warwick.ac.uk/record=b2876003-S1>.
- [51] A. Simchi, H. Asgharzadeh, Densification and microstructural evaluation during laser sintering of M2 high speed steel powder, *Mater. Sci. Technol.* 20 (2004) 1462–1468, <https://doi.org/10.1179/026708304X3944>.
- [52] A.B. Spierings, G. Levy, Comparison of density of stainless steel 316 L parts produced with selective laser melting using different powder grades, *Proc. Annu. Int. Solid Free. Fabr. Symp.*, Austin, TX 2009, pp. 342–353.
- [53] E. Jelis, M. Clemente, S. Kerwien, N.M. Ravindra, M.R. Hespas, Metallurgical and mechanical evaluation of 4340 steel produced by direct metal laser sintering, *JOM* 67 (2015) 582–589.
- [54] H. Irrinki, Mechanical Properties and Microstructure Evolution of 17-4 PH Stainless Steel Processed by Laser-Powered Bed Fusion, 2016.
- [55] P.A. Lykov, E.V. Safonov, A.M. Akhmedianov, Selective laser melting of copper, *Mater. Sci. Forum, Trans Tech Publ* 2016, pp. 284–288.
- [56] R. Mahshid, H.N. Hansen, K.L. Hojbjørre, Strength analysis and modeling of cellular lattice structures manufactured using selective laser melting for tooling applications, *Mater. Des.* 104 (2016) 276–283, <https://doi.org/10.1016/j.matdes.2016.05.020>.
- [57] H. Chen, D. Gu, D. Dai, C. Ma, M. Xia, Microstructure and composition homogeneity, tensile property, and underlying thermal physical mechanism of selective laser melting tool steel parts, *Mater. Sci. Eng. A* 682 (2017) 279–289, <https://doi.org/10.1016/j.msea.2016.11.047>.
- [58] I. Yadroitsev, P. Krakhmalev, I. Yadroitseva, Hierarchical design principles of selective laser melting for high quality metallic objects, *Addit. Manuf.* 7 (2015) 45–56, <https://doi.org/10.1016/j.addma.2014.12.007>.
- [59] X. Zhao, B. Song, Y. Zhang, X. Zhu, Q. Wei, Y. Shi, Decarburization of stainless steel during selective laser melting and its influence on Young's modulus, hardness and tensile strength, *Mater. Sci. Eng. A* 647 (2015) 58–61.
- [60] C.D. Boley, S.C. Mitchell, A.M. Rubenchik, S.S.Q. Wu, Metal powder absorptivity: modeling and experiment, *Appl. Opt.* 55 (2016) 6496–6500, <https://doi.org/10.1364/AO.55.006496>.
- [61] M. Van Elsen, F. Al-Bender, J.-P. Kruth, Application of dimensional analysis to selective laser melting, *Rapid Prototyp. J.* 14 (2008) 15–22, <https://doi.org/10.1016/13552540810841526>.
- [62] L. Battizzati, A.L. Greer, The viscosity of liquid metals and alloys, *Acta Metall.* 37 (1989) 1791–1802, [https://doi.org/10.1016/0001-6160\(89\)90064-3](https://doi.org/10.1016/0001-6160(89)90064-3).
- [63] I. Egry, G. Lohöfer, S. Sauerland, Surface tension and viscosity of liquid metals, *J. Non-Cryst. Solids* 156 (1993) 830–832, [https://doi.org/10.1016/0022-3093\(93\)90079-D](https://doi.org/10.1016/0022-3093(93)90079-D).
- [64] R.N. Singh, F. Sommer, Viscosity of liquid alloys: generalization of Andrade's equation, *Monatsh. Chem. Chem. Mon.* 143 (2012) 1235–1242, <https://doi.org/10.1007/s00706-012-0728-2>.
- [65] I. Egry, E. Ricci, R. Novakovic, S. Ozawa, Surface tension of liquid metals and alloys – recent developments, *Adv. Colloid Interf. Sci.* 159 (2010) 198–212, <https://doi.org/10.1016/j.cis.2010.06.009>.
- [66] F.A. Halden, W.D. Kingery, Surface tension at elevated temperatures. II. Effect of C, N, O and S on liquid iron surface tension and interfacial energy with Al₂O₃, *J. Phys. Chem.* 59 (1955) 557–559, <https://doi.org/10.1021/j150528a018>.
- [67] W.M. Steen, J. Mazumder, Theory, mathematical modelling and simulation, *Laser Mater. Process.*, Springer London, London 2010, pp. 251–294 (doi:10.1007/978-1-84996-062-5_6" data-bbox="74 885 493 918">10.1007/978-1-84996-062-5_6").
- [68] F. Incropera, D. DeWitt, *Fundamentals of Heat and Mass Transfer*, 5th Edition Wiley, 2001 (doi:citeulike-article-id:7020383).
- [69] M. Dourandish, D. Godlinski, A. Simchi, 3D printing of biocompatible PM-materials, *Mater. Sci. Forum, Trans Tech Publ* 2007, pp. 453–456.
- [70] P. Nandwana, A.M. Elliott, D. Siddel, A. Merriman, W.H. Peter, S.S. Babu, Powder bed binder jet 3D printing of Inconel 718: densification, microstructural evolution and challenges☆, *Curr. Opin. Solid State Mater. Sci.* 21 (2017) 207–218.
- [71] M. Ziaeef, E.M. Tridas, N.B. Crane, E.M.T. Mohsen Ziaeef, Nathan B. Crane, Binder-jet printing of fine stainless steel powder with varied final density, *JOM* 69 (2017) 592–596.
- [72] Y. Bai, C.B. Williams, An exploration of binder jetting of copper, *Rapid Prototyp. J.* 21 (2015) 177–185.
- [73] M. Letenneur, V. Brailovski, A. Kreitberg, V. Paserin, I. Bailon-Poujol, Laser powder bed fusion of water-atomized iron-based powders: process optimization, *J. Manuf. Mater. Process.* 1 (2017) 23, <https://doi.org/10.3390/jmmp1020023>.
- [74] B. Al-Mangour, Powder metallurgy of stainless steel: state-of-the art, challenges, and development, *Stainl. Steel* (2015) 37–80.
- [75] S. Hoeges, C.T. Schade, R. Causton, Development of a maraging steel powder for additive manufacturing, *MPIF World Congr. Powder Metall. Part. Mater.*, 2015.
- [76] Y. Sun, R.J. Hebert, M. Aindow, Non-metallic inclusions in 17-4PH stainless steel parts produced by selective laser melting, *Mater. Des.* 140 (2018) 153–162, <https://doi.org/10.1016/j.matdes.2017.11.063>.
- [77] K. Kempen, E. Yasa, L. Thijss, J.-P. Kruth, J. Van Humbeeck, Microstructure and mechanical properties of selective laser melted 18Ni-300 steel, *Phys. Procedia* 12 (2011) 255–263, <https://doi.org/10.1016/j.phpro.2011.03.033>.
- [78] R. Frykholm, Y. Takeda, B.-G. Andersson, R. Carlstrom, Solid state sintered 3-D printing component by using inkjet (binder) method, *J. Jpn. Soc. Powder Powder Metall.* 63 (2016) 421–426, <https://doi.org/10.2497/jjspm.63.421>.
- [79] E. Yasa, K. Kempen, J.-P. Kruth, L. Thijss, J. Van Humbeeck, Microstructure and mechanical properties of maraging steel 300 after selective laser melting, *Solid Free. Fabr. Symp. Proc.* 2010, pp. 383–396.
- [80] K. Kempen, Expanding the Materials Palette for Selective Laser Melting of Metals, 2015.
- [81] E. Yasa, J. Deckers, J.-P. Kruth, M. Rombouts, J. Luyten, Charpy impact testing of metallic selective laser melting parts, *Virtual Phys. Prototyp.* 5 (2010) 89–98.
- [82] E. Yasa, J. Deckers, J.-P. Kruth, M. Rombouts, J. Luyten, Experimental investigation of Charpy impact tests on metallic SLM parts, *Innov. Dev. Des. Manuf. Adv. Res. Virtual Rapid Prototyp* 2009, pp. 207–214.
- [83] C. Tan, K. Zhou, X. Tong, Y. Huang, J. Li, W. Ma, F. Li, T. Kuang, Microstructure and Mechanical Properties of 18Ni-300 Maraging Steel Fabricated by Selective Laser Melting, *Proc. 2016 6th Int. Conf. Adv. Des. Manuf. Eng. (ICADME 2016)*, 2016.
- [84] D. Koutny, L. Pantalejev, J. Tomes, D. Palousek, Comparison of selective laser melting of 18Ni maraging steel by Px1 and M2 cusing, *MM Sci. J.* 2016 (2016) 1590–1596, https://doi.org/10.17973/MMSJ.2016.12_2016191.
- [85] T. Hermann Becker, T. Hermann Becker, D. Dimitrov, D. Dimitrov, The achievable mechanical properties of SLM produced maraging steel 300 components, *Rapid Prototyp. J.* 22 (2016) 487–494.
- [86] W. Du, Q. Bai, B. Zhang, A novel method for additive/subtractive hybrid manufacturing of metallic parts, *Procedia Manuf.* 5 (2016) 1018–1030.
- [87] C. Casavola, S.L. Campanelli, C. Pappalettere, Experimental analysis of residual stresses in the selective laser melting process, *Proceedings Xlth Int. Congr. Expo.* Orlando, Florida, USA, 2008.
- [88] G. Casalino, S.L. Campanelli, N. Contuzzi, A.D. Ludovico, Experimental investigation and statistical optimisation of the selective laser melting process of a maraging steel, *Opt. Laser Technol.* 65 (2015) 151–158, <https://doi.org/10.1016/j.optlastec.2014.07.021>.
- [89] G. Bi, A. Gasser, K. Wissenbach, A. Drenker, R. Poprawe, Characterization of the process control for the direct laser metallic powder deposition, *Surf. Coat. Technol.* 201 (2006) 2676–2683.
- [90] J. Choi, Y. Chang, Characteristics of laser aided direct metal/material deposition process for tool steel, *Int. J. Mach. Tools Manuf.* 45 (2005) 597–607.
- [91] J. Mazumder, A. Schifferer, J. Choi, Direct materials deposition: designed macro and microstructure, *Mater. Res. Innov.* 3 (1999) 118–131.
- [92] J. Zhao, W. Cao, C. Ge, Y. Tan, Y. Zhang, Q. Fei, Research on laser engineered net shaping of thick-wall nickel-based alloy parts, *Rapid Prototyp. J.* 15 (2009) 24–28.
- [93] Y. Yang, J.Y.H. Fuh, H.T. Loh, Y.S. Wong, A volumetric difference-based adaptive slicing and deposition method for layered manufacturing, *Trans. Soc. Mech. Eng. J. Manuf. Sci. Eng.* 125 (2003) 586–594.
- [94] A. Dolenc, I. Mäkelä, Slicing procedures for layered manufacturing techniques, *Comput. Des.* 26 (1994) 119–126.
- [95] P. Singh, D. Dutta, Multi-direction slicing for layered manufacturing, *J. Comput. Inf. Sci. Eng.* 1 (2001) 129–142.
- [96] Y. Yang, J.Y.H. Fuh, H.T. Loh, Y. San Wong, Minimizing staircase errors in the orthogonal layered manufacturing system, *IEEE Trans. Autom. Sci. Eng.* 2 (2005) 276–284.
- [97] T. Do, C.S. Shin, D. Stetsko, G. VanConant, A. Vartanian, S. Pei, P. Kwon, Improving structural integrity with boron-based additives for 3D printed 420 stainless steel, *Procedia Manuf.* 1 (2015) 263–272.
- [98] T. Do, P. Kwon, C.S. Shin, Process development toward full-density stainless steel parts with binder jetting printing, *Int. J. Mach. Tools Manuf.* 121 (2017) 50–60, <https://doi.org/10.1016/j.ijmachtools.2017.04.006>.
- [99] L. Sun, Y.-H. Kim, P. Kwon, Densification and properties of 420 stainless steel produced by three-dimensional printing with addition of Si₃N₄ powder, *J. Manuf. Sci. Eng.* 131 (2009), 61001.
- [100] William F. Gale, Terry C. Totemeier, Smithells Metals Reference Book, Eighth, Elsevier Science, Burlington, 2003<https://www.elsevier.com/books/smithells-metals-reference-book/gale/978-0-7506-7509-3>.

- [101] A. Elliott, S. AlSalhi, A.L. Merriman, M.M. Basti, Infiltration of nanoparticles into porous binder jet printed parts, *Am. J. Eng. Appl. Sci.* 9 (2016).
- [102] N.B. Crane, J. Wilkes, E. Sachs, S.M. Allen, Improving accuracy of powder-based SFF processes by metal deposition from a nanoparticle dispersion, *Rapid Prototyp. J.* 12 (2006) 266–274.
- [103] E. Sachs, E. Wylonis, S. Allen, M. Cima, H. Guo, Production of injection molding tooling with conformal cooling channels using the three dimensional printing process, *Polym. Eng. Sci.* 40 (2000) 1232–1247, <https://doi.org/10.1002/pen.11251>.
- [104] Z.C. Cordero, D.H. Siddle, W.H. Peter, A.M. Elliott, Strengthening of ferrous binder jet 3D printed components through bronze infiltration, *Addit. Manuf.* 15 (2017) 87–92, <https://doi.org/10.1016/j.addma.2017.03.011>.
- [105] T. Kasuya, N. Yurioka, Carbon equivalent and multiplying factor for hardenability of steel, *Weld. Res. Suppl.*, Detroit Mich. 1993 (p. 263–s–268–s) http://files.aws.org/wj/supplement/WJ_1993_06_s263.pdf.
- [106] S. Cheruvathur, E.A. Lass, C.E. Campbell, Additive manufacturing of 17-4 PH stainless steel: post-processing heat treatment to achieve uniform reproducible microstructure, *JOM* 68 (2016) 930–942, <https://doi.org/10.1007/s11837-015-1754-4>.
- [107] E. Liverani, S. Toschi, L. Ceschin, A. Fortunato, Effect of selective laser melting (SLM) process parameters on microstructure and mechanical properties of 316 L austenitic stainless steel, *J. Mater. Process. Technol.* 249 (2017) 255–263, <https://doi.org/10.1016/j.jmatprote.2017.05.042>.
- [108] J. Yu, M. Rombouts, G. Maes, Cracking behavior and mechanical properties of austenitic stainless steel parts produced by laser metal deposition, *Mater. Des.* 45 (2013) 228–235.
- [109] L. Wang, S. Felicelli, Process modeling in laser deposition of multilayer SS410 steel, *J. Manuf. Sci. Eng.* 129 (2007) 1028–1034.
- [110] P.A. Kobryn, E.H. Moore, S.L. Semiatin, Effect of laser power and traverse speed on microstructure, porosity, and build height in laser-deposited Ti-6Al-4V, *Scr. Mater.* 43 (2000) 299–305, [https://doi.org/10.1016/S1359-6462\(00\)00408-5](https://doi.org/10.1016/S1359-6462(00)00408-5).
- [111] J.K. Wessel, *The Handbook of Advanced Materials: Enabling New Designs, Functionally Graded Materials*, John Wiley & Sons, 2004.
- [112] J.E. Smugeresky, D.D. Gill, C.J. Atwood, New Low Cost Material Development Technique for Advancing Rapid Prototyping Manufacturing Technology, 2007 1–39 <http://www.osti.gov/servlets/purl/926378-Q96D62/>.
- [113] J.-P.P. Kruth, L. Froyen, J. Van Vaerenbergh, P. Mercelis, M. Rombouts, B. Lauwers, Selective laser melting of iron-based powder, 14th International Symp. Electromachining (ISEM XIV), 149, 2004, pp. 616–622, <https://doi.org/10.1016/j.jmatprotec.2003.11.051>.
- [114] L. Wang, P. Pratt, S.D. Felicelli, H. El Kadiri, J.T. Berry, P.T. Wang, M.F. Horstemeyer, Experimental analysis of porosity formation in laser-assisted powder deposition process, 2009 TMS Annu. Meet. Exhib., 2009.
- [115] J.B. Ferguson, B.F. Schultz, A.D. Moghadam, P.K. Rohatgi, Semi-empirical model of deposit size and porosity in 420 stainless steel and 4140 steel using laser engineered net shaping, *J. Manuf. Process.* 19 (2015) 163–170.
- [116] H.A. Hamza, C. Smith, L. Hao, Effect of build orientation on the surface quality, microstructure and mechanical properties of selective laser melting 316 L stainless steel, *Rapid Prototyp. J.* (0) (2017) <https://doi.org/10.1108/RPJ-04-2016-0068>.
- [117] J. Choi, Y. Hua, Dimensional and material characteristics of direct deposited H13 tool steel by CO₂ laser, *J. Laser Appl.* 16 (2004) 245–251.
- [118] B. Zheng, Y. Zhou, J.E. Smugeresky, J.M. Schoenung, E.J. Lavernia, Thermal behavior and microstructure evolution during laser deposition with laser-engineered net shaping: part II. Experimental investigation and discussion, *Metall. Mater. Trans. A* 39 (2008) 2237–2245.
- [119] J.D. Majumdar, A. Pinkerton, Z. Liu, I. Manna, L. Li, Microstructure characterisation and process optimization of laser assisted rapid fabrication of 316 L stainless steel, *Appl. Surf. Sci.* 247 (2005) 320–327.
- [120] L. Thijss, F. Verhaeghe, T. Craeghs, J. Van Humbeeck, J.-P. Kruth, J. Van Humbeeck, J.-P. Kruth, A study of the microstructural evolution during selective laser melting of Ti-6Al-4V, *Acta Mater.* 58 (2010) 3303–3312, <https://doi.org/10.1016/j.actamat.2010.02.004>.
- [121] X. Tan, Y. Kok, Y.J. Tan, M. Descouins, D. Mangelinck, S.B. Tor, K.F. Leong, C.K. Chua, Graded microstructure and mechanical properties of additive manufactured Ti-6Al-4V via electron beam melting, *Acta Mater.* 97 (2015) 1–16, <https://doi.org/10.1016/j.actamat.2015.06.036>.
- [122] J.D. Hunt, Steady state columnar and equiaxed growth of dendrites and eutectic, *Mater. Sci. Eng.* 65 (1984) 75–83.
- [123] D. Wang, C. Song, Y. Yang, Y. Bai, Investigation of crystal growth mechanism during selective laser melting and mechanical property characterization of 316 L stainless steel parts, *Mater. Des.* 100 (2016) 291–299, <https://doi.org/10.1016/j.matdes.2016.03.111>.
- [124] L. Thijss, K. Kempen, J.-P. Kruth, J. Van Humbeeck, Fine-structured aluminium products with controllable texture by selective laser melting of pre-alloyed AlSi10Mg powder, *Acta Mater.* 61 (2013) 1809–1819, <https://doi.org/10.1016/j.actamat.2012.11.052>.
- [125] D. Herzog, V. Seyda, E. Wycisk, C. Emmelmann, Additive manufacturing of metals, *Acta Mater.* 117 (2016) 371–392, <https://doi.org/10.1016/j.actamat.2016.07.019>.
- [126] K. Zhang, S. Wang, W. Liu, X. Shang, Characterization of stainless steel parts by laser metal deposition shaping, *Mater. Des.* 55 (2014) 104–119.
- [127] I. Yadroitsev, I. Yadroitseva, I. Smurov, Strategy of fabrication of complex shape parts based on the stability of single laser melted track, SPIE-The Int. Soc. Opt. Eng., San Francisco, California, United States, 2011 <https://doi.org/10.1117/12.875402> (p. 79210C-79210C-13).
- [128] Z. Sun, X. Tan, S.B. Tor, W.Y. Yeong, Selective laser melting of stainless steel 316 L with low porosity and high build rates, *Mater. Des.* 104 (2016) 197–204, <https://doi.org/10.1016/j.matdes.2016.05.035>.
- [129] W.M. Tucho, V.H. Lysne, H. Austbø, A. Sjolyst-Kverneland, V. Hansen, Investigation of effects of process parameters on microstructure and hardness of SLM manufactured SS316 L, *J. Alloys Compd.* 740 (2018) 910–925, <https://doi.org/10.1016/j.jallcom.2018.01.098>.
- [130] A. Yadollahi, N. Shamsaei, S.M. Thompson, D.W. Seely, Effects of process time interval and heat treatment on the mechanical and microstructural properties of direct laser deposited 316 L stainless steel, *Mater. Sci. Eng. A* 644 (2015) 171–183.
- [131] K. Abd-Elghany, D.L. Bourell, Property evaluation of 304 L stainless steel fabricated by selective laser melting, *Rapid Prototyp. J.* 18 (2012) 420–428.
- [132] H. Yu, J. Yang, J. Yin, Z. Wang, X. Zeng, Comparison on mechanical anisotropies of selective laser melted Ti-6Al-4V alloy and 304 stainless steel, *Mater. Sci. Eng. A* 695 (2017) 92–100, <https://doi.org/10.1016/j.msea.2017.04.031>.
- [133] S.M.A., J.W. Elmer, T.W. Eagar, Microstructural development during solidification of stainless steel alloys, *Metall. Trans. A* 20 (1989) 2117–2131.
- [134] L. Facchini, N. Vicente, I. Lonardelli, E. Magalini, P. Robotti, A. Molinari, Metastable austenite in 17–4 precipitation-hardening stainless steel produced by selective laser melting, *Adv. Eng. Mater.* 12 (2010) 184–188.
- [135] A. Kudzal, B. McWilliams, C. Hofmeister, F. Kellogg, J. Yu, J. Taggart-Scarff, J. Liang, Effect of scan pattern on the microstructure and mechanical properties of powder bed fusion additive manufactured 17-4 stainless steel, *Mater. Des.* 133 (2017) 205–215, <https://doi.org/10.1016/j.matdes.2017.07.047>.
- [136] T. LeBrun, T. Nakamoto, K. Horikawa, H. Kobayashi, Effect of retained austenite on subsequent thermal processing and resultant mechanical properties of selective laser melted 17-4 PH stainless steel, *Mater. Des.* 81 (2015) 44–53.
- [137] A. Yadollahi, N. Shamsaei, S.M. Thompson, A. Elwany, L. Bian, Effects of building orientation and heat treatment on fatigue behavior of selective laser melted 17-4 PH stainless steel, *Fatigue Fract. Behav. Addit. Manuf. Parts.* 94 (2017) 218–235, <https://doi.org/10.1016/j.jifatigue.2016.03.014>.
- [138] B. AlMangour, J.M. Yang, Understanding the deformation behavior of 17-4 precipitate hardenable stainless steel produced by direct metal laser sintering using micropillar compression and TEM, *Int. J. Adv. Manuf. Technol.* 90 (2017) 119–126, <https://doi.org/10.1007/s00170-016-9367-9>.
- [139] B. AlMangour, J.-M. Yang, Improving the surface quality and mechanical properties by shot-peening of 17-4 stainless steel fabricated by additive manufacturing, *Mater. Des.* 110 (2016) 914–924, <https://doi.org/10.1016/j.matdes.2016.08.037>.
- [140] B. AlMangour, J.M. Yang, Integration of heat treatment with shot peening of 17-4 stainless steel fabricated by direct metal laser sintering, *JOM* 69 (2017) 2309–2313, <https://doi.org/10.1007/s11837-017-2538-9>.
- [141] E.A. Jägle, Z. Sheng, P. Kürnsteiner, S. Ocylok, A. Weisheit, D. Raabe, Comparison of maraging steel micro- and nanostructure produced conventionally and by laser additive manufacturing, *Materials (Basel)* 10 (2017) 8, <https://doi.org/10.3390/ma10010008>.
- [142] C. Tan, K. Zhou, W. Ma, P. Zhang, M. Liu, T. Kuang, Microstructural evolution, nanoprecipitation behavior and mechanical properties of selective laser melted high-performance grade 300 maraging steel, *Mater. Des.* 134 (2017) 23–34, <https://doi.org/10.1016/j.matdes.2017.08.026>.
- [143] J.M. Pardal, S.S.M. Tavares, V.F. Terra, M.R. Da Silva, D.R. Dos Santos, Modeling of precipitation hardening during the aging and overaging of 18Ni-Co-Mo-Ti maraging 300 steel, *J. Alloys Compd.* 393 (2005) 109–113, <https://doi.org/10.1016/j.jallcom.2004.09.049>.
- [144] S.L. Campanelli, A. Angelastro, C.G. Signorile, G. Casalino, Investigation on direct laser powder deposition of 18 Ni (300) marage steel using mathematical model and experimental characterisation, *Int. J. Adv. Manuf. Technol.* (2016) 1–11.
- [145] P. Krakhmalev, I. Yadroitseva, G. Fredriksson, I. Yadroitsev, In situ heat treatment in selective laser melted martensitic AISI 420 stainless steels, *Mater. Des.* 87 (2015) 380–385, <https://doi.org/10.1016/j.matdes.2015.08.045>.
- [146] G.A. Ravi, X. Hao, N. Wain, X. Wu, M.M. Attallah, Direct laser fabrication of three dimensional components using SC420 stainless steel, *Mater. Des.* 47 (2013) 731–736.
- [147] X. Yue, J.C. Lippold, B.T. Alexandrov, S.S. Babu, continuous cooling transformation behavior in the CGHAZ of naval steels, *Weld. J.* 91 (2012) (67s–75s).
- [148] X. Yue, J.C. Lippold, Evaluation of heat-affected zone hydrogen-induced cracking in navy steels, *Weld. J.* 92 (2013) 20S–28S.
- [149] W. Wang, S. Kelly, A metallurgical evaluation of the powder-bed laser additive manufactured 4140 steel material, *JOM* 68 (2016) 869–875, <https://doi.org/10.1007/s11837-015-1804-y>.
- [150] Y. Lee, M. Nordin, S. Babu, D. Farson, Influence of fluid convection on weld pool formation in laser cladding, *Weld. J.* 93 (2014) (29S–300S).
- [151] S.Y. Wen, Y.C. Shin, J.Y. Murthy, P.E. Sojka, Modeling of coaxial powder flow for the laser direct deposition process, *Int. J. Heat Mass Transf.* 52 (2009) 5867–5877, <https://doi.org/10.1016/j.ijheatmasstransfer.2009.07.018>.
- [152] X. He, J. Mazumder, Transport phenomena during direct metal deposition advertisement, *J. Appl. Phys.* 53113 (2007) 53113, <https://doi.org/10.1063/1.2710780>.
- [153] M. Alimardani, E. Toyserkani, J.P. Huissoon, A 3D dynamic numerical approach for temperature and thermal stress distributions in multilayer laser solid freeform fabrication process, *Opt. Lasers Eng.* 45 (2007) 1115–1130, <https://doi.org/10.1016/j.optlastec.2007.06.010>.
- [154] Y. Liu, J. Zhang, Z. Pang, Numerical and experimental investigation into the subsequent thermal cycling during selective laser melting of multi-layer 316 L stainless steel, *Opt. Laser Technol.* 98 (2018) 23–32, <https://doi.org/10.1016/j.optlastec.2017.07.034>.
- [155] E.T.A. Fathi, A. Khajepour, M. Durali, Prediction of melt pool depth and dilution in laser powder deposition, *J. Phys. D. Appl. Phys.* 39 (2006) 2613–2623.
- [156] H. Tan, J. Chen, F. Zhang, X. Lin, W. Huang, Estimation of laser solid forming process based on temperature measurement, *Opt. Laser Technol.* 42 (2010) 47–54, <https://doi.org/10.1016/j.optlastec.2009.04.016>.

- [157] Y. Huang, M.B. Khamesee, E. Toyserkani, A comprehensive analytical model for laser powder-fed additive manufacturing, *Addit. Manuf.* 12 (2016) 90–99, <https://doi.org/10.1016/j.addma.2016.07.001>.
- [158] A.B.C. Körner, E. Attar, Fundamental consolidation mechanisms during selective beam melting of powders, *Model. Simul. Mater. Sci. Eng.* 21 (2013), 85011.
- [159] S.A. Khairallah, A. Anderson, Mesoscopic simulation model of selective laser melting of stainless steel powder, *J. Mater. Process. Technol.* 214 (2014) 2627–2636, <https://doi.org/10.1016/j.jmatprotec.2014.06.001>.
- [160] K.T.A. Garg, M.M. Savalani, State-of-the-art in empirical modelling of rapid prototyping processes, *Rapid Prototyp. J.* 20 (2014) 164–178, <https://doi.org/10.1108/RPJ-08-2012-0072>.
- [161] C. Panisawas, C. Qiu, M.J. Anderson, Y. Sovani, R.P. Turner, M.M. Attallah, J.W. Brooks, H.C. Basoalto, Mesoscale modelling of selective laser melting: thermal fluid dynamics and microstructural evolution, *Comput. Mater. Sci.* 126 (2017) 479–490, <https://doi.org/10.1016/j.commatsci.2016.10.011>.
- [162] J.P.K.P. Mercelis, Residual stresses in selective laser sintering and selective laser melting, *Rapid Prototyp. J.* 12 (2006) 254–265, <https://doi.org/10.1108/13552540610707013>.
- [163] M. Shiomi, K. Osakada, K. Nakamura, T. Yamashita, F. Abe, Residual stress within metallic model made by selective laser melting process, *CIRP Ann.* 53 (2004) 195–198, [https://doi.org/10.1016/S0007-8506\(07\)60067-5](https://doi.org/10.1016/S0007-8506(07)60067-5).
- [164] M.F. Knol, Thermal Modelling of Selective Laser Melting: A Semi-analytical Approach, Delft University of Technology, 2016 <https://repository.tudelft.nl/islandora/object/uuid%3Ae6b406fe-0b13-4fc-8e13-da961b3f3718>.
- [165] M. Alimardani, E. Toyserkani, J.P. Huissoon, Three-dimensional numerical approach for geometrical prediction of multilayer laser solid freeform fabrication process, *J. Laser Appl.* 19 (2007) 14–25, <https://doi.org/10.2351/1.2402518>.
- [166] I. Tabernero, A. Lamikiz, E. Ukar, L.N.L. de Lacalle, C. Angulo, G. Urbikain, L.N. López de Lacalle, C. Angulo, G. Urbikain, Numerical simulation and experimental validation of powder flux distribution in coaxial laser cladding, *J. Mater. Process. Technol.* 210 (2010) 2125–2134, <https://doi.org/10.1016/j.jmatprotec.2010.07.036>.
- [167] D.A. de Moraes, A. Czekanski, Thermal modeling of 304 L stainless steel for selective laser melting: laser power input evaluation, *Adv. Manuf.*, ASME, Vol. 2, , 2017 <https://doi.org/10.1115/IMECE2017-7224> (p. V002T02A033).
- [168] A.V. Gusarov, I. Yadroitsev, P. Bertrand, I. Smurov, Heat transfer modelling and stability analysis of selective laser melting, *Laser Synth. Process. Adv. Mater.* 254 (2007) 975–979, <https://doi.org/10.1016/j.japsusc.2007.08.074>.
- [169] I.Y.A.V. Gusarov Ph, I. Smurov Bertrand, Model of radiation and heat transfer in laser-powder interaction zone at selective laser melting, *J. Heat Transf.* 131 (2009), 72101.
- [170] J.Y. Chen, Xue, Microstructural characteristics of laser-clad AISI P20 tool steel, *Proc. 1st Int. Surf. Eng. Congr. 13th IFHTSE Congr. Mater. Park ASM Int* 2002, p. 198.
- [171] G. Link, Layered Manufacturing of Laser-Deposited Carbon Steels, 2000.
- [172] M. Griffith, M. Schlienger, L. Harwell, Thermal Behavior in the LENS Process, Solid Free. Fabr. Symp. Proceedings, Austin, TX, 1998.
- [173] G. Ramdeen Link, Layered Manufacturing of Laser-deposited Carbon Steels, Stanford University, 2000 (ocw.stanford.edu/304643712?accountid=14906).
- [174] H. El Kadiri, L. Wang, M.F. Horstemeyer, R.S. Yassar, J.T. Berry, S. Felicelli, P.T. Wang, Phase transformations in low-alloy steel laser deposits, *Mater. Sci. Eng. A* 494 (2008) 10–20.
- [175] L. Costa, R. Vilar, T. Reti, A.M. Deus, Rapid tooling by laser powder deposition: process simulation using finite element analysis, *Acta Mater.* 53 (2005) 3987–3999.
- [176] S.R. Lewis, R. Lewis, D.J. Fletcher, Assessment of laser cladding as an option for repair of rails, *Int. Conf. Contact Mech. Wear Rail/Wheel Syst.*, 330, 2012, pp. 380–385.
- [177] Z. Bergant, J. Grum, Heat treatment effects of laser cladded 12 Ni Maraging tool steel with Ni-co-Mo alloys, *HTM J. Heat Treat. Mater.* 69 (2014) 114–123.
- [178] Z. Bergant, J. Grum, Influence of laser deposition technique on surface integrity of 12 Ni maraging tool steel, *Int. J. Microstruct. Mater. Prop.* 8 (2013) 17–26.
- [179] B. Zoran, S.J. Marko, O.J. Luis, G. Janez, Laser cladding and heat treatment of Ni-Co-Mo maraging steel, *J. ASTM Int.* 8 (2011) 1–12.
- [180] J.J. Hammell, M.A. Langerman, N.P. Saunders, Radiometri and metallurgical analysis of zone formation in elementary laser deposited thin-wall structures, *ASME 2013 Int. Mech. Eng. Congr. Expo., American Society of Mechanical Engineers, 2013* (p. V02AT02A001-V02AT02A001).
- [181] R.S. Amano, S. Marek, B.F. Schultz, P.K. Rohatgi, Laser engineered net shaping process for 316/15% nickel coated titanium carbide metal matrix composite, *J. Manuf. Sci. Eng.* 136 (2014), 51007.
- [182] C.H. Gür, B.O. Tuncer, Investigating the microstructure-ultrasonic property relationships in steels, 16th WCNDT-World Conf. NDT, 2004.
- [183] A.S.M.I.H. Committee, *ASM Handbook-Volume 1: Properties and Selection: Irons, Steels, and High Performance Alloys*, ASM Int., 1990 950–980.
- [184] J. Li, D. Deng, X. Hou, X. Wang, G. Ma, D. Wu, G. Zhang, Microstructure and performance optimisation of stainless steel formed by laser additive manufacturing, *Mater. Sci. Technol.* 32 (2016) 1223–1230.
- [185] K. Saiedi, L. Kvetková, F. Lofaj, Z. Shen, Austenitic stainless steel strengthened by the in situ formation of oxide nanoinclusions, *RSC Adv.* 5 (2015) 20747–20750, <https://doi.org/10.1039/C4RA16721J>.
- [186] D. Wang, D. Wang, Y. Liu, Y. Liu, Y. Yang, Y. Yang, D. Xiao, D. Xiao, Theoretical and experimental study on surface roughness of 316 L stainless steel metal parts obtained through selective laser melting, *Rapid Prototyp. J.* 22 (2016) 706–716.
- [187] P. Krakhmalev, I. Yadroitseva, G. Fredriksson, I. Yadroitsev, Microstructural and thermal stability of selective laser melted 316 L stainless steel single tracks, *south African, J. Ind. Eng.* 28 (2017) 12–19, <https://doi.org/10.17166/28-1-1466>.
- [188] R. Rashid, S.H. Masood, D. Ruan, S. Palanisamy, R.A. Rahman Rashid, M. Brandt, Effect of scan strategy on density and metallurgical properties of 17-4PH parts printed by selective laser melting (SLM), *J. Mater. Process. Technol.* 249 (2017) 502–511, <https://doi.org/10.1016/j.jmatprotec.2017.06.023>.
- [189] C. Sanz, V. Navas Garcia, O. Gonzalo, G. Vansteenkiste, V. García Navas, Structural integrity of direct metal laser sintered parts subjected to thermal and finishing treatments, *J. Mater. Process. Technol.* 213 (2011) 2126–2136, <https://doi.org/10.1016/j.jmatprotec.2013.06.013>.
- [190] L. Costa, R. Vilar, Laser powder deposition, *Rapid Prototyp. J.* 15 (2009) 264–279.
- [191] A.S.M. Handbook, Vol. 3: Alloy Phase Diagrams, 9, , ASM Int., 1992 2.
- [192] W. Hofmeister, M. Wert, J. Smugeresky, J.A. Phillip, M. Griffith, M. Ensz, Investigating solidification with the laser-engineered net shaping (LENSTM) process, *JOM* 51 (1999) 1–6.
- [193] M. Hedges, Rapid Prototyping: Laser Engineered Net Shaping (TM)-Technology, Applications and Opportunities, *Eur. Congr. Exhib. Powder Metall. Eur. PM Conf. Proc.*, the European Powder Metallurgy Association 2003, p. 1.
- [194] G.K. Lewis, E. Schlienger, Practical considerations and capabilities for laser assisted direct metal deposition, *Mater. Des.* 21 (2000) 417–423, [https://doi.org/10.1016/S0261-3069\(99\)00078-3](https://doi.org/10.1016/S0261-3069(99)00078-3).
- [195] J. Smugeresky, D. Keicher, J. Romero, M. Griffith, L. Harwell, Laser engineered net shaping (LENSTM) process: optimization of surface finish and microstructural properties, *Proc. of the World Congress on Powder Metallurgy and Particulate Materials*, Princeton, NJ, 1997.
- [196] H. El Cheikh, B. Courant, S. Branchu, X. Huang, J.-Y. Hascoët, R. Guillén, Direct laser fabrication process with coaxial powder projection of 316 L steel. Geometrical characteristics and microstructure characterization of wall structures, *Opt. Lasers Eng.* 50 (2012) 1779–1784.
- [197] J.O. Milewski, G.K. Lewis, D.J. Thoma, G.I. Keel, R.B. Nemec, R.A. Reinert, Directed light fabrication of a solid metal hemisphere using 5-axis powder deposition, *J. Mater. Process. Technol.* 75 (1998) 165–172.
- [198] M. Ma, Z. Wang, D. Wang, X. Zeng, Control of shape and performance for direct laser fabrication of precision large-scale metal parts with 316 L stainless steel, *Opt. Laser Technol.* 45 (2013) 209–216.
- [199] P.L. Blackwell, The mechanical and microstructural characteristics of laser-deposited IN718, *J. Mater. Process. Technol.* 170 (2005) 240–246.
- [200] A. Ahmadi, R. Mirzaei, N.S. Moghaddam, A.S. Turabi, H.E. Karaca, M. Elahinia, Effect of manufacturing parameters on mechanical properties of 316 L stainless steel parts fabricated by selective laser melting: a computational framework, *Mater. Des.* 112 (2016) 328–338, <https://doi.org/10.1016/j.matdes.2016.09.043>.
- [201] W.F. Smith, *Structure and Properties of Engineering Alloys*, McGraw-Hill, 1993 (doi:6.0-6).
- [202] B. Zhang, C. Coddet, Selective laser melting of iron powder: observation of melting mechanism and densification behavior via point-track-surface-part research, *J. Manuf. Sci. Eng.* 138 (2016) 51001.
- [203] K. Abdelghany, Evaluating the properties of products fabricated from commercial steel powders using the selective laser micro-welding rapid manufacturing technique, *J. New Gener. Sci.* 8 (2010) 1–10.
- [204] K. Guan, Z. Wang, M. Gao, X. Li, X. Zeng, Effects of processing parameters on tensile properties of selective laser melted 304 stainless steel, *Mater. Des.* 50 (2013) 581–586, <https://doi.org/10.1016/j.matdes.2013.03.056>.
- [205] M.T.E.M.L. Griffith, J.D. Puskar, C.V. Robino, J.A. Brooks, J.A. Phillip, E. Smugeresky, W.H. Hofmeister, M.T.E.M.L. Griffith, J.D. Puskar, C.V. Robino, J.A. Brooks, J.A. Phillip, Understanding the microstructure and properties of components fabricated by laser engineered net shaping (lens), *Mater. Res. Soc.* 625 (2000).
- [206] J. Safka, M. Ackermann, L. Volesky, Structural properties of H13 tool steel parts produced with use of selective laser melting technology, *J. Phys. Conf. Ser.*, IOP Publishing 2016, p. 12004, <https://doi.org/10.1088/1742-6596/709/1/012004>.
- [207] P.B.M. Mazur, M. Leary, M. Brandt, Numerical and experimental evaluation of a conformally cooled H13 steel injection mould manufactured with selective laser melting, *Int. J. Adv. Manuf. Technol.* 93 (2017) 881–900, <https://doi.org/10.1007/s00170-017-0426-7>.
- [208] S.K. Shah, F. Czerwinski, W. Kasprzak, J. Friedman, D.L. Chen, Effect of transition metals on energy absorption during strain-controlled fatigue of an aluminum alloy, *Int. J. Fatigue* 87 (2016) 456–470, <https://doi.org/10.1016/j.ijfatigue.2016.02.008>.
- [209] M. Zhang, C.-N. Sun, X. Zhang, P.C. Goh, J. Wei, D. Hardacre, H. Li, Fatigue and fracture behaviour of laser powder bed fusion stainless steel 316 L: influence of processing parameters, *Mater. Sci. Eng. A* 703 (2017) 251–261, <https://doi.org/10.1016/j.msea.2017.07.071>.
- [210] L.M.S. Santos, J.A.M. Ferreira, J.S. Jesus, J.M. Costa, C. Capela, Fatigue behaviour of selective laser melting steel components, *Theor. Appl. Fract. Mech.* 85 (2016) 9–15.
- [211] F. Liu, X. Lin, H. Yang, X. Wen, Q. Li, F. Liu, W. Huang, Effect of microstructure on the fatigue crack growth behavior of laser solid formed 300 M steel, *Mater. Sci. Eng. A* 695 (2017) 258–264, <https://doi.org/10.1016/j.msea.2017.04.001>.
- [212] Y. Chew, J.H.L. Pang, G. Bi, B. Song, Effects of laser cladding on fatigue performance of AISI 4340 steel in the as-clad and machine treated conditions, *J. Mater. Process. Technol.* 243 (2016) 246–257, <https://doi.org/10.1016/j.jmatprotec.2016.12.020>.
- [213] S. Da Sun, Q. Liu, M. Brandt, V. Luzin, R. Cottam, M. Janardhana, G. Clark, Effect of laser clad repair on the fatigue behaviour of ultra-high strength AISI 4340 steel, *Mater. Sci. Eng. A* 606 (2014) 46–57, <https://doi.org/10.1016/j.msea.2014.03.077>.
- [214] J.M. Lourenço, S. Da Sun, K. Sharp, V. Luzin, A.N. Klein, C.H. Wang, M. Brandt, Fatigue and fracture behavior of laser clad repair of AerMet® 100 ultra-high strength steel, *Int. J. Fatigue* 85 (2016) 18–30, <https://doi.org/10.1016/j.ijfatigue.2015.11.021>.
- [215] S. Bhattacharya, G.P. Dinda, A.K. Dasgupta, H. Natu, B. Dutta, J. Mazumder, Microstructural evolution and mechanical, and corrosion property evaluation of Cu-30Ni alloy formed by direct metal deposition process, *J. Alloys Compd.* 509 (2011) 6364–6373.

- [216] B. AlMangour, D. Grzesiak, Jenn-Ming Yang, Selective laser melting of TiC reinforced 316 L stainless steel matrix nanocomposites: influence of starting TiC particle size and volume content, *Mater. Des.* 104 (2016) 141–151, <https://doi.org/10.1016/j.matdes.2016.05.018>.
- [217] B. AlMangour, D. Grzesiak, J.-M. Yang, Nanocrystalline TiC-reinforced H13 steel matrix nanocomposites fabricated by selective laser melting, *Mater. Des.* 96 (2016) 150–161, <https://doi.org/10.1016/j.matdes.2016.02.022>.
- [218] B. AlMangour, D. Grzesiak, J.-M. Yang, In situ formation of TiC-particle-reinforced stainless steel matrix nanocomposites during ball milling: feedstock powder preparation for selective laser melting at various energy densities, *Powder Technol.* 326 (2018) 467–478, <https://doi.org/10.1016/j.powtec.2017.11.064>.
- [219] S. Wang, S. Zhang, C.H. Zhang, C.L. Wu, J. Chen, M.B. Shahzad, Effect of Cr3C2content on 316 L stainless steel fabricated by laser melting deposition, *Vacuum* 147 (2018) 92–98, <https://doi.org/10.1016/j.vacuum.2017.10.027>.
- [220] J. Hashim, L. Looney, M.S.J. Hashmi, Particle distribution in cast metal matrix composites—part I, *J. Mater. Process. Technol.* 123 (2002) 251–257, [https://doi.org/10.1016/S0924-0136\(02\)00098-5](https://doi.org/10.1016/S0924-0136(02)00098-5).
- [221] B. AlMangour, M.-S. Baek, D. Grzesiak, K.-A. Lee, Strengthening of stainless steel by titanium carbide addition and grain refinement during selective laser melting, *Mater. Sci. Eng. A* 712 (2018) 812–818, <https://doi.org/10.1016/j.msea.2017.11.126>.
- [222] B. AlMangour, D. Grzesiak, T. Borkar, J.-M. Yang, Densification behavior, microstructural evolution, and mechanical properties of TiC/316 L stainless steel nanocomposites fabricated by selective laser melting, *Mater. Des.* 138 (2018) 119–128, <https://doi.org/10.1016/j.matdes.2017.10.039>.
- [223] B. AlMangour, D. Grzesiak, J.-M. Yang, Selective laser melting of TiB2/H13 steel nanocomposites: influence of hot isostatic pressing post-treatment, *J. Mater. Process. Technol.* 244 (2017) 344–353, <https://doi.org/10.1016/j.jmatprotc.2017.01.019>.
- [224] B. Almangour, D. Grzesiak, J.M. Yang, Rapid fabrication of bulk-form TiB2/316L stainless steel nanocomposites with novel reinforcement architecture and improved performance by selective laser melting, *J. Alloys Compd.* 680 (2016) 480–493, <https://doi.org/10.1016/j.jallcom.2016.04.156>.
- [225] B. AlMangour, F. Yu, J.-M. Yang, D. Grzesiak, Selective laser melting of TiC/H13 steel bulk-form nanocomposites with variations in processing parameters, *MRS Commun.* 7 (2017) 84–89, <https://doi.org/10.1557/mrc.2017.9>.
- [226] B. AlMangour, D. Grzesiak, J.-M. Yang, Selective laser melting of TiB2/316 L stainless steel composites: the roles of powder preparation and hot isostatic pressing post-treatment, *Powder Technol.* 309 (2017) 37–48, <https://doi.org/10.1016/j.powtec.2016.12.073>.
- [227] B. AlMangour, D. Grzesiak, J.-M. Yang, Scanning strategies for texture and anisotropy tailoring during selective laser melting of TiC/316 L stainless steel nanocomposites, *J. Alloys Compd.* 728 (2017) 424–435, <https://doi.org/10.1016/j.jallcom.2017.08.022>.
- [228] B. AlMangour, D. Grzesiak, J.M. Yang, In-situ tic particle reinforced 316 L stainless steel matrix nano composites: powder preparation by mechanical alloying and selective laser melting behaviour, *Solid Free. Fabr.* 2016 Proc. 27th Annu. Int. solid free. Fabr. Symp., Austin, Texas 2016, pp. 584–591<https://sffsymposium.engr.utexas.edu/sites/default/files/2016/044-AlMangour.pdf>.
- [229] Q. Wei, S. Li, C. Han, W. Li, L. Cheng, L. Hao, Y. Shi, Selective laser melting of stainless-steel/nano-hydroxyapatite composites for medical applications: microstructure, element distribution, crack and mechanical properties, *J. Mater. Process. Technol.* 222 (2015) 444–453.
- [230] L. Hao, S. Dadbakhsh, O. Seaman, M. Felstead, Selective laser melting of a stainless steel and hydroxyapatite composite for load-bearing implant development, *J. Mater. Process. Technol.* 209 (2009) 5793–5801.
- [231] W.H. Jiang, R. Kovacevic, Laser deposited TiC/H13 tool steel composite coatings and their erosion resistance, *J. Mater. Process. Technol.* 186 (2007) 331–338.
- [232] N. Axén, K.-H. Zum Gahr, Abrasive wear of TiC-steel composite clad layers on tool steel, *Wear* 157 (1992) 189–201, [https://doi.org/10.1016/0043-1648\(92\)90197-G](https://doi.org/10.1016/0043-1648(92)90197-G).
- [233] S. Gu, G. Chai, H. Wu, Y. Bao, Characterization of local mechanical properties of laser-cladding H13-TiC composite coatings using nanoindentation and finite element analysis, *Mater. Des.* 39 (2012) 72–80.
- [234] D. Novichenko, L. Thivillon, P. Bertrand, I. Smurov, Carbide-reinforced metal matrix composite by direct metal deposition, *Phys. Procedia* 5 (2010) 369–377, <https://doi.org/10.1016/j.phpro.2010.08.158>.
- [235] X. Wang, M. Zhang, S. Qu, Development and characterization of (Ti, Mo) C carbides reinforced Fe-based surface composite coating produced by laser cladding, *Opt. Lasers Eng.* 48 (2010) 893–898.
- [236] S. Qu, X. Wang, M. Zhang, Z. Zou, Microstructure and wear properties of Fe–TiC surface composite coating by laser cladding, *J. Mater. Sci.* 43 (2008) 1546–1551.
- [237] X.H. Wang, M. Zhang, L. Cheng, S.Y. Qu, B.S. Du, Microstructure and wear properties of in situ synthesized VC carbide reinforced Fe-based surface composite coating produced by laser cladding, *Tribol. Lett.* 34 (2009) 177–183.
- [238] Q. Zhang, J. He, W. Liu, M. Zhong, Microstructure characteristics of ZrC-reinforced composite coating produced by laser cladding, *Surf. Coat. Technol.* 162 (2003) 140–146, [https://doi.org/10.1016/S0257-8972\(02\)00697-7](https://doi.org/10.1016/S0257-8972(02)00697-7).
- [239] J. Dutta Majumdar, A. Kumar, L. Li, Direct laser cladding of SiC dispersed AISI 316 L stainless steel, *Tribol. Int.* 42 (2009) 750–753, <https://doi.org/10.1016/j.triboint.2008.10.016>.
- [240] B. Du, Z. Zou, X. Wang, S. Qu, In situ synthesis of TiB2/Fe composite coating by laser cladding, *Mater. Lett.* 62 (2008) 689–691, <https://doi.org/10.1016/j.matlet.2007.06.036>.
- [241] D. Novichenko, A. Marants, L. Thivillon, P.H.P.H. Bertrand, I. Smurov, Metal matrix composite material by direct metal deposition, *Phys. Procedia* 12 (2011) 296–302, <https://doi.org/10.1016/j.phpro.2011.03.038>.
- [242] M. Doubenskaia, I. Smurov, S. Grigoriev, M. Pavlov, Complex analysis of elaboration of steel–TiC composites by direct metal deposition, *J. Laser Appl.* 25 (2013), 42009.
- [243] A. Emanian, S.F. Corbin, A. Khajepour, Effect of laser cladding process parameters on clad quality and in-situ formed microstructure of Fe–TiC composite coatings, *Surf. Coat. Technol.* 205 (2010) 2007–2015, <https://doi.org/10.1016/j.surfcoat.2010.08.087>.
- [244] A. Emanian, M. Alimardani, A. Khajepour, Correlation between temperature distribution and in situ formed microstructure of Fe–TiC deposited on carbon steel using laser cladding, *Appl. Surf. Sci.* 258 (2012) 9025–9031, <https://doi.org/10.1016/j.apsusc.2012.05.143>.
- [245] A.P.I. Popoola, B.A. Obadele, O.M. Popoola, Effects of tic-particulate distribution in aisi 304l stainless steel matrix, *Dig. J. Nanomat. Biostruct.* 7 (2012) 1245–1252.
- [246] B. Du, Z. Zou, X. Wang, S. Qu, Laser cladding of in situ TiB2/Fe composite coating on steel, *Appl. Surf. Sci.* 254 (2008) 6489–6494, <https://doi.org/10.1016/j.apsusc.2008.04.051>.
- [247] J.D. Majumdar, L. Li, Studies on direct laser cladding of SiC dispersed AISI 316 L stainless steel, *Metall. Mater. Trans. A* 40 (2009) 3001.
- [248] K. Zhang, W. Liu, X. Shang, Research on the processing experiments of laser metal deposition shaping, *Opt. Laser Technol.* 39 (2007) 549–557.
- [249] J.C. Betts, The direct laser deposition of AISI316 stainless steel and Cr3C2 powder, *J. Mater. Process. Technol.* 209 (2009) 5229–5238, <https://doi.org/10.1016/j.jmatprotc.2009.03.010>.
- [250] B. Han, M. Li, Y. Wang, Microstructure and wear resistance of laser clad Fe–Cr3C2 composite coating on 35CrMo steel, *J. Mater. Eng. Perform.* 22 (2013) 3749–3754.
- [251] P. Xu, C. Lin, C. Zhou, X. Yi, Wear and corrosion resistance of laser cladding AISI 304 stainless steel/Al2O3 composite coatings, *Surf. Coat. Technol.* 238 (2014) 9–14, <https://doi.org/10.1016/j.surfcoat.2013.10.028>.
- [252] U. Scheithauer, A. Bergner, E. Schwarzer, H.-J. Richter, T. Moritz, Studies on thermoplastic 3D printing of steel–zirconia composites, *J. Mater. Res.* 29 (2014) 1931–1940.
- [253] U. Scheithauer, T. Slawik, E. Schwarzer, H.J. Richter, T. Moritz, A. Michaelis, Additive manufacturing of metal-ceramic-composites by thermoplastic 3D-printing (3DTP), *J. Ceram. Sci. Technol.* 6 (2015) 125–132, <https://doi.org/10.4416/JCST2014-00045>.
- [254] K. Agarwal, S. Vangapally, A. Sheldon, Binder Jet Additive Manufacturing of Stainless Steel–Tricalcium Phosphate Biocomposite for Bone Scaffold and Implant Applications, *Solid Free. Fabr.* 2017 Proc. 28th Annu. Int. Solid Free. Fabr. Symp. – An Addit. Manuf. Conf. 2017 2376–2388<https://sffsymposium.engr.utexas.edu/TOC2017>.
- [255] D.S.D. Uduwage, Binder Jet Additive Manufacturing of Stainless Steel–hydroxyapatite Bio-composite, Minnesota State University–Mankato, 2015<https://cornerstone.lib.mnsu.edu/etds/432>.